ISTITUTO NAZIONALE DI FISICA NUCLEARE
Laboratori Nazionali di Frascati

LNF-79/11(R)
9 Febbraio 1979

R. Bertani: THE NEW FRASCATI PROJECT: ALA/MDA.

Servizio Documentazione
dei Laboratori Nazionali di Frascati
Cas. Postale 13 - Frascati (Roma)

INFN - Laboratori Nazionali di Frascati
Servizio Documentazione

LNF-79/11(R)
9 Febbraio 1979

R. Bertani: THE NEW FRASCATI PROJECT : ALA/MDA.(x)

CONTENTS:

I - The physics of Adone and DCI 3
II - Results from photoproduction experiments 17
III - Nucleon-antinucleon interactions 21
IV - Theoretical expectactions for the physics of ALA/MDA 26
V - The ALA design 38
VI - The magnetic detector for ALA (MDA) 45
VII - Expected performances of the apparatus 80

INTRODUCTION.

The recent astonishing series of discoveries of new hadrons coupled to the e^+e^- (and $\mu^+\mu^-$) system$^{(1, 2)}$ has demonstrated the primary importance of e^+e^- storage rings for the progress of particle physics. At intermidiate energies, a study of the Adone data, which are briefly reviewed in Chapter I, showns an intriguing situation with many hints of new phenomena of great importance, which however have not been clarified because of limitations in the experiments and in the accelerator itself. As a matter of fact, at the present time while the experiments at Adone got to an end, these experimental indications of new phenomena fully justify a new campaign of research which, however, cannot be done at Adone at the required level of statistics and precision.

Electron-positron physics in the considered energy range is also covered by DCI, a new french machine, which is also briefly described in Chapter I. It has a fact, however, that after more than one year of efforts to improve its luminosity the principle by which a luminosity as large as 10^{32} cm^{-2} s^{-1} had to be reached with this machine ("charge compensation") does not work. This machine is consistently limited to luminosities as at Adone. On the other hand, a new machine can be desig

---

(x) - M. Sc, Thesis, University of Pisa (1979).

ned (ALA), which is expected to provide luminosities in excess of 10^{31} $cm^{-2}s^{-1}$ by exploiting a well-proven optics scheme ("low-β") at limitated beam currents (Chap. V). This accelerator, when equiped with a modern magnetic detector (the MDA project) would allow to improve the Adone data by a factor between 500 for inclusive physics and 2000 for exclusive physics, and thus would open an essentially new field of research.

The contribution to the knowledge of the phenomena studied with ALA and MDA by the photoproduction experiments and by $\bar{p}p$ annihilation experiments can be a usefull complement but cannot significantly reduce the unique role of the e^+e^- machine. These considerations are developed in Chapter II.

It is of great additional interest that, while exciting indications of new not-understood structures in $e^+e^- \longrightarrow$ hadrons were found at Adone and DCI, a welth of experimental data on nucleon-antinucleon states were also collected in other experiments, showing that most likely this system has many resonant and quasi-bound states. These data are reviewed in Chapter III. It has to be expected therefore that a significant selection of barion-antibarion states would also be found at ALA.

As a counterpart of the rich experimental picture, the theoretical expectations are also pointing at the importance of $e^+ e^-$ physics at ALA. Vector meson recurrencies are expected to show up a number of times, as well as baryonium bound and resonant states whose properties are anticipated to be different in $N\bar{N}$ potential models and in dual models, in particular with respect to radiative decays. More excitingly, the vector gluon of the Pati-Salam model can still be expected to show up at ALA energies, as well as the unit charge unstable light quarks of the same theory and possibly quarks of indefinite mass considered by T. T. Wu and collaborators. These theoretical expectations are reviewed in Chapters IV.

As a whole, the rich experimental picture indicated by Adone and DCI and implemented by photoproduction and $N\bar{N}$ experiments, as well as the intriguing and fascinating theoretical expectations point at the importance of the experimental program whose design is reviewed in the following.

CHAPTER I - THE PHYSICS OF ADONE AND DCI.

I. 1. - Adone

The parameter of an e^+e^- storage ring which is most relevent for experiments is the luminosity. The Adone(3) luminosity is shown in Fig. 1 in comparaison with that of other machines (record values). Typical luminosity in normal conditions is $L \sim 4 \times 10^{29}$ cm^{-2} s^{-1} at $W = 3.0$ GeV. As the hadronic cross-section $\sigma_h = \sigma$ ($e^+e^- \longrightarrow$ hadrons) is of the order of 20×10^{-33} cm^2, the rate of produced hadronic events is of the order of 30/hour, in each of the four intersections. The cms energy spread depends on energy as Γ_W (MeV) $\simeq$ 0.32 W^2 (GeV^2) (f. w. h. m.). This sets a lower limit of the order of one MeV to the narrow resonancies that can be resolved in an energy scan. The source section is smaller then 1 mm^2. The source length, as determined by the head-on collision of the machine bunches increases with energy from about 25 to about 50 cm (f. w. h. m.). The straight section length available for experiments is 220 cm, the vacuum tube being 20 cm and the quadrupoles about 60 cm in diameter. Because of the large source length as well as of the limited straight section length any large detector covers an effective solid angle appreciably smaller than the solid angle for point source.

I. 2. - The second generation Adone detectors

After the series of first generation experiments (4), three experiments in the period 1973-1978 have provided important data on various hadronic channels. The main properties of these experiments are summarised in Table I(5).

The $\gamma\gamma 2$ apparates (6) is shown in Fig. 2 . It comprises two semi-cylindrical telescopes transverse to the beam in which layers of trigger counters, optical spark chambers and lead or iron converters are sandwiched up to a total thickness of 5.5 Xo. Thus the system detects charged tracks and also photons.

For point source, the solid angle covered by the trigger counters is 40% of 4π . The coverage of the main detector is 66% of 4π (Table I), while the photon signature is improved by additional telescopes over 27% of 4π . Over this region, pions of energy smaller than 300 MeV are stopped by range. A pair of end-cap telescopes covers an additional solid angle of $0.15 \times 4\pi$. A many-

TABLE I - Main parameters of the Adone experiments(5)

$B\bar{B}$ Calorimetry, dE/dx vs. E , $\gamma\gamma 2$ γ detection , MEA Momentum analysis

	$B\bar{B}$	$\gamma\gamma 2$	MEA
Orientation of the axis of symmetry referred to the beam direction	parallel	orthogonal	orthogonal
Solid angle for point like source / 4π	70 %	66 %	40 %
Direction measured by	magnetostrictive S. C.	optical S. C.	optical S. C.
Momentum measured by	E, dE/dx	range	magnet
Quality of mom. meas.	poor	poor	good
Quality of photon detection	poor	good	poor
Minimum energy (MeV) for a pion to trigger	$\sim$ 60	$\sim$ 120 ($\sim$ 35 + γ's)	$\sim$ 130
Luminosity monitors	S. A. Bhabha W. A. Bhabha Double bremss.	S. A. Bhabha W. A. Bhabha	S. A. Bhabha W. A. Bhabha

fold coincidence generates a charged trigger for pions when $T_\pi > 120$ MeV and for kaons when $T_K > 190$ MeV. Photons are also included in the trigger by a triple coincidence in the outer counter layers. A number of triggers are generated, the most inclusive one being one photon and one charge prong. The computed photon detection efficiency is shown in Fig. 3. For a still loose photon signature (curve b) the efficiency is not above 70÷80% and the threshold is about 50 MeV. Only a very rough measurement of the energy of the detected photons is possible in practice.

The MEA experiment (7) is a solenoid, 2 m long and 2 m in diameter, set transverse to the beam and generating a field of about 2 Kgauss (see Fig. 4 and Table I). Thin optical spark chambers in the field measure the momenta of charged tracks with a resolution of the order of ± 8%. Behind the coils, over a solid angle of ~ 20% of 4π, two telescopes of thick-plate optical spark chambers help in discriminating hadrons from muons and provide some photon signature. The trigger is generated by thin vertex detectors and layers of scintillators outside the coils, which accept pions if $T_\pi > 130$ MeV and kaons if $T_K > 190$ MeV. At least two tracks, one in the above and one in the below hemisphere, are required.

The B$\bar{B}$ experiment (8) (Fig. 5 and Table I) is an array of counters with cilindrical symmetry coaxial with the beam. The trigger is provided by barrels of counter hodoscopes, one of which (Hod 3, 35 g/cm^2 of liquid scintillator) measures also dE/dx (with resolution AE/E ≃ 20% at $E_p = 100$ MeV). A set of cilindrical magnetostrictive spark-chambers measures the charged tracks emitted at the vertex. An electron (photon) signature is provided by two sets of flash-tubes lead-iron sandwiches. One track in the trigger is defined by a collinear a 1-2-3 coincidence (corresponding to $T_\pi > 60$ MeV). Two or more tracks at various azimuths can be required in the trigger, depending on background conditions. Background rejection can also require futher off-line conditions. If hodoscope 4 is required to be fired in the off-line analysis, this corresponds to impose $T_\pi > 200$ MeV.

I. 3. - The physics of Adone

We will briefly review only those data that are most likely to be studied again in detail at ALA. We therefore will completely forget about the J/ψ studies.

A scan for narrow resonances in steps of 1 to 4 MeV (depending on energy) has given a negative result (9). The data is shown in Fig. 6.

The upper limit set on the integrated rate is typically

$$\int_{\Delta W} (\sigma - \langle\sigma\rangle)\, dW \leq 0{,}07 \int_{\Delta W} (\sigma J/\psi - \langle\sigma\rangle)\, dW$$

where the signal is derived from fluctuations of σ with respect to its average $\langle\sigma\rangle$ over the machine energy resolution ΔW, and the corresponding J/ψ signal (≳ 10 nb. GeV) is taken as reference. The limited machine luminosity and detector efficiency did not allow to reach a better sensitivity, nor to scan at lower energies (below ≳ 1. 45 GeV).

The final Adone data have included a good measurement of $R = \dfrac{\sigma\ \text{hadronic}}{\sigma_{\mu\mu}}$, as shown in Fig. 7(10).

This data proves the exceptional increase of the hadronic cross-section above W = 1GeV, and is highly suggestive of the opening-up of new channels. With reference to the example provided by the SPEAR data, one can think in terms of narrow resonances followed by broader ones. However, as we have seen the search for these structures is lacking at the lowest energies.

Three structures of width ranging between a few MeV and a few tens of MeV have been observed. At W ~ 2. 13 MeV the MEA group has noticed a 5÷6 standard deviation peak (Fig. 8) in K*(890) production around 2130 MeV; 40.5 ± 5.8 events are observed, where 13.1 ± 2.5 would be expected on the basis of the interpolating straight line shown in the figure. The attempted fit to a Breit-Wigner resonance gives M = 2130 MeV, $\Gamma = \pm 30$ MeV. It is observed that the significance of the effect should be improved and even more, that extracting the K^* signal itself from the data is rather delicate owing to the poor K/π discrimination. The lack of a clear signal in inclusive K-production at the same energy (nK/nch 8,2 % at the resonance, nK/nch ~ 10,5 % at W = 2300 MeV) can be taken as an indication of such poorness, rather than as a hint for surprising decay branching ratios of the resonance.

At W = 1.82 GeV the three Groups have observed a structure in the inclusive cross-section for three or more charged particles seen in the apparatus (Fig. 9). The results of Breit-Wigner fits are reported in Table II. Some apparent inconsistency among the peak position observed in the three experiments has led to an attempt to interpret the data as two interphering resonances (line 1 of Table II), giving the overall fit shown in Fig. 10. However, in view of the different (and relatively small) acceptancies of the three detectors and of the poor statistics one cannot exclude the possibility that the differencies among the data are due to systematic effects and statistical fluctuations. On the other hand, the situation might as well be as complex as suggested by Fig. 11.

TABLE II - The 1820 fits.

	MASS (MeV)		WIDTH (MeV)		χ^2/d.f.
	M_2	M_1	Γ_2	Γ_1	
$B\bar{B}$ with interference	1812^{+7}_{-13}	(1792^{+31}_{-14})	34^{+21}_{-15}	(79^{+77}_{-29})	6.1/9
$B\bar{B}$ without interference	1836^{+3}_{-3}	(1765^{+14}_{-38})	13^{+3}_{-2}	(47^{+25}_{-20})	8.8/11
$\gamma\gamma 2$	1819 ± 5		21 ± 5		5.6/11
MEA	1821 ± 16		31 ± 15		10/14

The interpretation of this or these structures is not at all elucidated by the available information on the branching ratios. The $\gamma\gamma 2$ Group has compaired the excitation curves in the 3,4 Ch + + $\geqslant 1\gamma$ and 3,4 Ch (Fig. 12). The absence of signal in the latter distribution can be understood if a G = - 1 $2\pi^+ 2\pi^- \pi^0$ channel is dominating. On the other hand, both the width and the position of the structure would be much more suggestive of a ϕ than of an ω-recurrence (see Chapter IV). A search for an excess of kaons at this energy (Fig. 13) did not give conclusive results. Moreover, typical ϕ^* decays would be KK^*, $\phi\pi\pi$, etc., leading to signals in the 4-charged hadronic channel which gives an important contribution in the channel with 3-4 observed prongs. May be indeed this is not a ϕ recurency. However, we can take this as an example of quite a general situation at Adone and DCI, where low statistics, unsufficient detector acceptance and poor particle recognition prevents from reaching any firm conclusion on the physics meaning of an observed anomaly in the data.

A very narrow structure in inclusive hadronic production was observed at Adone in 1977 (Fig. 14 first colum) suggesting a resonance at M $\approx$ 1499 MeV with $\Gamma \approx 2 \div 3$ MeV. Further data collected in 1978 has brought to the confusing overall picture shown in the second column of the same figure. An attempt by the $\gamma\gamma$ 2 Group to reproduce at least the peak/valley ratio by means of three points with higher statistics has failed (Fig. 15).

On the other hand, in order to attribute a conclusive power to this negative result one would have to trust the Adone energy scale to better than 1 MeV, while it is by no means clear that the absolute machine energy is known so well. Also, the long term stability of the detectors might be questioned. In conclusion, it is still unclear whether something important (in view of the narrow width) is hiding itself in this energy region.

A number of inclusive measurements at Adone are also suggestive of interesting phenomena and calling for better data. In Fig. 16 the NCh /< No > ratio is compaired to the one measured at SPEAR showing a deviation from the value of 2 predicted by isospin conservation in pion production and change of trend at Adone energies. The much larger errors of the Adone data with respect to SPEAR are due in part to the incomplete photon detection efficiency and more to the uncertainties in the large Montecarlo corrections applied to the raw data. Similar consideration are applicable to another piece of information, the 4π excitation cross-section shown in Fig. 17.

Although the comparison with older Novosibirsk data at lower energy might be suggestive of a broad ϱ-recurrency, the large statistical errors, the incompleteness of the scan, as well as some large fluctuaction in the data leave the possibility open for some more subtle phenomenon left undiscovered by these explorative measurements.

The possibility that at the Adone energies light quarks or relatively heavy leptons are produced and have not been discovered yet deserves special attention. A search for heavy sequential leptons produced as $e^+e^- \longrightarrow L^+L^-$ with subsequent $L^\pm \longrightarrow e^\pm \nu\nu$, $L^\pm \longrightarrow \mu^\pm \nu\nu$ decay has been made long ago(11), giving a lower limit to the mass of the heavy lepton of $M_\tau \gtrsim 1 \div 1.5$ GeV. Since the production cross-section can be calculated in QED and the leptonic branching ratio using the universal weak coupling constant, this negative result looks rather significant. This is also strengthened by the lack of e, μ events below $W \simeq 3.6$ GeV in the SPEAR results (12). However, a conclusive negative result can only come from direct measurements with a detector providing a much better e, μ signature than at Adone and exploiting a much higher machine luminosity.

In contrast to the unlikely existence of a new heavy lepton below the τ the possibility of an excited electron or muon is more open. A search for the reaction $e^+e^- \longrightarrow e^* e$ was made by the $\gamma\gamma$ 2 experiment by detecting e, γ events (13) at large angles, in association $\hookrightarrow e\gamma$ with inelastically scattered electrons in tagging counters set inside the gap of the Adone bending magnets. The resolution at large angles was $\Delta\theta_e = \pm 2^\circ$, $\Delta\theta_\gamma = \pm 4^\circ$, with no energy measurement (computed efficiency as in Fig. 3), while the tagging efficiency was monitored by detecting beam-gas bremsstrahlung. The results are compaired with the expected QED rate of beam-beam large angle bremsstrahlung in Fig. 18. The poor statistics and some uncertainty in detector efficiency limit the significance of this result. By writing the $e\,\gamma\,e^*$-interaction in terms of the Hamiltonian

$$H = \lambda \frac{e}{m^*} \bar{\psi}_e \, \sigma_{\mu v} \, \psi_e F^{\mu v}$$

one can derive from this data an upper limit to the compling constant λ as a function of m^* (Fig. 19). The limit, which is around 3×10^{-4}(o), can and should be largely improved at ALA. Moreover a similar search could be made for μ^* production, if an adeguate muon signature is available.

Finally, one should leave the possibility open that quarks are produced free and are not observed yet. The Adone experiments had no sensitivity to 1/3 e charged quarks, and probably also to 2/3 e charges. This is also true for the SPEAR and Doris experiments. This situation calls for an experiment at ALA with accurate dE/dx measurements and sensitivity to very low ionization. One also has the possibility that quarks are not stable or not detectable over long path lengths. Unstable quarks of unit charge are indeed predicted in some theory, as well as quarks which cease ionizing after some path. These theoretical ideas are discussed in Chapter IV. The MDA experiment at ALA is designed such as to tag also these particles.

I. 4. - DCI

DCI is the french e^+e^- storage ring which was built some time ago for similar porpouses as ALA. The machine is operating in its full configuration since summer 1977. The design luminosity was $\sim 10^{32}$ cm^{-2} s^{-1} at W = 3.0 GeV, with two bunches/beam and 200÷250 mA/bunch (15). Such a high luminosity was based on the principle of "charge compensation": the accelerator is composed of two rings one on top of the other, having the two 6-m long straight sections in common (Fig. 20).

(o) - The absence of strong modifications to the $e\gamma e$ vertex was also checked in the BCF experiment on Bhabha scattering (14).

One section is used for injection and one is free for experiments. Electrons of beam one and positrons of beam two (and viceversa) merge together at the intersect, such that four-bunch collisions take place with a net total charge zero (to within a few percents of the single bunch charge). In a two-beam operation, without charge compensation, the luminosity was expected to be lower by about two orders of magnitude. The magnetic radius in the bending magnets is 3. 8 m and the ring length is 94. 6 m (Fig. 21). The top energy is W = 3. 6 GeV. The energy dependence of the luminosity will be discussed later, in comparison with the expected ALA performances. The charge-compensation scheme has proved to be very delicate and not really understood. At present, private communications report that with four beams a maximum increased of luminosity of about 30% over two beams was observed. The last official report in summer 1977(15) on two-beam operation shows a beam size explosion at a current of 20 + 30 mA (Fig. 22) and corresponding luminosities below 10^{29} cm^{-2} s^{-1} (Fig. 23). For $1.35 \lesssim W \lesssim 2.0$ GeV, well inside the ALA energy region, the luminosity obtained with two beams is very similar to Adone.

I. 5. - The physics of DCI

Even working with luminosities of the order of 10^{29} cm^{-2} s^{-1}, DCI has contributed in 1977/78 a few interesting indications on structures in partial hadronic cross-sections. An old ACO detector was employed, (M3N), consisting of a longitudinal solenoid with sandwiches of trigger scintillators, optical spark-chambers interleaved with lead-converters, and a double layer of proportional chambers (also employed in the trigger (Fig. 24)(16). The solid angle is $\Delta\Omega \simeq 0.6 \times 4\pi$, T_π = 220 MeV is the maximum range for pions stopping in the detector, T_π = 85 MeV is the minimum energy for triggering, and ∼ 90% is the photon conversion efficiency at $E_\gamma \sim$ 100 MeV. Besides data on $\sigma(4\pi)$ which show a broad enhancement at W ∼ 1,5 GeV similar to what observed at Adone (Fig. 25) two structures are observed (although with poor statistics) in $\sigma(5\pi)$ (and in part in $\sigma(3\pi)$) at $M_1 \sim$ ∼ 1660 MeV with $\Gamma_1 \sim$ 40 MeV, and $M_2 \sim$ 1770 MeV with $\Gamma_2 \sim$ 50 MeV, which could correspond to two resonances with I = 0, G = - 1(17) (Fig. 26).

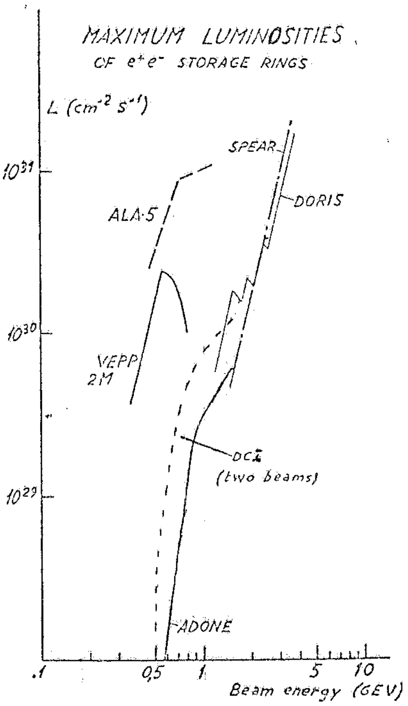

FIG. 1 - Luminosity versus energy for Adone and other machines.

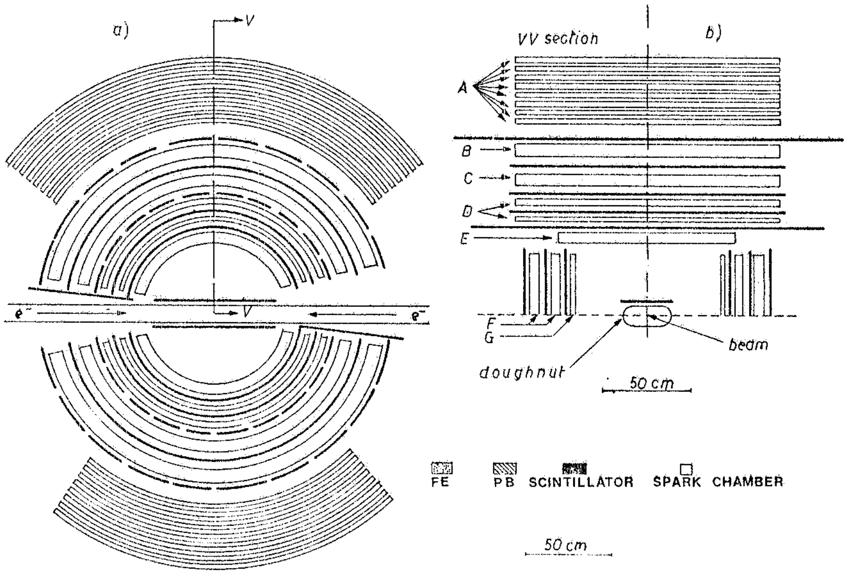

FIG. 2 - The $\gamma\gamma$ 2 apparatus.

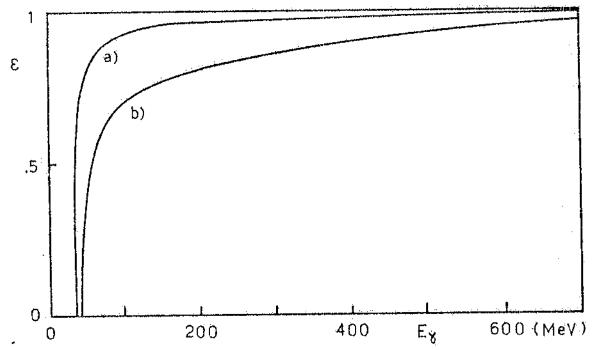

FIG. 3 - Montecarlo predicted efficiency for the $\gamma\gamma 2$ apparatus, if a photon is defined as a) one layer hit; b) two layers hit.

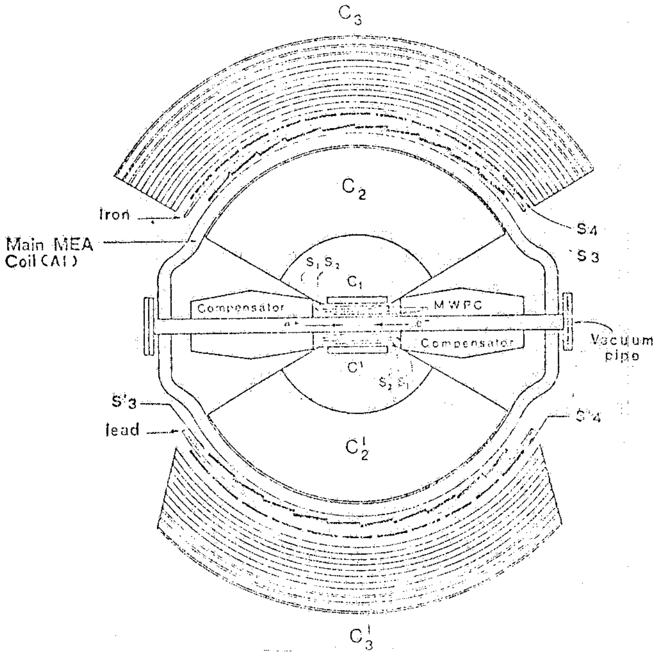

FIG. 4 - MEA experimental set-up (vertical section). C_1, C'_1 are narrow gap spark chambers; C_2, C'_2 are wide gap cylindrical spark chambers for momentum analysis; C_3, C'_3 are thick plate spark chambers for particle identification. MWPC are multiwire proportional chambers; S_1, S'_1, ..., S_4, S'_4 are scintillation counters.

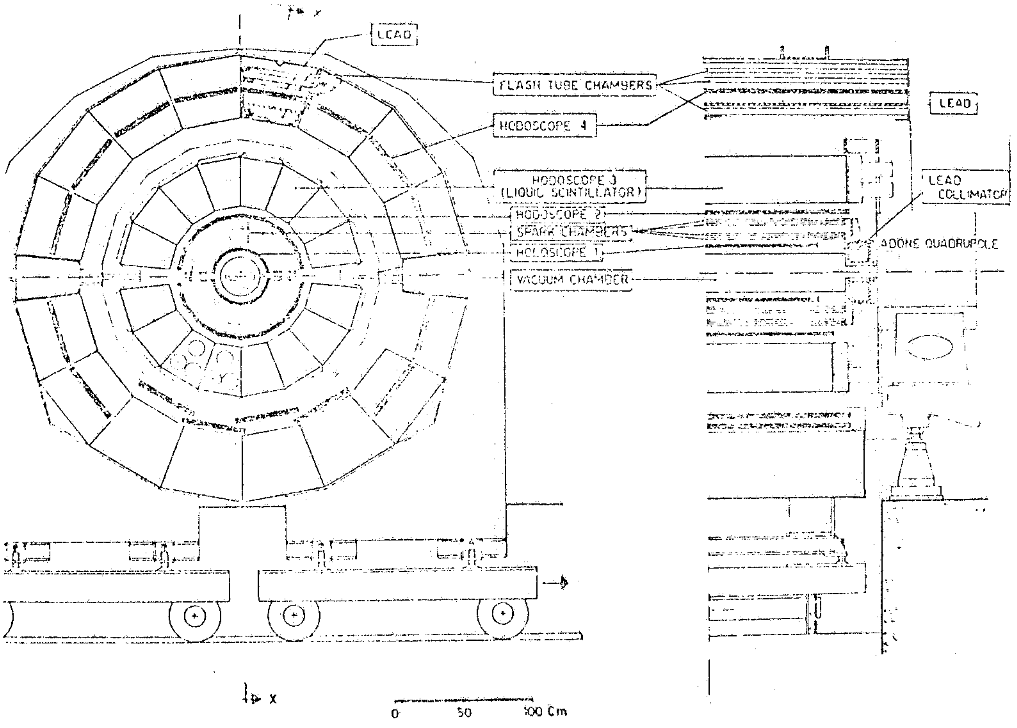

FIG. 5 - The $B\bar{B}$ apparatus (5).

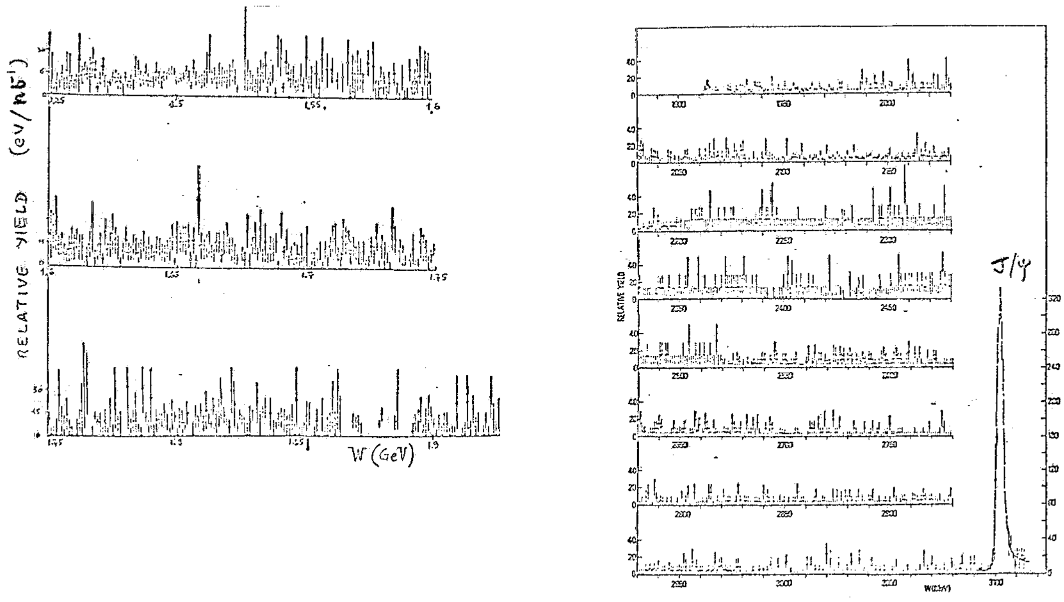

FIG. 6 - Scan for narrow resonances at Adone$^{(10)}$.

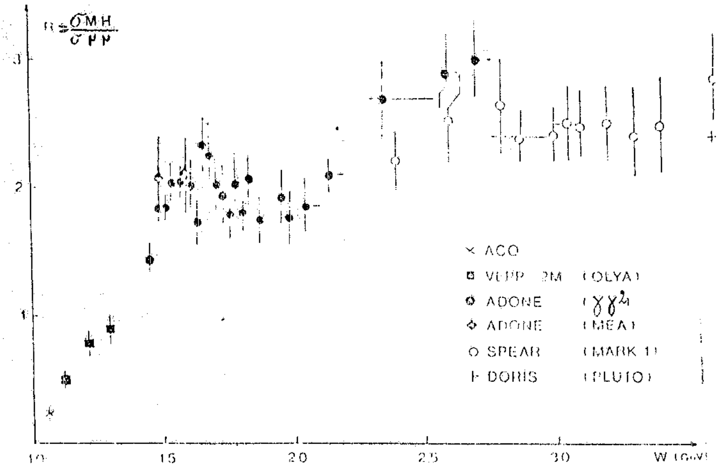

FIG. 7 - R-data from a number of experiments$^{(10)}$.

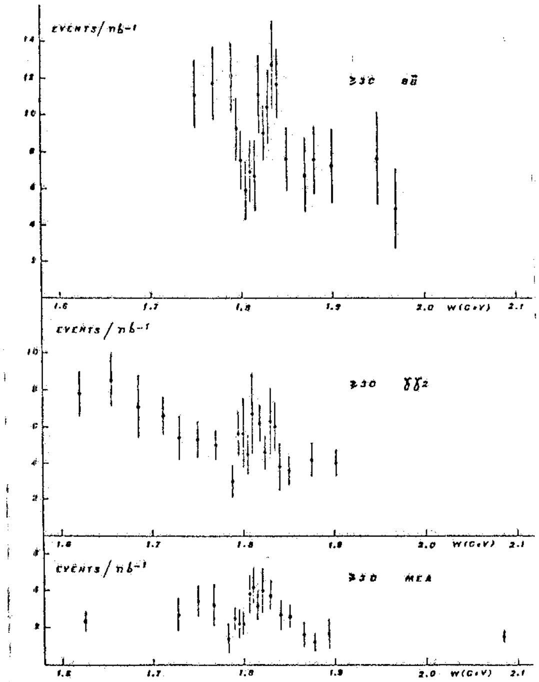

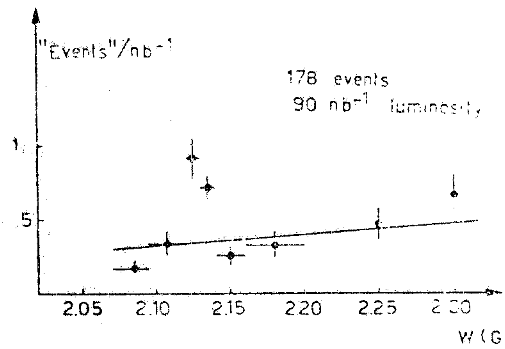

FIG. 8 - $(\pi K)^0$ yield vs. C. M. energy W. $(800 < M_{\pi K} < 950\ \mathrm{MeV}/c^2)$ $^{(5)}$.

FIG. 9 - The 1820 resonances in the three experiments$^{(5)}$.

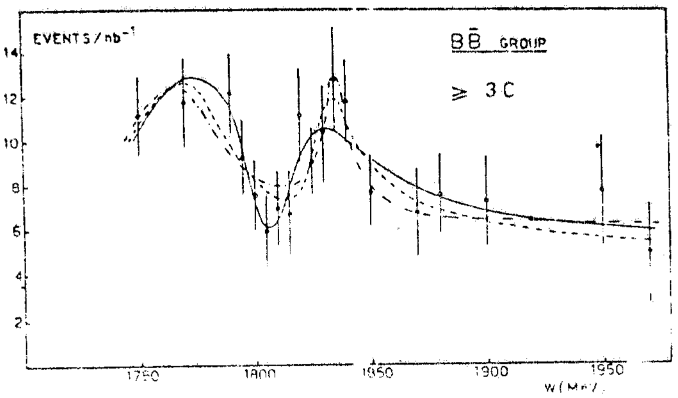

FIG. 10 - Fits to the B$\bar{B}$ yield vs W for (≥3C) hadronic events.
Fit 1 Table II ——— (linear term + BW$_1$ + BW$_2$ + interference (BW$_1$, BW$_2$));
Fit 2 Table II
- - - - - (linear term + BW$_1$ + BW$_2$)
— — — (linear term + BW$_1$ + BW$_2$ + interference (BW$_2$, linear term).

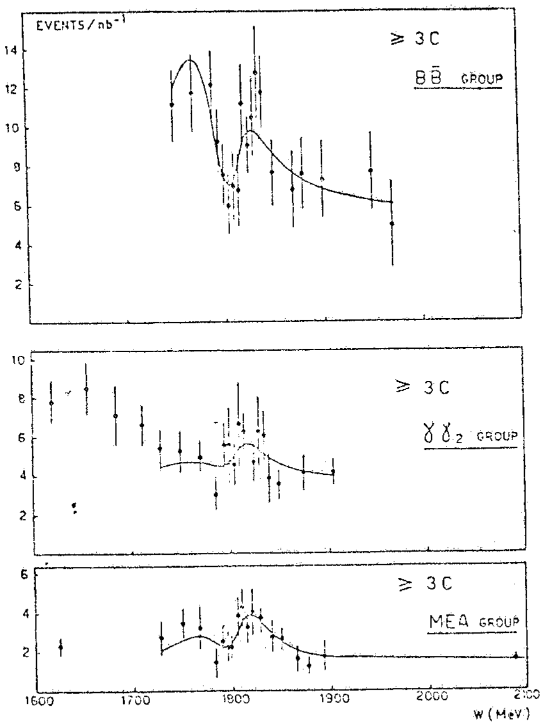

FIG. 11 - The 1820 fits in the three experiments.

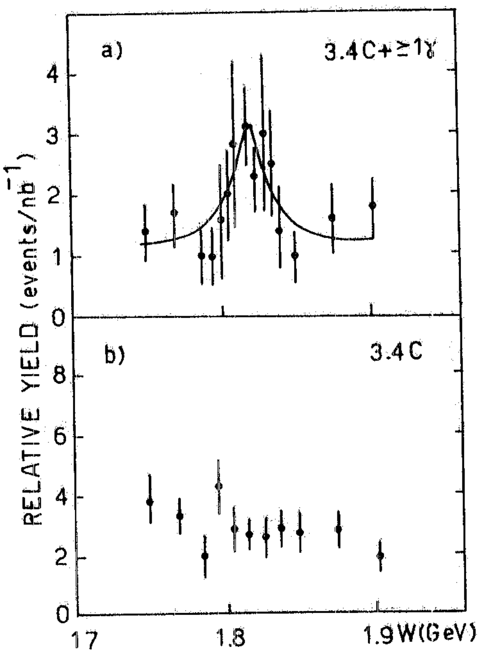

FIG. 12 - The γγ2 data in the channels 3,4 Ch + ≥1γ and 3,4 Ch.

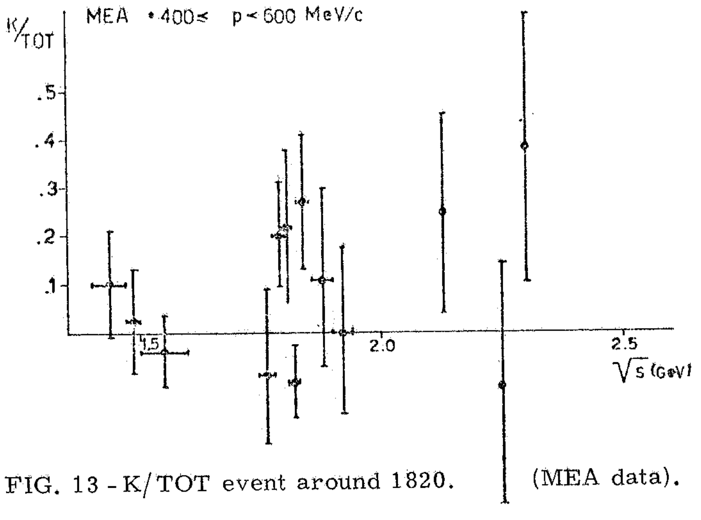

FIG. 13 - K/TOT event around 1820. (MEA data).

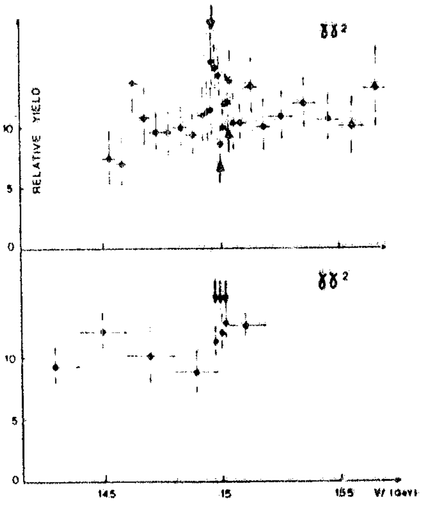

FIG. 15 - γγ2 high statistical data on the 1500 region$^{(10)}$.

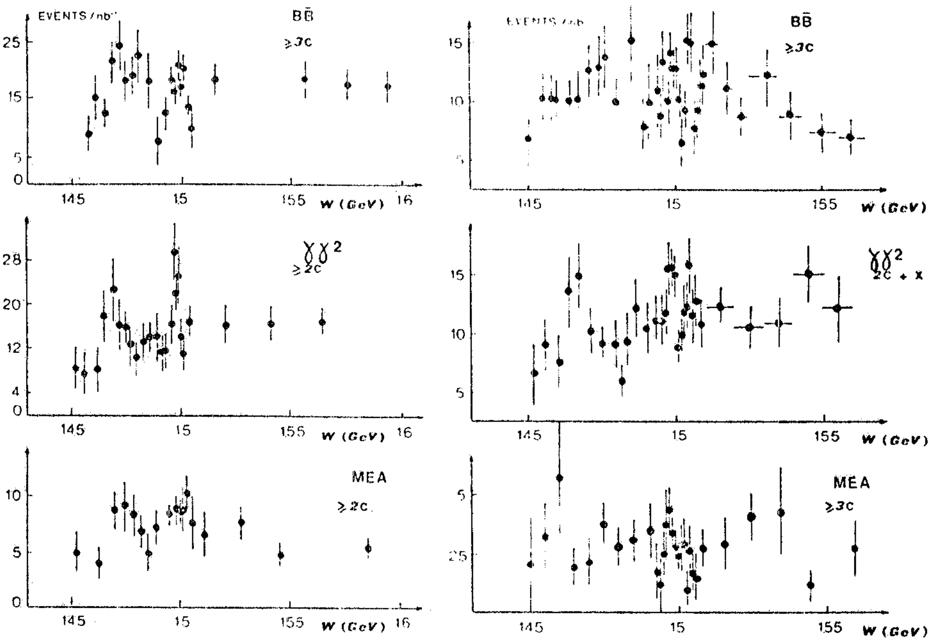

FIG. 14 - Adone data around W = 1500; first coloumn, 1977 data; second coloumn, overall data (10).

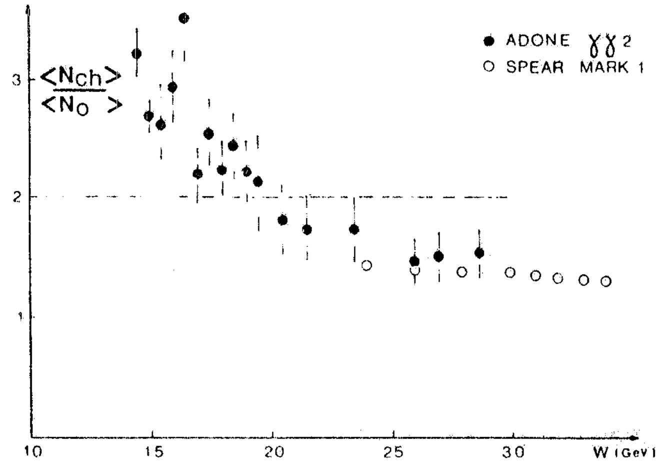

FIG. 16 - $\langle NCh \rangle / \langle No \rangle$ at Adone at SPEAR (10).

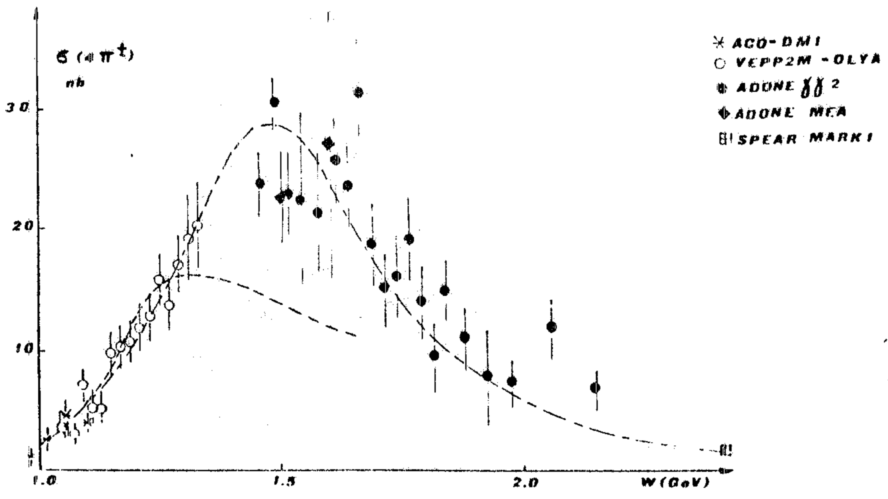

FIG. 17 - $\sigma(4\ \pi^{\pm})$ ad Adone with some low energies VEPP 2M data (10).

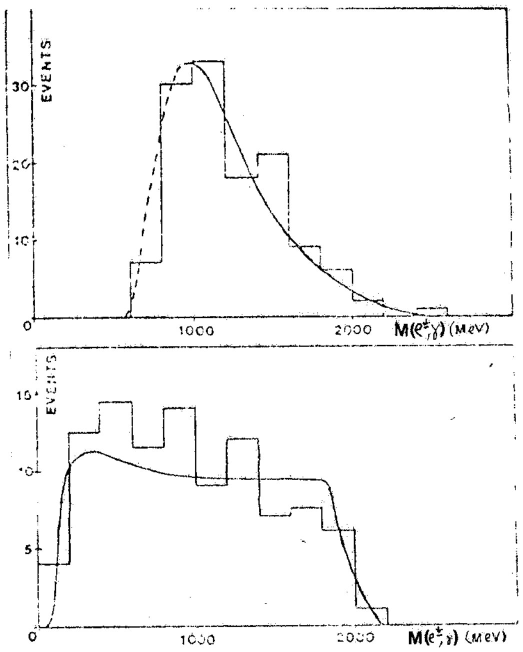

FIG. 18 - Experimental (histograms) and computed (curves) events distribution versus effective (eγ) mass, for events with two e and one γ at large angles (lower), and one e and one γ at large angles, with one tagged electron (upper)(13).

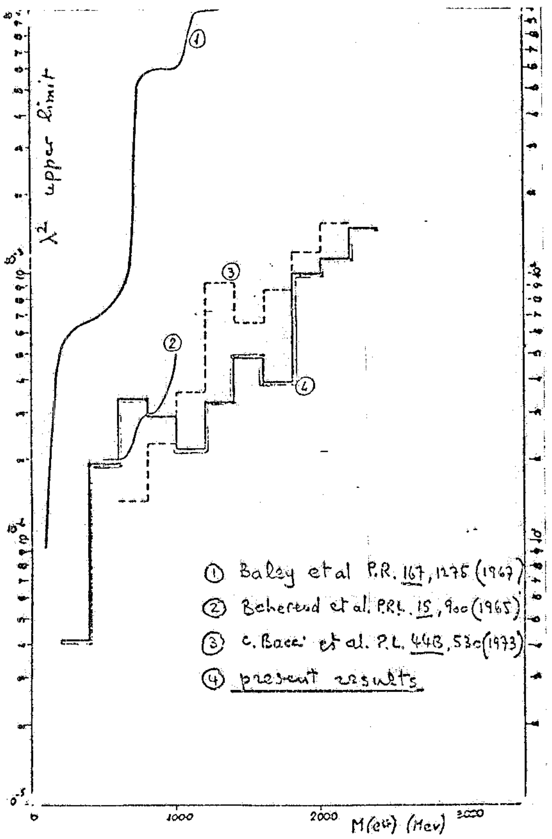

FIG. 19 - Upper limit on λ^2 versus the e^* mass (13).

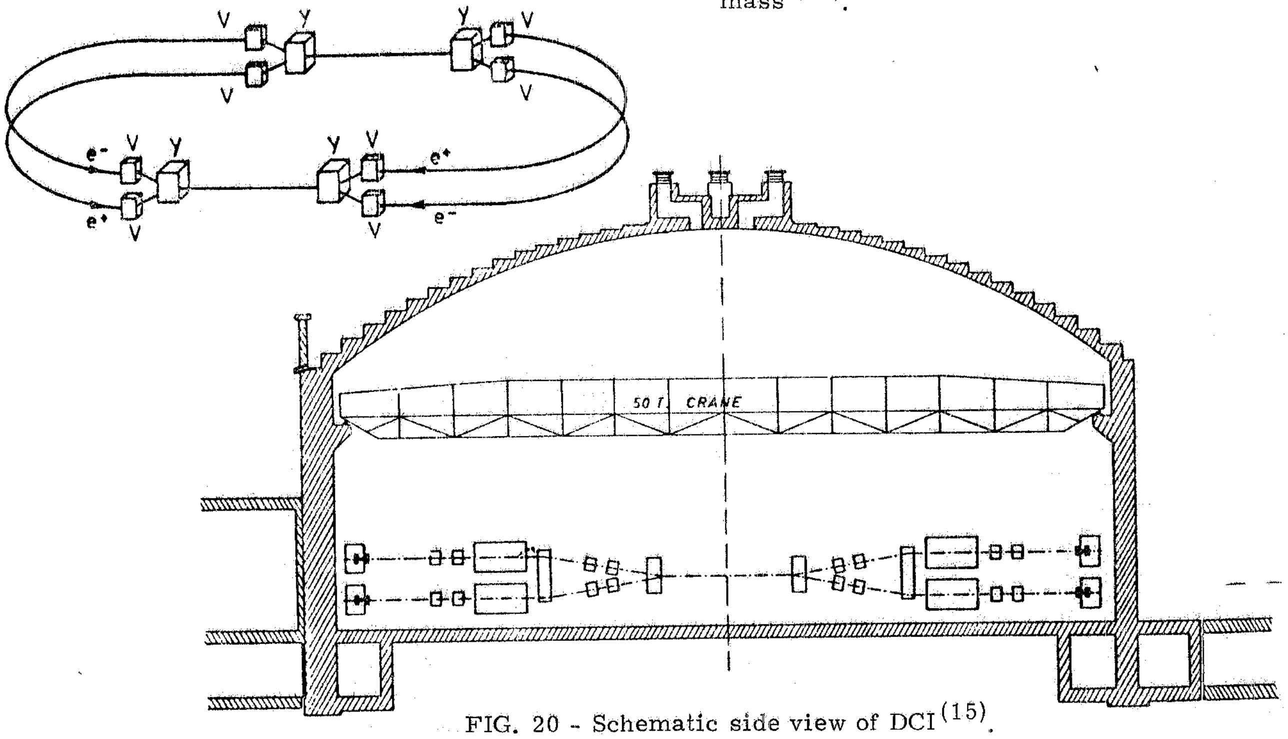

FIG. 20 - Schematic side view of DCI(15).

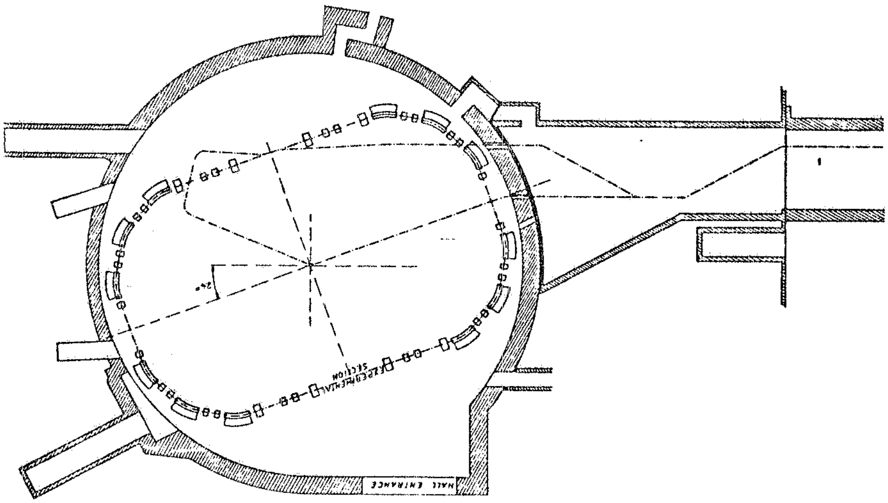

FIG. 21 - Schematic plan view of DCI$^{(15)}$.

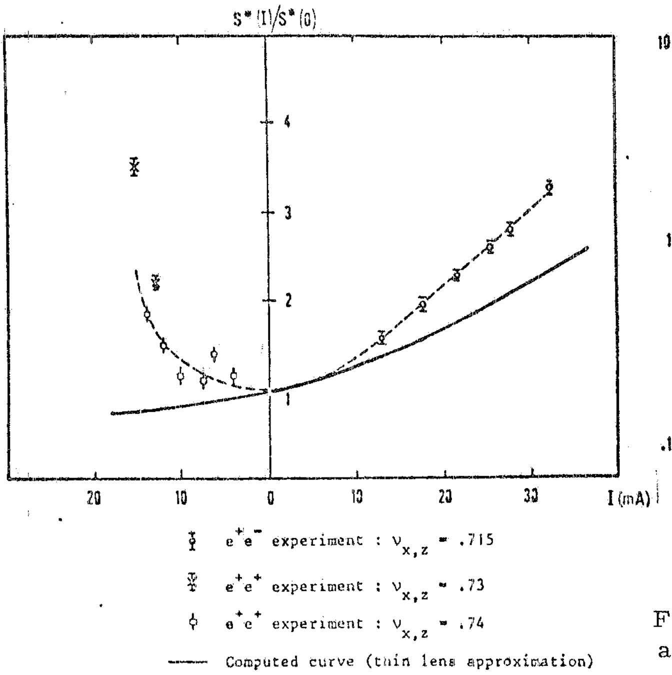

FIG. 22 - Effective beam tranverse section at the interaction point versus current at W = 1.6 GeV$^{(15)}$.

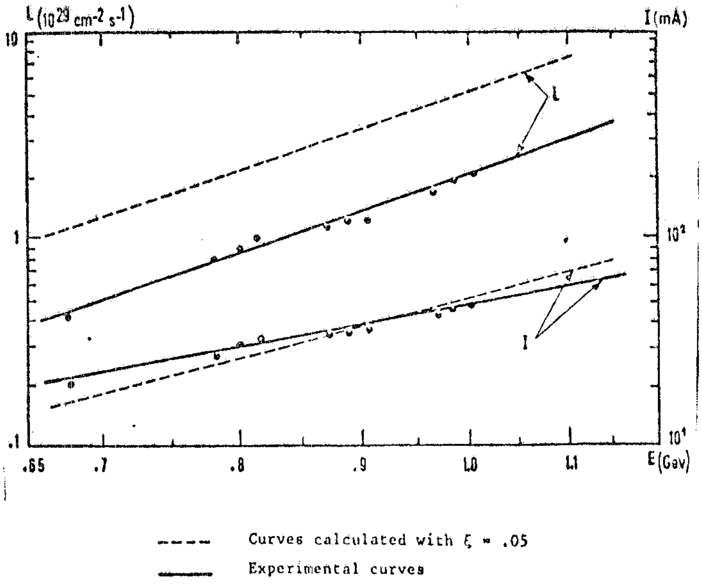

FIG. 23 - Energy dependence of maximum current and luminosity for two beam operation$^{(15)}$.

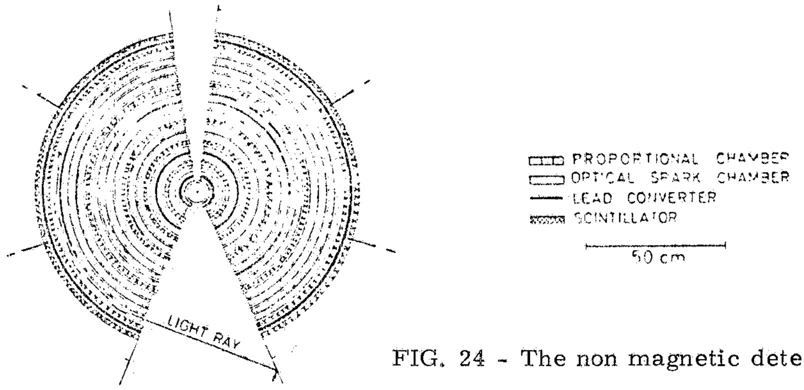

FIG. 24 - The non magnetic detector used in 1977 at DCI$^{(16)}$.

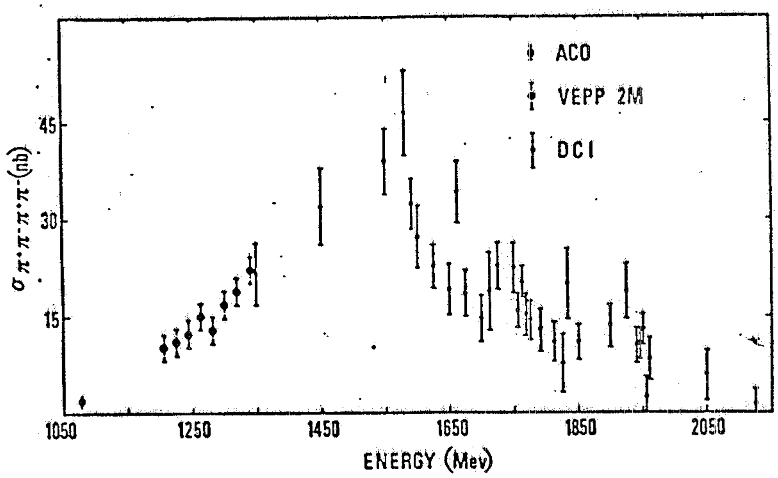

FIG. 25 - $\sigma(4\pi)$ at DCI.

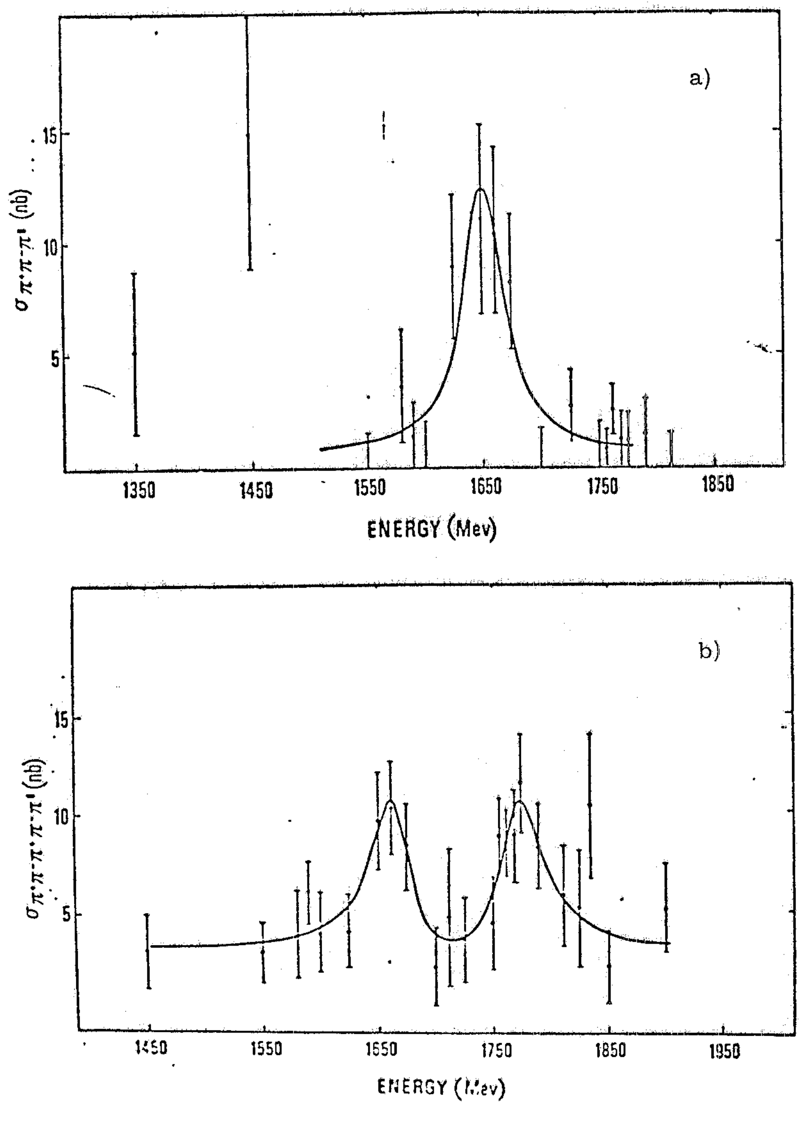

FIG. 26 - a) $\sigma(3\pi)$, and b) $\sigma(5\pi)$ at DCI.

CHAPTER II - RESULTS FROM PHOTOPRODUCTION EXPERIMENTS.

II. 1. - The Desy-Frascati experiment

The classical photoproduction experiments of ϱ, ω, ϕ, where the mass-spectrum of the photoproduced forward e^+, e^- pairs studied searching for Compton production of vector mesons over a non-resonant background (which can be calculated by the Bethe-Heitler formula), have been recently extented to $1 \leqslant m_{e^+e^-} \leqslant 1,8$ GeV in a Desy-Frascati experiment. The effect of very small Compton production amplitudes was emphasized in this experiment (18, 19) by studying the mass distribution of the asymmetrical (in the exchange of e^+ with e^-) contribution to the spectrum. This contribution exists because of the interpherence term between the C - odd Compton amplitude

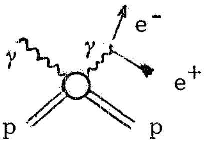

and the C - even Bethe-Heitler amplitude

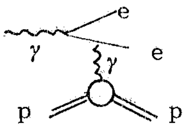

and gives much larger effect at the resonances than in the direct mass spectrum, as long as the Compton amplitude is much smaller than the Bethe-Heitler one and the latter is still sizable.

The results of the Desy-Frascati experiments, as at summer 1978, are shown in Fig. 27. The structure at about 1250 MeV and the bump at larger masses have very high statistical significance, in view of the fact that a negative interference rate is expected above the ϕ. This is shown in Fig. 28, where the contribution of different vector mesons is shown separately. The data provide evidence for possible resonances with $M = 1097^{+16}_{-19}$ MeV and $\Gamma = 31^{+24}_{-20}$ MeV, $M = 1266 \pm 5$ MeV and $\Gamma = 110 \pm 35$ MeV and for additional objects at larger masses. These data are not in contradiction with the Adone-DCI results which do not extend below W = 1400. However, they should be compared to the Novosibirsk data at this energy which are shown in Figs. 7 and 17 of Chapter I. In view of the small solid angle and poor particle discrimination of the Novosibirsk experiment, it is felt that high statistics accurate measurements at ALA should be able to find structures corresponding to those of the photoproduction experiment, maybe not in the four π channels.

II. 2. - Other photoproduction experiments

The existence of structures around 1800 MeV has been confirmed in a Cornell-Harvard photoproduction experiment (20), similar to the Desy-Frascati one, but using the higher energy photon beam of Cornell (EMAX = 11. 5 GeV) and selection kaons in the double spectrometer. The data is shown in Fig. 29.

A broad peak at 1500 MeV was found in the large acceptance WA4 photoproduction experiment at the CERN SPS, as shown in Fig 30. This data is fully consistent with the data of Figs. 17 and 25 of Chapter I and is tentatively interpreted as a single very broad resonance. Data whith high statistics at ALA might be able to reveal a number of fine structures in this spectrum. The same broad structure is confermed at Cornell in a large solid angle experiment (Fig. 31). (20).
The $K^{*}(890)$ excitation curve from ~ 1800 to 2800 MeV has been studied at Cornell, in the sample of events of the tipe $\gamma p \rightarrow K^+K^-\pi^+\pi^- p$ (Fig. 32) (20). Although no strong ϕ signal is seen wi-

thin the still very poor statistics (lower histogram), a few structures in the $K^* K\pi$ spectrum at $\sim$ 1900, 2100, 2400 MeV, (black area in upper histogram) if confirmed with more statistics, suggest that the study of final states involving kaons might be very interesting in the high-energy region of ALA. With reference to the discussion on the baryonium states of Chapter IV, it is interesting to note preliminary data by the same experiment in the $\gamma p \rightarrow \bar{p} p p$ channel, (Fig. 33)(20) which indicate that final states with nucleon pairs might reveal important and maybe resonant structure at the higher ALA energies.

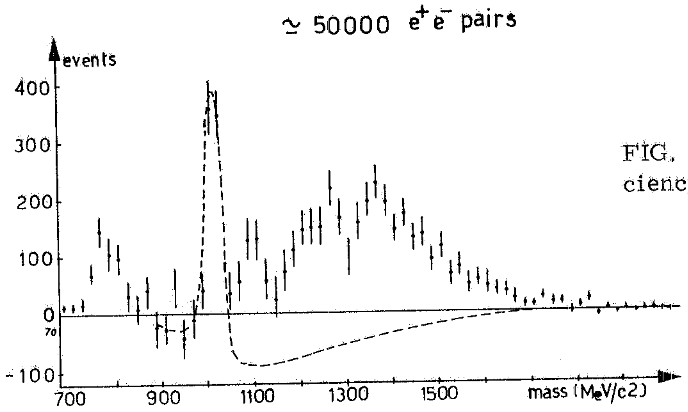

FIG. 27 - Interference spectrum weighted on efficiency of the Desy-Frascati experiment (19).

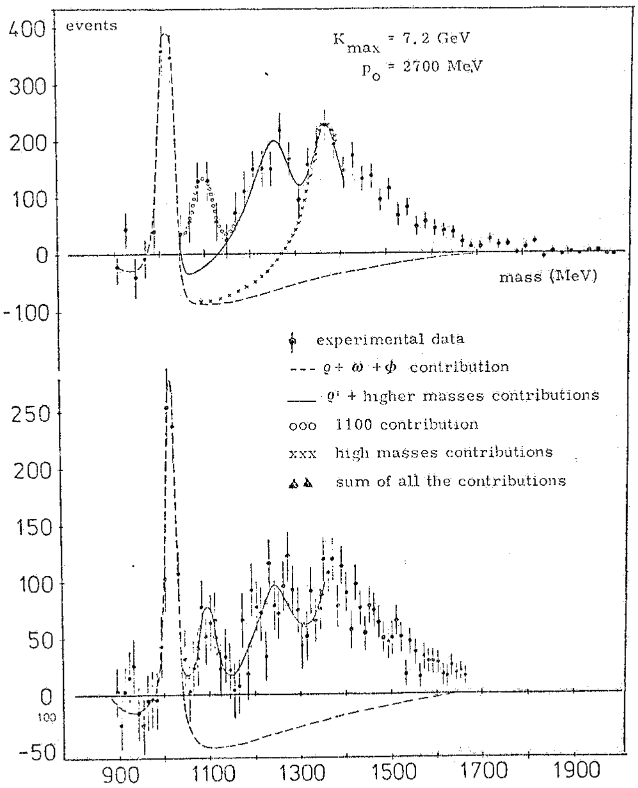

FIG. 28 - Experimental data of the Desy-Frascati experiment compared with what expected if no vector meson existed above the ϕ (lower figure) in the upper figure the high mass asymmetry is splitted into contributions by structures at 1100, 1250, and by a broader term at larger masses (19).

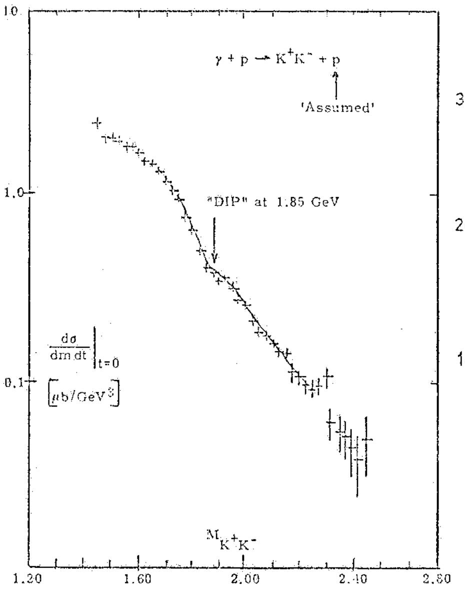

FIG. 29 - Data from the Cornell-Harvard experiment, showing a "DIP" near W = 1.85 GeV, which is naturally correlated to the Adone peak at the same energy.

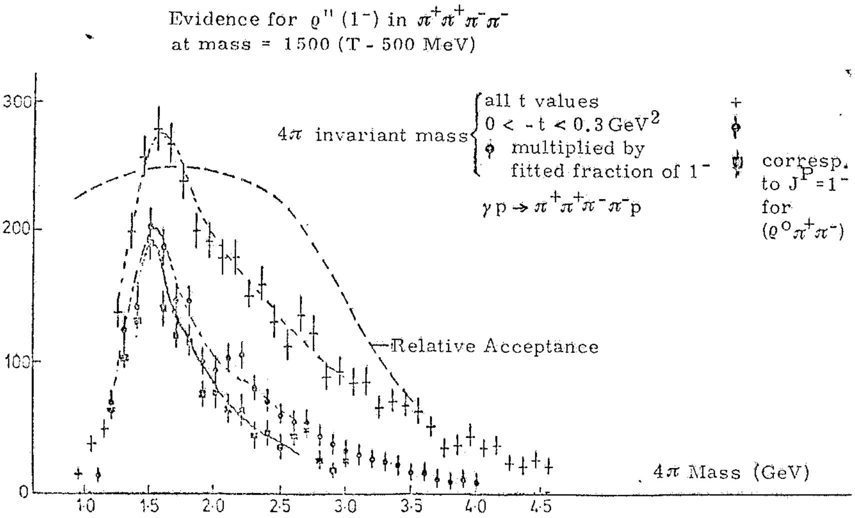

FIG. 30 - Four-pion photoproduction data of the WA 4 experiment.

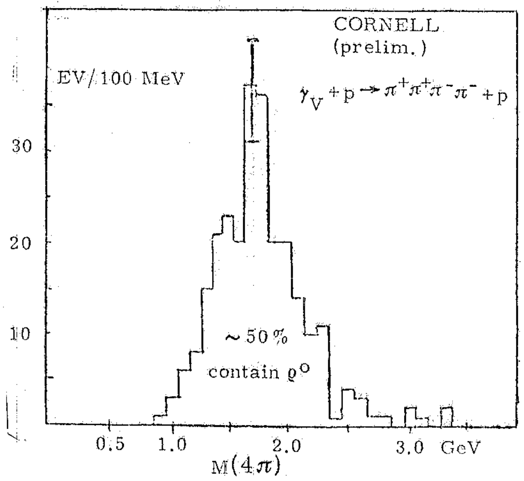

FIG. 31 - Preliminary data of the Cornell "Lame" experiment in the $\gamma p \to \pi^+\pi^-\pi^+\pi^-$ p channel.

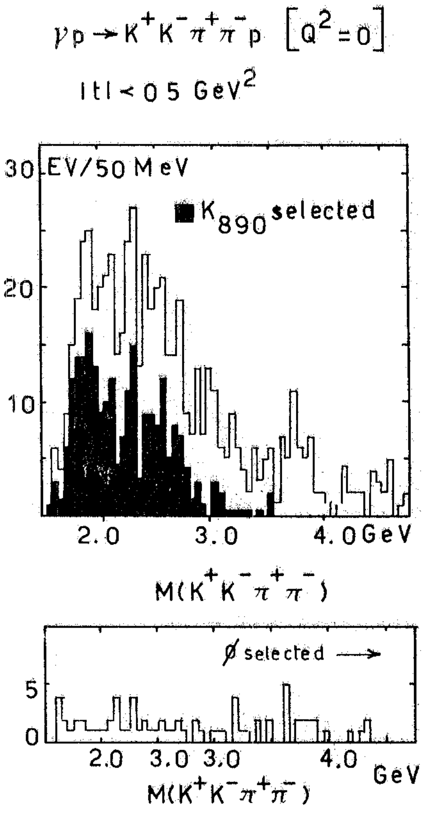

FIG. 32 - Cornell data on $\gamma p \to K^+K^-\pi^+\pi^- p$ channel.

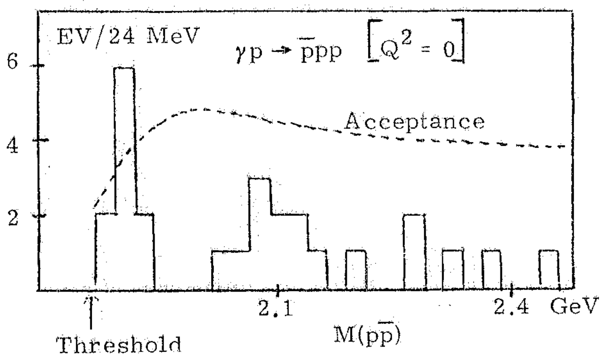

FIG. 33 - "Lame" data on $\gamma p \to p\bar{p}p$

CHAPTER III - NUCLEON-ANTINUCLEON INTERACTIONS.

III. 1. - Experiments on nucleon-antinucleon interactions

A number of experiments on $\bar{p}p$ interaction have provided evidence for resonant or quasi-bound states strongly coupled to the $\bar{p}p$ system. These states are usually referred to as "baryonium" candidates, and their nature is tentatively understood in a number of models, which are reviewed in Chapter IV. Since some of these states (or similar ones that might still be undiscovered) are likely to be observable at ALA/MDA, we shall briefly review the most significant ones among these data.

Inclusive measurements of inelastic $\bar{p}p$ cross-section(21)show a bump at $M(\bar{p}p) \sim 1935$ MeV (the S-meson), as shown in Fig. 34. A comparison of the signal in $\bar{p}p$ and $\bar{p}d$ cross-sections (Fig. 34) allows to conclude that most likely $I = 1$. Since the signal is also observed in σ-elastic $(\bar{p}p)$ (Fig. 35)(22)one can perform a phase-shift analysis, which favours $J = 2$. Therefore the S-meson cannot be seen directly at ALA (it could, however, be seen in a radiative decay of a $J = 1$ state of larger mass). However, there are question marks in this finding, which leave the possibility open that some effect could also be observed at ALA. Since no peak is seen in $\bar{p}p \rightarrow \bar{n}n$ (Fig. 35), which is connected to $\bar{p}p \rightarrow \bar{p}p$ by simple isospin relations, one must either assume that two isospin degenerate states conspire to give zero net effect in charge exchange, or that in the $\bar{n}n$ channel a large background amplitude interpheres negatively with the resonance. In this frame a combined fit to elastic and charge exchange data gives either $J = 1$ and x (elasticity) = 0.37, or $J = 2$ and $x = 0.22$(23). The width of the S is of the order of 10 MeV, which can be understood easier if, being a baryonium state, has a small compling to many-pion states (and small phase-space to $\bar{p}p$).

Broader states of larger mass, called T (2190) with $\Gamma \sim 90$ MeV, and U (2350 with $\Gamma \sim 160$ MeV, are also seen in total and elastic cross-sections (Fig. 36)(24) and might therefore be other members of the baryonium family. The derivation of the quantum numbers of these "states" is by no means unique. In the same approach as above (no signal for T and U is seen in charge-exchange) one gets $J \lesssim 1$ and $x \gtrsim 0.74$ for the T (2190) and $J \lesssim 2$ and $x \gtrsim 0.85$ for U (2350). On the other hand, these bumps are probably due to a sum of various contributions. For instance, a phase-shift analysis of $\bar{p}p \rightarrow \pi^+\pi^-$ (25) gives evidence (Fig. 37) for broader resonances not far from T and U (at $M \sim 2150$ MeV with $\Gamma \sim 200$ MeV and $J^{PL} = 3^{--}$, and at $M \approx 2310$ MeV with $\Gamma \sim 210$ MeV and $J^{PL} = 4^{++}$). It should be recalled, in addition, that $\sigma(\bar{p}p \rightarrow \pi^+\pi^-)$ is about 1% of the total annihilation cross-section (and also therefore much smaller than the signal shown in Fig. 36, and it is a sum of many smaller effects. Maybe therefore the 2190 structure.

It is interesting that strong signals are found in particular channels with small cross-sections, which are not noticeable in inclusive measurements. A CERN experiment using the Omega spectrometer(26) has studied the reaction $\pi^- p \rightarrow (p_F \pi^-)$ resonant $+ (\bar{p}p)$ backward when the forward recoiled proton p_F and the π^- are in a resonant $\Delta(1236)$ or $N^*(1520)$ state. The mass spectrum of backward emitted $(p\bar{p})$ pair is shown in Fig. 38. Three peaks are seen, one corresponding to the S(1930) and two at ~ 2020 and ~ 2204 MeV with widths of the order of 10-30 MeV. The quantum numbers of these possible resonances are an open problem. Baryonium candidates are also found with non-zero strangeness in $K^- p \rightarrow \bar{\Lambda} pK$ at 12 GeV/c, again in the Omega spectrometer (Fig. 39)(27). Peaks in the $(\bar{\Lambda}p)$ system at ~ 2.2, ~ 2.9, ~ 3.1 GeV are seen, which are natural baryonium candidates. It is natural to conclude that the possibility is also open at ALA for pair-production of low-lying strange baryonium members, like $e^+e^- \rightarrow B(2400) \rightarrow \Lambda\bar{\Lambda}$. These states, if they exist, might also decay in a non negligible fraction of cases into $\bar{K}K$. Therefore a scan for final states containing $\bar{K}K$ pairs at ALA can to some extent be considered as a search for members of a particular family of baryonium states (not only for $\phi_{\pm}$ recurrencies !). In this connection we note a bump at $M \sim 2.0$ GeV in the ratio $(p\bar{p} \rightarrow K^0 K^- \pi^+ / \bar{p}p \rightarrow \text{all})$ (Fig. 40(28)). Candidates to quasi-bound baryonium states have been found at CERN in an experiment studying the spectrum of photons emitted in the capture of $\bar{p}$ at rest in hydrogen. The data after subtraction of a large continuous background is shown in Fig. 41(29). Besides the 132 MeV peak due to radiative capture of the π^- contaminating the $\bar{p}$ beam, one observes three peaks which are naturally interpreted as being due to $\bar{p}p \rightarrow \gamma B$ with masses of the bound baryonium of $\sim$1684, $\sim$1664, $\sim$1395 MeV. The observed width is due to the detector resolution. Since the $\bar{p}$ capture is likely to take place in an S-state, some of these "baryoniums" might well have J = 1 and possibly be directly produced in e^+e^-.

In summary, it seems likely that being MDA and ALA able to detect very small cross-sections, a number of baryonium states will either be directly seen in particular channels, or indirectly revealed in a study of radiative decays.

III. 2. - Perspective of the low energy $\bar{p}p$ CERN program

It is being considered at CERN$^{(30)}$ to build within the end of 1982 a storage ring for low energy anti-protons (LEAR). This facility will be provided with an internal jet-gas target allowing experiments on $\bar{p}p$ interactions in flight for c. m. s. energy $2m_p < W < 3.5$ GeV. Also, by slowly ejecting the antiprotons one expects to get a beam with good duty-cycle and $\gtrsim 10^6$ antiprotons per second, that can be stopped in a thin solid or gas target. We briefly review here the main features of this project, and the areas of common interest with ALA/MDA. One such area is first of all the study of baryonium states.

When antiprotons are stopped in low pressure hydrogen gas, $\bar{p}p$ "atoms" are created with orbital angular momentum varying from zero to several units. The capture in a definite angular momentum state is accompained by the emission of monochromatic X-rays. The subsequent annihilation may have a large branching ratio for γ or π decay to quasi-bound baryonium states. In principle, a large solid angle detector can measure at the same time the triggering X-rays, the decay photon or pion, and the annihilation products of the final state baryonium. Those baryonium states which have $J^{PC} = 1^{--}$ or $J^{PC} = 0^{++}, 2^{++}$ are in principle observable, directly, or indirectly in radiative decay, also at ALA/MDA. However, at the present momentum the rate of production of such baryonium states at ALA cannot be reliably predicted. As far as the signature for baryonium is concerned, LEAR has the qualitative advantage that one would know automatically that any state with mass < 2 Mp observed by the above mechanism is strongly coupled to the initial $\bar{p}p$ state and therefore is likely to be baryonium. However, clear-cut prove of baryonium must eventually come from some peculiar decay features, which can be studied at best with MDA. As far as the determination of quantum numbers is concerned, if a state is produced directly or is seen in radiative decay at ALA it must have $J^{PC} = 1^{--}$ or 0^{++}, 2^{++} respectively. LEAR on the other hand will produce baryonium from initial states which can have a large spin, and the orbital momentum of these states is experimentally determined by the X-ray emitted in the $\bar{p}$ capture and the final state baryonium has an orbital momentum which is the same for π and differs by one unit for γ decays. Thus a good efficiency for X-ray detection is essential at LEAR, which is a difficult problem. This facility should see more states than ALA/MDA, but will have to separate them from each other and will have difficulties in determining their spin. In this situation, it seems fair to say that ALA/MDA will compete on equal grounds with LEAR in the study of those baryonium states below threshold which can be produced in e^+e^- annihilation. Of course, the study of additional resonances at ALA which are not baryonium should be much easier and cleaner then at LEAR where one has many more competing channels.

For $W \gtrsim 2$ Mp, $\bar{p}p$ annihilation can also be studied at LEAR, in particular with the internal jet-gas target, and resonant baryonium states can be directly seen either in the elastic or inelastic channels. This gives an advantage to this machine, even if the spin of not strongly coupled resonances to two body channels would remain unknown. An accurate study of those among these states which have $J^{PC} = 1^{--}$ or 0^{++}, 2^{++} can be performed at ALA/MDA (including the branching ratio into baryon pairs). Besides baryonium studies, for $W \gtrsim 2$ Mp one can measure at LEAR the proton form factor in the time like region. This will also be measured at ALA/MDA. For $q^2 =$ $= -4.3$ GeV^2/c (W = 2.06 GeV) the expected rate of events at LEAR using the slow extracted beam is $\sim$1500/day$^{(30)}$, while at ALA ($L \sim 10^{31}$ cm^{-2}s^{-1} and $\sigma_{e^+e^- \rightarrow \bar{p}p} \sim 1$ nb at this energy) one expected about one thousand. It seems therefore that in both experiments the rate will not be a problem. However, it might be easier at ALA to separate collinear non-relativistic $\bar{p}p$ pair from $\pi^+\pi^-$ or K^+K^-, than at LEAR to separate e^+e^- from $\pi^+\pi^-$ (although this is possible, as shown by a CERN experiment$^{(31)}$.

The authors of the LEAR proposal hope to be able to study the spectrum of vector mesons of lower mass than the available c. m. s. energy by exploiting the reaction $\bar{p}p \to \underset{\hookrightarrow e^+e^-}{V}\pi^0$ with the same detector where the reaction $\bar{p}p \to e^+e^-$ is studied. The extimated rate from this reaction is model dependent. The background from hadronic events is difficult to extimate, since several reactions can generate the observed topology 2 ch + 2γ. In the most optimistic case, the output of the measurement would be a mass spectrum of the vector states coupled to e^+e^-, which will have to be compared to the one measured in the photoproduction experiments. The LEAR project cannot, therefore, compete with ALA/MDA in the detailed study of the branching ratios of these states.

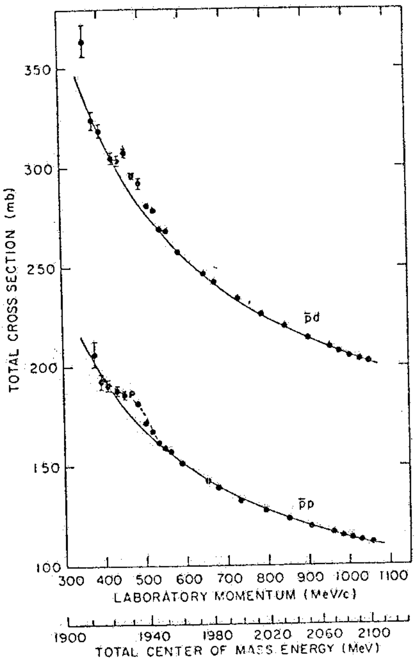

Fig. 34 - $\bar{p}p$ and $\bar{p}d$ (cross-sections(21))

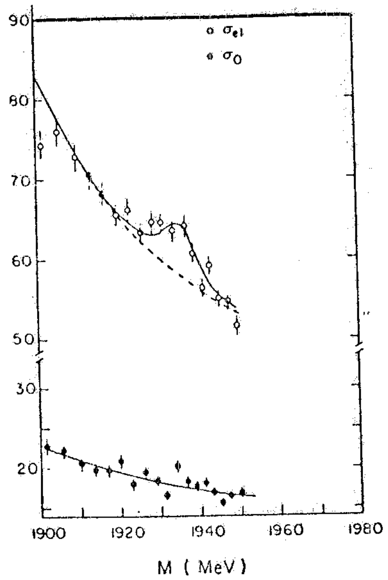

FIG. 35 - A comparison between the elastic and the charge-exchange cross-sections in the S-region.

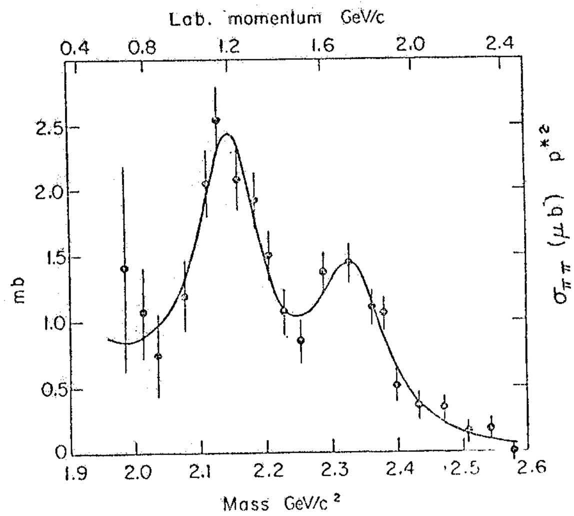

FIG. 36 - $\bar{p}p$ elastic cross-section in the T and U region.

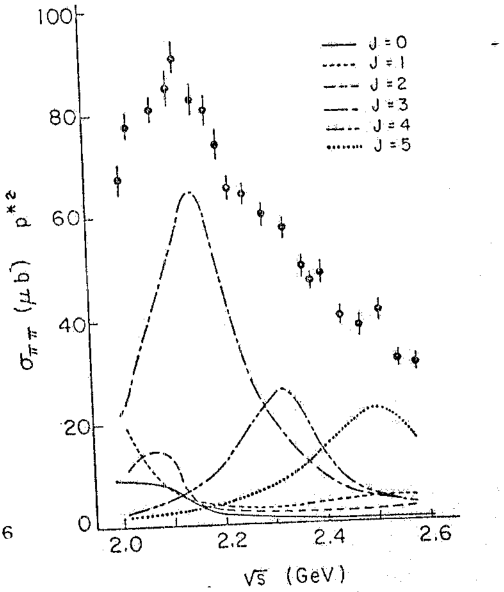

FIG. 37 - Phase-shift analysis of $\bar{p}p \to \pi^+\pi^-$ in T and U region with the data decomposed into contributions by states of different J.

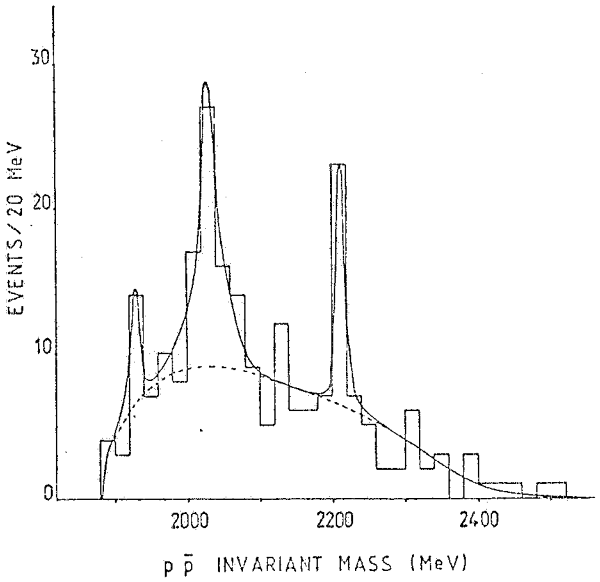

FIG. 38 - Data from the CERN -spectrometer for the reaction $\pi^- p \to p_{fast}\pi^- + (\bar{p}p)_{backward}$.

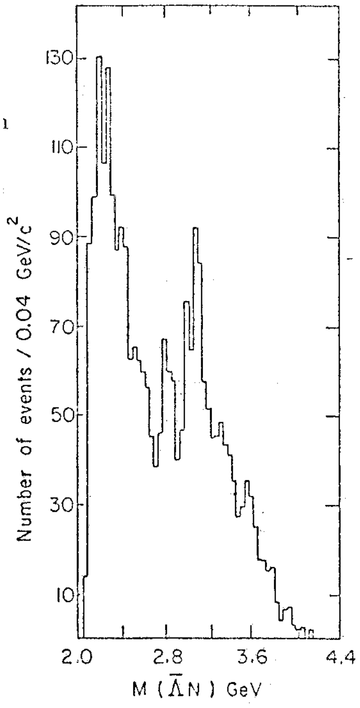

FIG. 39 - $\bar{\Lambda}p$ mass spectrum from $K^-p \to \bar{\Lambda}pX$, where X is p, $p\pi^0$, $N\pi^+$.

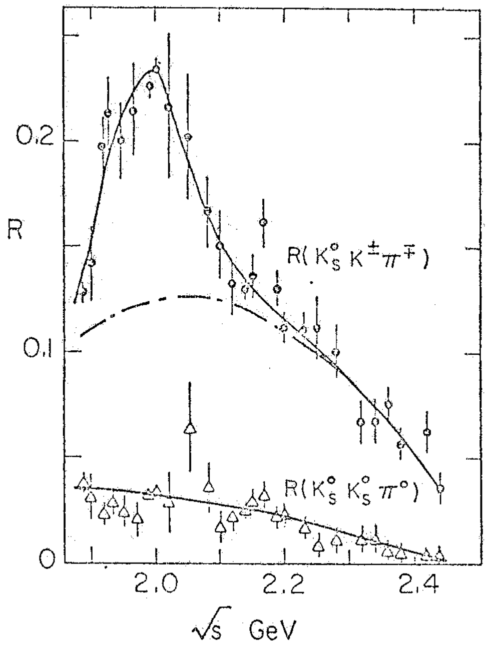

FIG. 40 - Ratio of $\bar{p}p \to K_S^0 K^{\mp} \pi^{\pm}$ over $\bar{p}p \to$ all, and of $\bar{p}p \to K_S^0 K_S^0 \pi^0$ over $\bar{p}p \to$ all.

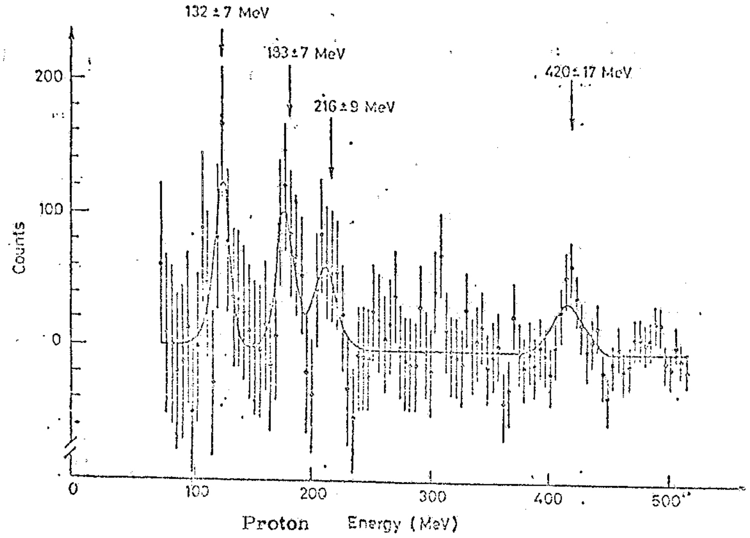

FIG. 41 - γ ray spectrum providing evidence for three narrow states, below threshold in $\bar{p}p$ system.

CHAPTER IV - THEORETICAL EXPECTATIONS FOR THE PHYSICS OF ALA/MDA

We briefly resume in this chapter only the most relevant theoretical arguments and questions which can be elucidated with data from ALA/MDA. Not only this is not intended to be a fully comprehensive summary, but in particular it should not lead to underestimate one of the most important quality features of the project, which is inherent to the jump forward by three orders of magnitude in luminosity x efficiency: the ability to discover new subtle and yet unpredicted phenomena.

IV. 1. - The vector meson recurrencies

Below $W = 1$ GeV, the reaction $e^+e^- \to$ hadrons is dominated by the production of $\varrho(765)$ with $\Gamma = 125$ MeV and $I^G = 1^+$ of $\omega(784)$ with $\Gamma = 11.4$ MeV and $I^G = 0^-$, and of $\Phi(1020)$ with $\Gamma = 4$ MeV and $I^G = 0^-$. In the frame of quark models, these mesons are mixtures of $q\bar{q}$ states, whose radial and orbital excitations are expected to generate families of higher mass mesons with the same I^G and in a number of cases $J^{PC} = 1^{--}$. An approximate mass formula is(32)

$$m_n^2 = m_o^2 + n\Delta^2 ,$$

when Δ^2 is 1-1.2 GeV^2, $n = 0, 1, 2, \ldots$ is the order of the recurrency, and m is the mass of the excited meson. This formula predicts a number of resonances in the energy range of ALA: $M_{\varrho'} \sim 1300$ MeV, $M_{\varrho''} \sim 1600$ MeV, $M_{\varrho'''} \sim 2000$ MeV; $M_{\omega'} \sim 1300$ MeV, $M_{\omega''} \sim 1600$ MeV, $M_{\omega'''} \sim 2000$ MeV; $M_{\phi'} \sim 1450$ MeV, $M_{\phi''} \sim 1750$ MeV, $M_{\phi'''} \sim 2150$ MeV. The coupling of the recurrences to e^+e^- can be predicted only on the basis of dinamical models. Typical values for the ϱ-recurrencies are(33)

$$\Gamma_\varrho = 125 \text{ MeV} , \qquad \Gamma_{\varrho'} = 180 \text{ MeV} , \qquad \Gamma_{\varrho''} = 350 \text{ MeV} .$$

SU_3 relations can be used to predict Γ_{ω_n}, Γ_{ϕ_i} giving values like

$$\Gamma_{\omega'} \sim 470 \text{ MeV} , \quad \Gamma_{\omega''} \sim 560 \text{ MeV}, \quad \Gamma_{\phi'} \sim 40 \text{ MeV} , \quad \Gamma_{\phi''} \sim 280 \text{ MeV} .$$

These figures, however, are largerly uncertain and should be taken only as expected order of magnitudes for these parameters in the quark model.

Infinite series of resonancies of the ϱ, ω, ϕ families are also predicted in Regge models(34); in particular while the main trajectory gives rise to recurrencies of larger mass and larger spin, each daughter trajectory contains a member of mass larger than the ω and $J^{PC} = 1^{--}$. In the case of equally spaced daughter trajectories with the typical slope in the spin versus q^2 plane $d\alpha/dq^2 \sim 1$ GeV^{-2}; the mass formula is again

$$m_n^2 = m_o^2 + n\Delta^2 ,$$

with $\Delta^2 \sim 1$ GeV^2, viz. very similar, even numerically, to what obtained in quark models. By making use of a number of experimental indications from Adone and DCI and based on the extended vector dominance model as well as on quark model considerations, Greco has discussed possible values for the decay widths of these recurrencies(35), which depend heavily on the assumed dinamics like for instance dominant $\varrho\pi\pi$ or $\varrho\varepsilon$ or $\omega\pi\varrho_n$-decay. One gets estimates like

$$\Gamma_{\varrho'} \sim \Gamma_{\varrho''} \sim 100 \text{ MeV} , \qquad 100 \text{ MeV} \lesssim \Gamma_{\omega'} \sim \Gamma_{\omega''} \lesssim 400 \text{ MeV} ,$$

$$25 \text{ MeV} \lesssim \Gamma_{\phi'} \lesssim 50 \text{ MeV} , \qquad 30 \text{ MeV} \lesssim \Gamma_{\phi''} \lesssim 100 \text{ MeV} .$$

Again, one should take these values as guidelines, while a better theoretical understanding of the real phenomena can only be based on better experimental data, in particular on detailed measurements of the energy dependence of the various final states.

The peak cross-sections are expected to vary with the order of the recurrency like(35)

$$\sigma_{n,\,\mathrm{peak}} \simeq \left(\frac{m_o}{m_n}\right)^3 \frac{\Gamma_o}{\Gamma_n} \quad \sigma_{o,\,\mathrm{peak}}$$

Although the expected values depend on the rather unknown Γ_n's, it is significant that in all cases one predicts σ_n's of 10-100 nb. No matter which the dominant decay channel is, MDA should be able to perform the job easily.

With the experimental picture available at present, there is no interpretation of the data that can be made convincing. The bump at M = 1266 MeV with $\Gamma \sim$ 11 MeV of the Desy-Frascati experiment could be the ϱ'. However, while an anomaly at about this energy is found in the pion form factor measured at Novosibirsk(36) (Fig. 42)no signal is seen in $\sigma(2\pi^+ 2\pi^-)$ and data on $\sigma(2\pi^0\pi^+\pi^-)$ and $\sigma(6\pi)$ are too poor to be of any use. The bump seen at W $\sim$ 1500 MeV in $\sigma(e^+e^- \rightarrow 2\pi^+ 2\pi^-)$ (Fig. 17, Chapter I) as well as in photoproduction $\gamma \rightarrow 2\pi^+ 2\pi^-$ (Fig.30, Chap. II) which is consistent with the large interpherence at $m_{e^+e^-} \gtrsim 1400$ MeV in the Desy-Frascati experiment (Fig. Chap. II) could well be dominated by the ϱ''. However, a separate study of the different final states ($\varrho\pi\pi$, $\omega\pi$, etc.) has not been possible and the real signal is most likely mixed with a large non-resonant background. One of the bumps in $e^+e^- \rightarrow 3\pi$ or in $e^+e^- \rightarrow 5\pi$ seen at DCI (Fig. 25, Chapter I) might be the ϱ'' (at m $\sim$ 1750 MeV), but the statistical significance of the signal is marginal, and moreover what about the second peak at lower mass?

The structure marginally seen at Adone at W $\sim$ 1500 MeV is where the ϕ' is expected. However the signal is too narrow ($\Gamma <$ 5 MeV), such that Greco tries to explain it as an orbital excitation of the $s\bar{s}$ system, leaving the point open for a jet undiscovered nearly ϕ'(35). The signal at W$\sim$1820 MeV (Fig. 12, Chapter I) might be the ϕ'' (although it is very narrow too, but there is no prove for this interpretation, also because there is no significant signal in inclusive K-production. If one forgets about theoretical prejudices favouring very large ω_n-widths, this signal might well be the ω''. The 2130 MeV signal at Adone (Fig. 8, Chapter I) is commonly considered to be the ϕ''', but any firm interpretation should await more detailed experimental information. It can be anticipated that the true picture will only emerge by the future data interpreted in critical close connection with the theoretical models.

We shall now discuss in some more detail the energy dependence of the cross-section for $e^+e^- \rightarrow$ hadrons to be expected at ALA in presence of a number of resonances whose widths increase with energy. Quite in general(37), the process of hadronic production in e^+e^- annihilation is described by a diagram like

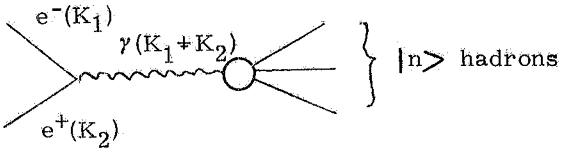

where K_1, K_2 are the electron and positron four momenta. The matrix element for this process is

$$M = \alpha\, \bar{w}(K_2)\, \gamma_\mu\, u(k_1)\, \frac{G^{\mu\nu}}{s} \langle n \,|\, j_V \,|\, 0 \rangle$$

where $s = q^2$, and $q^\mu = K_1^\mu + K_2^\mu$. As a consequence of the continuity equation of the electromagnetic current $\partial_\mu J^\mu = 0$ the current and the four-momentum transfer are orthogonal, $q^\mu J_\mu = 0$. Since the space component of q is zero ($K_1^4 = -K_2^4 \simeq E$), this equation says that $q^o J_o = 0$, viz. $J_o = 0$ (since $q^o = 2E$). Thus the e.m. current is purely space-like. Since the vector space-like part of the e.m. current has $J^{PC} = 1^{--}$ and $|0\rangle$ has $J^{PC} = 0^{++}$, the state $J^\mu|0\rangle$ has $J^{PC} = 1^{--}$. The only matrix elements $\langle n|J^\mu|0\rangle$ which can be different from zero are those for which $\langle n|$ has $J^{PC} = 1^{--}$. Therefore we expect the hadronic cross-section to be dominated by production of vector mesons, by their tails and their recurrencies. For a given vector final state with mass m one writes conventionally

$$\langle V|J^{\mu}|0\rangle = \varepsilon^{\mu}(q)\,\frac{m^2}{2\beta_V}\ ,$$

where β_V is the adimensional coupling constant and the polarization four-vector, $\varepsilon^{\mu}(q)$ is directed along J^{μ}. The cross-section is derived by averaging over the initial and summing over the final state spin orientations, and by multiplying by the one-particle phase-space. One obtain in the zero-width approximation (37)

$$\sigma(e^+e^-\rightarrow V) = \frac{4}{3}\,\frac{\pi\alpha^2}{s}\,\frac{3\pi m^2}{\beta_V^2}\,\pi\,\delta(s-m)^2\ , \qquad \text{where}\ \ \frac{4}{3}\,\frac{\pi\alpha^2}{s} = \frac{85\ \text{nb}}{s(\text{GeV}^2)}\ .$$

For a resonance represented by a Breit-Wigner distribution with finite width Γ one has :

$$\sigma_{e^+e^-\rightarrow V} = \frac{4}{3}\,\frac{\pi\alpha^2}{s}\,\frac{3\pi m^2}{\beta_V^2}\,\frac{m\Gamma}{(s-m^2)^2+m^2\Gamma^2}\ .$$

The coupling constant β_V^2 is uniqualy related to the width of the vector meson into e^+e^- which is proportional to $|M(e^+e^-\rightarrow V|^2$ in a similar way as $\sigma(e^+e^-\rightarrow V)$. One gets

$$\Gamma(V\rightarrow e^+e^-) = \Gamma_{ee} = \frac{\pi\alpha^2 m}{3\beta_V^2}\ .$$

One can therefore rewrite

$$\sigma_{e^+e^-\rightarrow V} = \frac{4}{3}\,\frac{\pi\alpha^2}{s}\,\frac{9\,\Gamma_{ee}\,m}{\alpha^2}\,\frac{m\Gamma}{(s-m^2)^2+(m\Gamma)^2}\ .$$

The peak cross-section is :

$$\sigma_{\text{PEAK}} = 12\pi\,\frac{B_{ee}}{m^2}\ , \qquad \text{where}\quad B_{ee} = \frac{\Gamma_{e^+e^-}}{\Gamma}\ .$$

The partial cross-section into a particular decay channel of branching ratio B_f is σB_f. In particular $B_f = B_{ee}$ if one isolates the vector meson decays into e^+e^-. One sees here how one can exploit measurements of total decay rate and partial rate into e^+e^- to derive Γ and Γ_{ee} for mesons narrower than the machine energy spread. Indeed

$$\int d(\sqrt{s})\,\sigma(e^+e^-\rightarrow V\rightarrow \text{all}) = \frac{6\pi^2}{m^2}\,\Gamma B_{ee} = \text{cm}^2\text{GeV}\ , \qquad \int d(\sqrt{s})\,\sigma(e^+e^-\rightarrow V\rightarrow e^+e^-) = \frac{6\pi^2}{m^2}\,\Gamma B_{ee}\ ,$$

the unknowns in there two equations being only Γ and B_{ee}. When many vector mesons are produced in the same energy region, as expected at ALA, the cross-section is the sum of the various contributions, including possible interpherence terms. When the width of the resonances becomes compairable to their masses, which is possibly true at the top ALA energies, the ratio $R = \sigma h/\sigma_{\mu\mu}$ tends to

$$R \sim \sum_i \frac{9\pi}{\alpha^2}\,\frac{m_i\,\Gamma_i\,e^+e^-}{\Delta^2}\ ,$$

and one expects $R \sim 2.5$ below $W = 3$ GeV in the V. D. M. This is compatible with the recent Adone results (fig. 7, Chap. I). On the other hand, the asymptotically free quark models predict

$$R \quad \underset{i}{} \; Q_i^2 \; (1 + \frac{\text{constant}}{\ln(s/\ \ ^2)})$$

where Q_i are the constituent quark charges of any colour. For three light quarks of three colours, as appropriate for energies increasing from W$\sim$ 1. 8 to W$\sim$ 2. 4 GeV, one expects R to tend to the value of 2 form above. This is fully compatible with the Adone data. Although the top ALA energy of only 2. 4 GeV will be a limitation in this context, it is expected that accurate absolute measurements of R from W $\sim$ 1. 8 to W = 2. 4 might contribute to elucidate this point.

IV. 2. - Baryonium models.

The existence of new families of hadrons which have been given the general name of baryonium states, is predicted both in nucleon-nucleon potential and in dual models. I. S. Shapiro (38) and collaborators have analized the data on nucleon-nucleon interaction at low energy and derived parameters for an effective potential, by taking into account $\pi, \eta, \varrho, \omega$ as well as 2π and 3π non-resonant exchanges. The various contributions to the potential are written as

$$V_i = g_i^2 \; \Omega_i \; \frac{e^{-\mu_i r}}{r}$$

(μ_i = effective mass of the exchange) where the form of the real operator Ω_i is uniquely specified by the quantum numbers of the exchanged particle. It is empirically found in the fit that the coupling constant g_ω^2 of the repulsive ω-exchange term is very large. In a model in which the nucleon-nucleon potential is generated by exchange of non-strange mesons, one derives a very simple relationship between the NN and the $\overline{\text{NN}}$ potentials: when passing from NN to $\overline{\text{NN}}$, the amplitude contributed by G-odd exchange terms change sign, and those contributed by G-even exchanges remain unaltered. Therefore one can predict the NN potential in terms of the NN one. In particular the ω-exchange contribution takes a very important role because it is strong and attractive in $\overline{\text{NN}}$, such that a number of resonant and bound states an predicted. Of course, these states cannot be stable because annihilation will eventually kill them. Indeed, an additional contribution to the scattering potential is given in the NN case by the annihilation graph

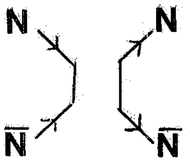

Since this corresponds to an exchange of two nucleon masses, one expects that the modifications generated by annihilation on the $\bar{\text{N}}$N potential come in at a distance $1/2m_n \sim 0,1$ fermi. This is 1/3 of the characteristic distance for ω-exchange and therefore the ability of the potential to generate bound and resonant states is preserved. Shapiro et al. have approximated the effect of annihilation by means of an absorbitive Saxon-Woods potential

$$V_{ann} \sim - i \, W_o/(1 + e^{r/r_o})$$

with r_o of the order of 0, 1 f. Indeed, a fit to low energy $\overline{\text{N}}$N scattering and charge-exchange data gives $r_o \simeq$ 0, 17 f while Wo $\sim$ 8 GeV.

The parametrization of the global $\bar{\text{p}}$p potential obtained in this way has allowed to derive on order-of-magnitude prediction for the spin vs. mass trajectories of both I = 0 and I = 1 baryonium families, which are shown in fig. 43 and 44 (39).

It is noticed that several states with J = 1 exist in the ALA energy region, while several more could be reached by radiative transitions.

More recent calculations by the same group predict a group of resonant states centered at W ∼ 2.0 GeV decaying predominantly into $\bar{N}N$, $\bar{N}N\pi$, $\bar{N}^*N\pi$, etc., as well as a group around 2.4 GeV decaying predominantly into $\Lambda\bar{\Lambda}$, $\Lambda\bar{\Lambda}\pi$, $\bar{\Sigma}\Lambda\pi$, etc. Typical resonance widths and separation between nearby resonances are 50 MeV. The prediction is made for the branching ratio for radiative transitions from atomic to resonant and bound states to be of the order of 10^{-3}. This process can explain some photon excess observed in $\bar{p}p$ annihilation. On the other hand, if this excess is due to transitions between baryonium states, ALA/MDA should be able to find the radiative photons. A popular quark model of baryonium is due to Chan Hong-Mo and collaborators (40), in which the new states are predicted based on the only assumption that all multi-quark states with zero total colour can in principle exist in nature. With $\bar{q}q$ one gets in this way all mesons, with qqq (or $\bar{q}\bar{q}\bar{q}$) all hadrons. Since no mesons are found which Q = 2 (nor barions with Q = 3) one has taken in the past the attitude that four quark states like $qq\bar{q}\bar{q}$ are not bound in nature, since they would naturally lead to Q = 2 states. However, if one consider than states as bound objects of qq and $\bar{q}\bar{q}$, one can make a model in which a number of hadronic states are predicted that bear close resemblance to what experimentally found and discussed in Chap. III. For instance, these states would not be able to decay into mesons without violating the OZI rule, while they would naturally decay into barion pairs.

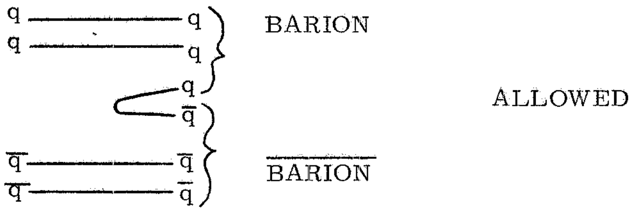

This simple rule is able to predict directly that these states are narrow below $\bar{N}N$ threshold, and have normal hadronic width (∼ 100 MeV) well above threshold. They may legitimally be called baryonium because of the large decay rate into $\bar{B}B$; on the other hand, being 4-quark states, they are not bound states of two barions (as in the potential model), such that Chan et al. like to call them rather "diquoniums". Since q is a colour triplet, a qq system can be in a $\bar{3}$ or 6 representation, while $\bar{q}\bar{q}$ can be either 3 or $\bar{6}$. If the net colour must be zero in physical hadrons, one can have two diquonium families, $(qq)_{\bar{3}}(\bar{q}\bar{q})_3$ and $(qq)_6(\bar{q}\bar{q})_{\bar{6}}$. These families are called True and Mock diquonium respectively, and in fact it is only the T-diquonium that can easily decay into barion pairs as discussed above. M-diquonium, if colour is a good quantum number, cannot do it, since a colour 6-set and a colour triplet cannot combine to give a zero colour barion.

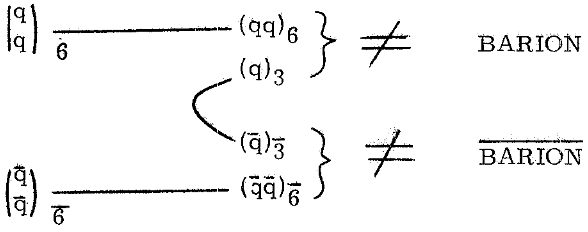

Because of this assumed property, the existence of the M-barionium would be considered by the authors of the model as the very prove that colour is a genuin quantum number of hadronic interactions. M-diquonium is narrow (Γ = 10 ÷ 20 MeV) both above and below the $\bar{N}N$ threshold because it can decay into mesons only by violating the Zweig rule.

The predicts $J(M^2)$ distribution for T-diquonium states generated by u and d quarks only is shown in fig. 45.

A spin dependent interaction is introduced to separate members of the family in which both (qq) and ($\bar{q}\bar{q}$) are in a I = 1 state. A number of predicted states correspond to the peaks discussed in Chap. III.

The predicted $J(M^2)$ distribution for M-diquonium is plotted in fig. 46. There is no really good experimental candidate for a member of this family yet. The signature for such states is to be found not only in the narrow width but also in specific decay channels. It is found in the model, as a consequence of the assumption that colour rearrangement is avoided as long as possible, that higher spin states decay mostly into lower states of the same family by pion emission. Therefore specific predicted signatures are $B\bar{B}$, $B\bar{B}\pi$, $B\bar{B}\pi\pi$, etc. , with one or more monocromatic pions.

A number of both T and M-diquoniums states have the right quantum numbers for being directly coupled to a photon. The predicted spectrum is shown in fig. 47 and compaired with the DCI peak at 1660 MeV, with the Adone peak at 1820 MeV and with the data of the Omega photoproduction experiment. Although specific predictions should not be taken too seriousely, it is clear that in the general frame provided by this model many interesting phenomena are anticipated and submitted to the decisive test of ALA/MDA.

A dinamical quark model of barion-barion scattering has been developed by Rossi and Veneziano (41) in which families of exotic hadrons (some of which including four quarks) are predicted. Quarks enclosed in barions are assumed to be bound toghether by gluons via a junction

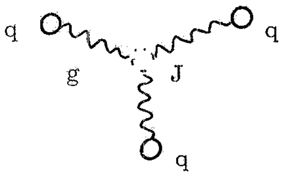

and $\bar{B}B$ scattering is described by a number of dual diagrams, in which states with 4 quarks and 2 junctions ($M^J{}_4$), 2 quarks and 2 junctions ($M^J{}_2$), 2 junctions only ($M^J{}_0$, a gluon ball) as well as regular mesons can be exchanged in the t-channel (see fig. 48). All these states are directly coupled to $\bar{B}B$ states and can therefore be considered "barioniums". The Zweig rule forbids the decay of $M^J{}_4$ into mesons, as illustred at the bottom of fig. 48 and are therefore expected to be narrow below $\bar{N}N$ threshold. The above exchange generate Regge trajectories which are tentatively estimated in the model as shown in fig. 49. One sees that the masses of the J = 1 members of these "barionium" families, including the gluon ball, are including in the ALA energy region.

In conclusion, no matter whether a potential or a quark model is adopted, one is brought to conclude that ALA/MDA have a good chance to pin-down a significant sample of the expected baryonium states.

IV. 3. - Coloured gluons and quarks.

New foundamental particles coupled to e^+e^- are predicted in the unified gauge theory of quarks and leptons developed by Pati and Salam (42). In this theory neither quarks nor gluons or colour in general are confined. Quarks have unit charge and are unstable against decay into leptons, with lifetimes so short ($\tau \lesssim 10^{-11}$s) that they would have excaped detection until now. An octet of colour vector gluons is predicted, whose two neutral members can mix into two neutral gauge gluons ($\tilde{U}$ and V^c), one of which ($\tilde{U}$) is coupled to e^+e^- similary to the photon

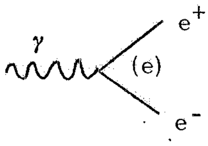

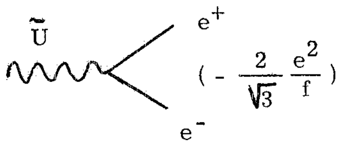

In real life two physical particles could exist coupled to e^+e^- with weights $\cos^2\xi$ and $\sin^2\xi$:

$$\underline{\tilde{U}} = \tilde{U}\cos\xi - V^o\sin\xi \ , \qquad \tilde{V} = \hat{U}\sin\xi + V^o\cos\xi$$

The dominant decay modes of $\tilde{U}$, with numerical values for the widths estimated in a particular model and for $m_{\tilde{U}} = 1 \div 2$ GeV, are listed in the following table

$\tilde{U} \longrightarrow e^+e^-$ or $\mu\mu$	$\Gamma =$	6 to 30 KeV
$\eta'\gamma$		40 to 1000 KeV
$2\pi\gamma, 4\pi\gamma\gamma$, KK		50 to 500 KeV
$3\pi, \varrho\pi, 5\pi$, KK		10 to 1000 KeV
$2\pi, 4\pi$,		10 to 1000 KeV

Thus the leptonic branching ratio is of the order of percents, and the overall radiative branching ratio is very large ($\gtrsim 30\%$). The above decay channels are either forbidden or very small for the V^o. This means that one or two resonances could exist in the mass range 1 - 2 GeV having (with splitting of the order of $\frac{1}{10}\, m_{\tilde{U}}$ and relative weights $\cos^2\xi$ and $\sin^2\xi$) appreciable branching ratios into e^+e^- and $\mu^+\mu^-$ and large branching ratios for radiative decays. There are several clear signatures directly accessible to experiment, first of all the exceptional rate of γ-decays (notice also the large two-body $\eta'\gamma$ channel), and also the resonant behaviour into odd number of pions, as well as into even number of pions and into kaon pairs, which can be well checked in a large solid angle detector like MDA and are inconsistent with any vector meson recurrency. The total width of $\tilde{U}$ is estimated to be at least 100 KeV in this model, which would lead (using $B_{ee} \sim$ percents and the formula of page 18) to an integrated cross-section of 10 μbarn x MeV. This is a very large signal ($\sim J/\psi$) which would be very easily detectable at ALA/MDA. The authors of ref. (42) note that if the narrow structure observed at Adone at $M \sim 1500$ MeV is one of these coloured gluons, it must be the weakly coupled one ($\sin^2\xi \sim \frac{1}{100}$), such that the second stronger partner is expected in the region $M \sim 1300 \div 1400$ MeV. It is interesting to note that no search for narrow resonances (nor in fact any measurement of σ_h even at VEPP 2 M, see fig. 17) was made at Adone in this energy region. The 1100 MeV structure observed in the Desy-Frascati photoproduction experiment can also be considered a candidate vector gluon, although one may feel that its width is rather large. It should be recalled that both the absolute magnitude of Γ and Γ_{ee} are estimated in the above model under very specific dinamical assumptions: Γ_{ee} might be smaller if finite mass renormalization corrections are not negligible and Γ might be larger, up to a factor of five in the estimate of the authors. Therefore the actual signal in e^+e^- could be well smaller and not as narrow as indicated in the previous example, but in any case detectable and clearly identifiable at ALA/MDA.

As well as coloured gluons, coloured quarks of unit charge or coloured or $q\bar{q}$ mesons can be produced free in the Pati-Salam model. These hypotetical particles can be of interest for ALA/MDA if their mass is of the order of $0.5 \div 1$ GeV. From ref. 42, one estimates that $\tau \gtrsim 2.10^{-9}$sec in this case, which would leave the possibility open for short collinear tracks to be observed in MDA, followed by decay inside the detector. These events with unit charges should be easily identified (the possibility for similar events and fractional charges will be discussed in the following in connection with the quark-imps model). The decay signature of a reaction $e^+e^- \rightarrow q^+q^-$ depends on the quark colour involved: for instance typical decays are $q_{\text{blue, yellow, red}} \longrightarrow \nu$ + mesons
and $q_{\text{red}} \longrightarrow$ lepton$^{\pm}$ + mesons or lepton$^{\pm}$ + neutrinos
and also, if $m_{\tilde{U}}$ happens to be smaller than m_q
$q_{\text{red}} \longrightarrow$ gluon$^{\pm}$ + neutrino $\longrightarrow$ lepton$^{\pm}$ + 2 neutrinos.

Although final states with neutrinos and mesons will show missing energy and momentum in MDA, it looks unlikely that such an indirect signature might be of great importance, because it can be faked by a number of detector inefficiencies. More interesting are the decays involving charged leptons, which will give rise to anomalous $e^{\pm}\ \mu^{\pm}$ events as those observed at SPEAR. It is remarkable that if indeed $m_{\tilde{U}} \lesssim m_q$ and if $m_{\tilde{U}} \lesssim 1$ GeV, the final state charged lepton generated by the two-step process $q^{\pm} \to U^{\pm} + \nu \to e^{\pm} + \nu + \nu$ has a momentum distribution which is little different from a genuine tree-body decay spectrum, as in a heavy lepton decay. Along these lines it is argued in ref. (12) that the anomalous $e\,\mu$ events of SPEAR might be interpreted as being due to q^+q^- production and decay. Of course, this argument is now very weak in this specific case, because of the increased evidence for production of τ at SPEAR and DORIS: however, in the ALA energy region the possibility for $m_q \leqslant 1.2$ GeV, $M_{\check{U}} \sim 1.1$ GeV is in principle still open. The corresponding e events have been looked for at Adone (ref. 11, Chap. I), but since the branching ratio for these decays are hardly predictable both this negative result and the lack of $e\,\mu$ events below $W \sim 3.7$ GeV at SPEAR and DORIS do not completely remove the interest for a similar search at a very luminous machine as ALA. Finally, a sizable branching ratio for $q_{red} \longrightarrow q_{yellow,blu} + \gamma$ is also predicted in this model, which adds an increased interest for an accurate study of monocromatic photon with MDA.

IV. 4. - Indefinite mass particles.

B. M. Coy and T. T. Wu have recently discussed the possibility that quarks might be indefinite mass particles (imps) as those which are encountered in two dimensional Ising models (43). Since there is no basic quantum-mechanical argument that can exclude this possibility, one is led to wonder either quarks of fractional charge are produced free in nature but have not been discovered yet because of the peculiar properties of imps. If this is so, the principle of confinement which is insert in current quark-models would simply express the fact that untill now the experimentalists did not look for quarks in the right way.

If a field has free particles (asymptotic states) there must be corresponding poles in the field propagator at $q^2 = m^2$. If there are no asymptotic states (confinement) there are two distinct possibilities consistent with no poles in the propagator:

a) the propagator is a simple function without discontinuities in the complex q-plane, like a polinominal, an exponential, etc.

b) the propagator has a cut on the real positive axis, which can be considered like a sequence of poles with infinitely small separation from each other and with zero residues.

In case b), one can consider that the carrier associated to the field has an infinite number of states with a continuos mass distribution. A quantum particle, of this type, called imp (indefinite mass particle) in ref. (43), will acquire a definite mass when is produced. For instance, one may have a light quark which can have a mass from $\frac{1}{3} M_{proton}$ to $\frac{1}{3} M_{proton} + 1 \div 2\, M_{pion}$. A peculiar feature of imps is that after production over a region of linear size $\sim$ 1 fermi (as it is typical of strong interactions) their geometrical dimensions must grow indefinitely with time (as long as they are not captured in matter) while they preserve their remaining properties (mass, momentum, total charge etc.). This feature is imposed by the absence of asymptotic states. In the quark-imp case, the particle after production in a very small volume will have to tend to acquire its natural infinite size, just because its natural levels are an infinite series with zero spacing. Although the speed and law of growth of imps is hardly predictable, they will acquire after some time dimensions of the order of the optical wave lengths (10^3 Å), after which they would cease ionizing and would not be observable in scintillators, spark chambers, bubble chambers, nuclear emulsion and so on. Detection of particles of such a peculiar property requires special attention: it is argud in Cap. I that if $l_0 = c\,\tau \lneq 10$ cm (l_0 = natural ionization length) they would have excaped detenction in previous experiments, while they would be detectable at ALA/MDA (for a quark mass of $\frac{1}{2}$ GeV) up to a confinement factor of about 10^{-4}. The characteristic signatures of quark-imps which can be exploited in MDA are

1) one track (or possibly two tracks, which would be back-to-back in two body production) which suddenly disappears without interactions or increased ionization at the end of range
2) 1/9 or 4/9 ionization power of a normal particle of the same velocity
3) continous bending in magnetic field which can be signalled at distancies larger than the ionization path by nuclear interactions of the outgoing imp.

The exploitation of these features is discussed in detail in Chap. VII. Although the idea of quark-imps may look rather dairing, the novelty of the idea, coupled to the peculiarity of the experimental signatures as well as the importance of a possible discovery indicate that this is addition relevant field of interest for research at ALA/MDA.

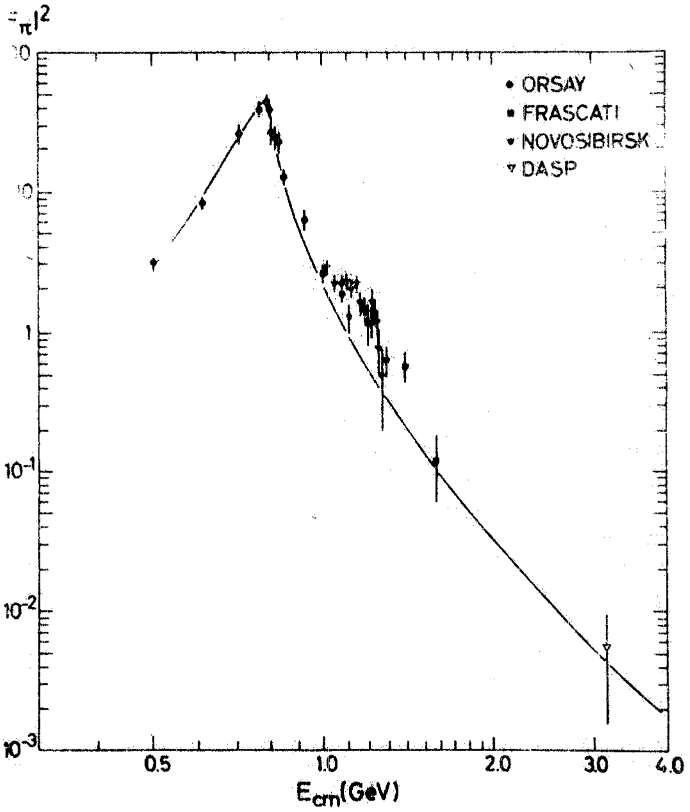

FIG. 42 - Pion form factor.

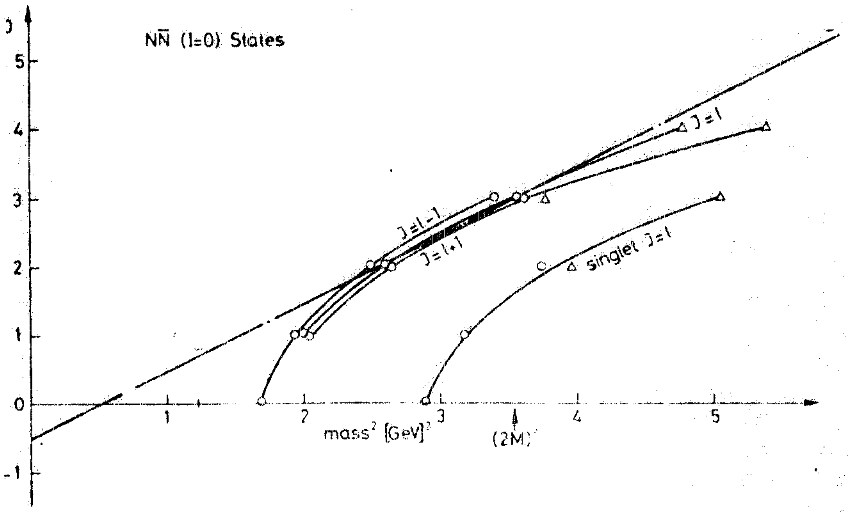

FIG. 43 - NN states for I = 0 trajectories.

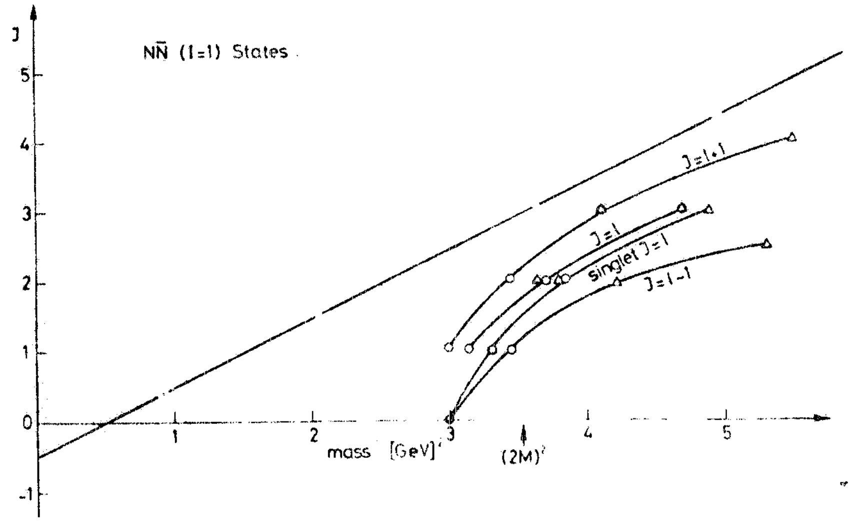

FIG. 44 - NN states for I = 0 trajectories

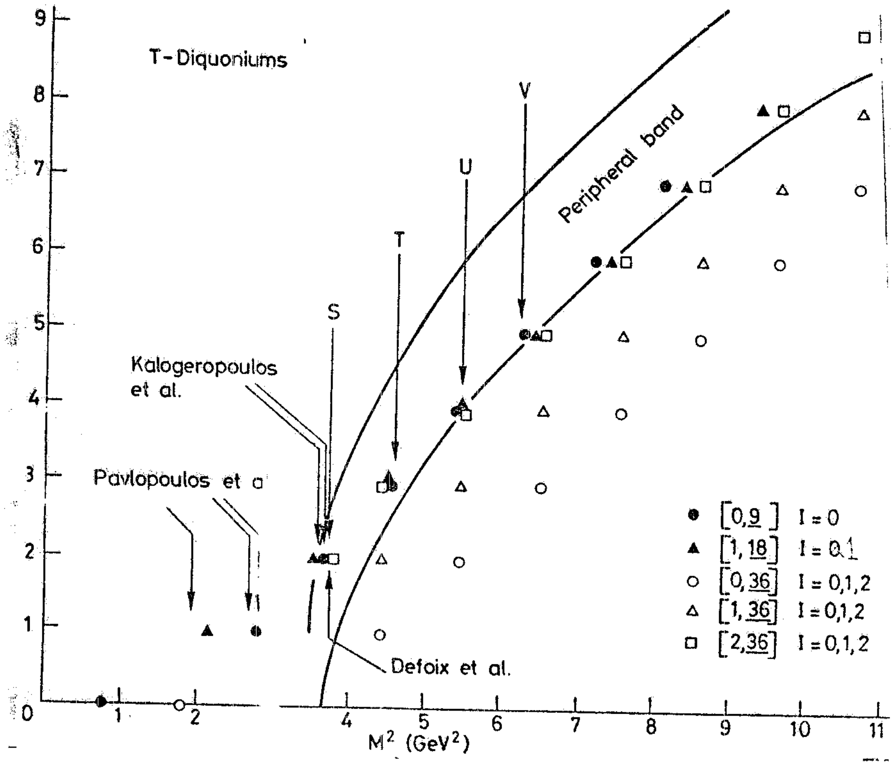

FIG. 45 - Predicted distribution for T-diquuonium.

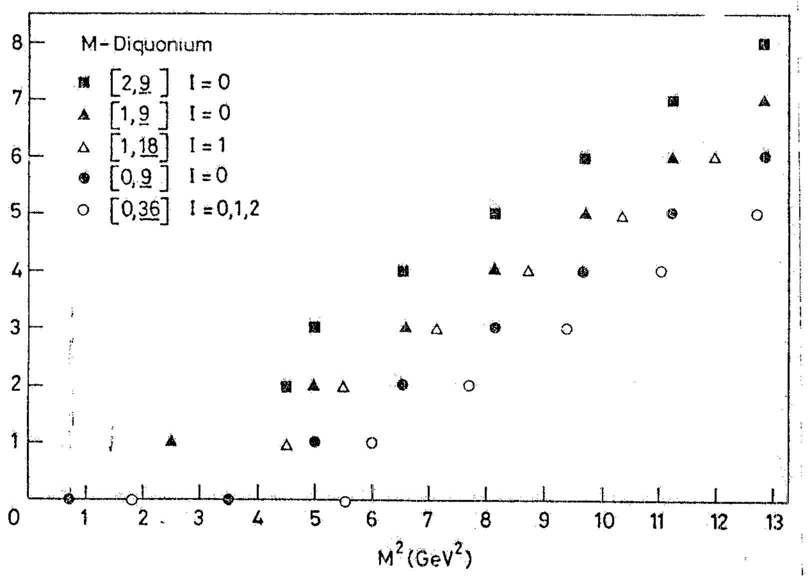

FIG. 46 - Predicted spectrum for M-diquonium.

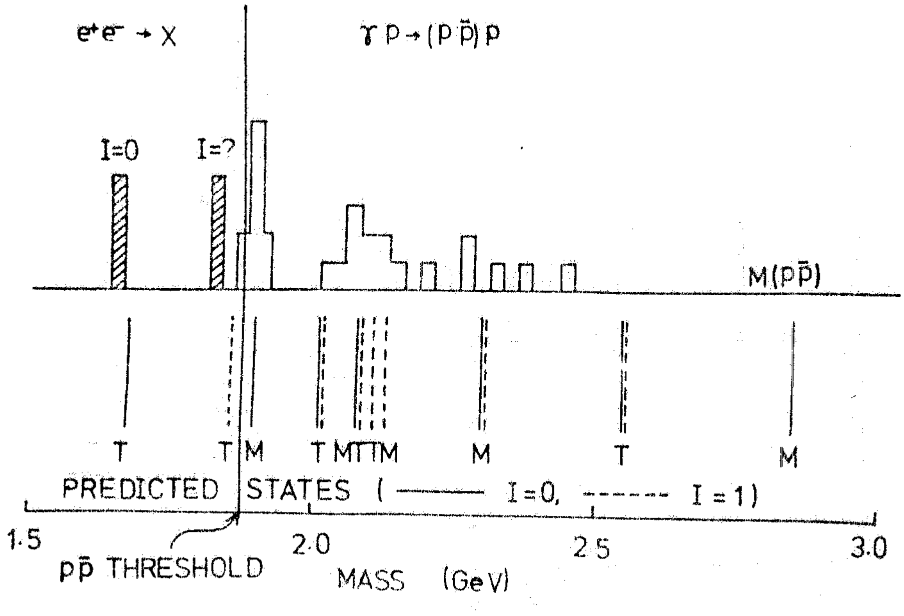

FIG. 47 - Predicted $J^{PC} = 1^{--}$ barionium states.

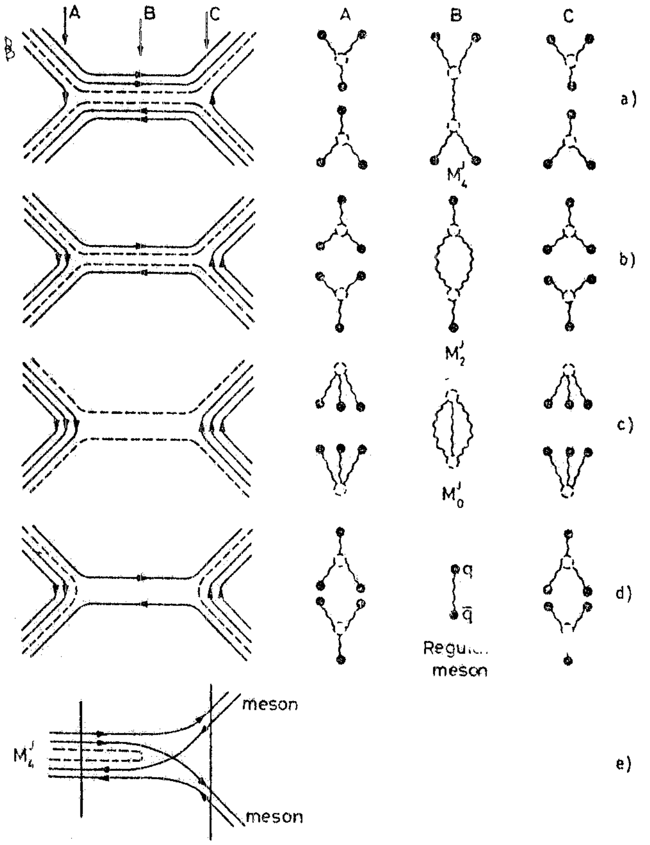

FIG. 48 - BB dual diagrams for BB scattering according to ref. (8).

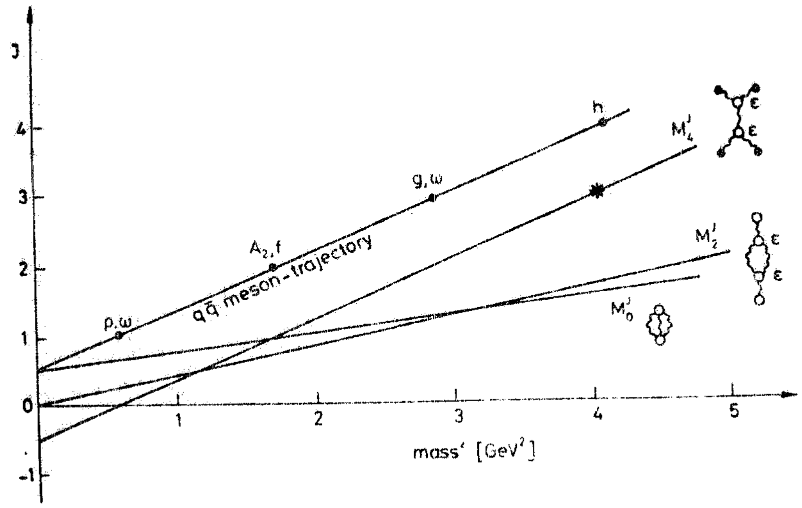

FIG. 49 - Regge trajectories for the exotic mesons of Fig. 48 (the star is the S-meson).

CHAPTER V - THE ALA DESIGN.

The basic design of ALA has been published by the Adone machine group in ref. 44. Work on the detailed design is still in progress. We shall describe here only those machine parameters which are of more direct interest for the experimental group. The machine layout is shown schematically in fig. 50. The length of the two straigth sections available for the experiments is 3. 0 meters. The polar angle covered by the quadrupoles, as seen from the intersect is about ±14°.

The magnetic radius is $\varrho = 2.5$ m, which gives a maximum energy of 1. 2 GeV with B = 16 KG. The design luminosity of the machine is shown in fig. 51. It is seen that the design ALA luminosity is much higher than at Adone and at the present DCI.

The natural dependence on energy of the luminosity of a machine like ALA can be easily estimated on the basis of some general considerations. Let N_1, N_2 be the number of particles in the electron and positron bunches, and assume for simplicity that the density of particles is distributed uniformly in cilindrical bunches of section S. The event rate for a cross-section σ is given by $R = \sigma N_1 \cdot \frac{c}{2\pi r} \cdot \frac{N_2}{S}$ where c is speed of light, r is the machine radius, and $\frac{c}{2\pi r} = f$ is the frequency of the bunch-bunch crossing. Of course with h bunches in each beam, the luminosity is written $L = N_1 \cdot f \cdot \frac{N_2}{S} \cdot h$. When turning around in the machine, the particles emit syncrotron light, and the power lost by one particle is given by the formula

$$U\,(\text{KeV}) = f \cdot 88\ \frac{E^4\,(\text{GeV})}{\varrho\,(\text{m})}$$

This power is restored by the radiofrequency such that the particles, in average, remain on the ideal orbit. However, fluctuations in the emission acts cannot be compensated by the radiofrequency and produce an increase of the beam section as E^2. Let's assume that we want to store in the beams as many particles is possible. This number is limited in pratics by the beam-beam interaction: the "target beam" is seen by the "projectile beam" as a lens which modifies the Q of the machine. This Q-shift ξ can never exceed the distance from the operating point and the nearby instabilities (a reasonable number for this maximum shift is $\xi = 0.06$). The strenght of this addictional lens is (inverse of the focal lenght) proportional to the partical density ($\frac{N}{S}$) and to the inverse of the projectile momentum ($\frac{1}{p}$): $\xi \sim \frac{N}{S} \cdot \frac{1}{p} \sim \frac{N}{E^3}$. This means that for a given ξ , N cannot grow with energy more than E^3.

Therefore, at most $L \propto \frac{N_1\,N_2}{S} \propto \frac{E^3\,E^3}{E^2} \propto E^4$. This is called the natural-energy dependence of Luminosity. In ALA, as we shall see below, it is planned to vary the machine optics over part of the energy range in order to get $L \propto E$. This is a very important improvement. In Adone, on the other hand, for reasons which are not well understood but probably because of the weak radiation damping associated to the rather large bending radius, $L \propto E^7$ for $W \leq 1600$ MeV. At the highest machine energies, the available radiofrequency power is non sufficienty to accelerate a constant number of particles and the luminosity drops very fast with energy. The total power radiated by the two beams is $W_{rad} = U \cdot (N_1 + N_2)$. When W_{rad} is equal to the radiofrequency power, an increase of energy which produces a fast increase of U like E^4, can only be obtained at the expense of the fast decrease of $N_1 + N_2$, with $W_{rad} = W_{rf} = U \cdot (N_1 + N_2) = \text{constant}$.

Then $N_1 + N_2 \propto E^{-4}$, and so $L \propto \frac{N_1 N_2}{S} \propto \frac{E^{-4}\,E^{-4}}{E^2} \propto E^{-10}$.

In a more realistic treatment the transverse particle density in the beam is approximated to two dimensional gaussian distributions with standard deviations σ_x and σ_y, and equivalent section $S = 4\pi \cdot \sigma_x \cdot \sigma_y$

The luminosity is written as

$$L = N_1 N_2 \frac{c}{2\pi r} \quad \frac{1}{4\pi \cdot \sigma_x \cdot \sigma_y} \quad h$$

It is usefull to express N_1 and N_2 in terms of the beam currents, which are directly measurable. Since $I_{1,2} = e\, N_{1,2} \frac{c}{2\pi r}\, h$ and assuming $I_1 = I_2$, we have:

$$L = \frac{2\pi r}{e^2 c h} \quad \frac{I^2}{4\pi \cdot \sigma_x \cdot \sigma_y} = \left|\frac{I}{I_0}\right|^2 \quad \frac{r c}{2 r_e^2} \quad \frac{1}{\sigma_x \cdot \sigma_y} \quad \frac{1}{h}$$

where $r_e = \frac{e^2}{m_e c^2} = 2,82 \times 10^{-13}$ cm is the classical radius of the electron, and $I_0 = \frac{e c}{r_e} = 17000$ A.

The Q-shifts are in general different in the z and x directions, and one gets

$$\xi_{x,z} = -\frac{1}{4\pi} \quad \frac{\beta_{x,z}}{x,z} \quad \frac{\Delta p_{x,z}}{p}$$

where β is the local betatron wave-length, such that the integral along a full orbit $\oint \frac{ds}{\beta_{x,z}} = Q_{x,z}$

It is convenient to express in the luminosity formula the beam currents as functions of the Q-shifts that they produce by beam-beam interactions (ξ_x, ξ_z). These shifts can be computed as follow (45).

A relativistics bunch of N particles with transverse charge density in the laboratory $\varrho(r) = \varrho_0\, e^{(-r^2/2\sigma^2)}$, with $\varrho_0 = \frac{N e}{2\pi\sigma^2} \frac{1}{L}$ (positive bunch) (L = length of the bunch in the laboratory) generates a transverse magnetic field B_t that can be computed as

$$2\pi r\, B_t = \frac{4\pi}{c} \int_0^r \varrho_0\, e^{-\frac{r^2}{2\sigma^2}} \cdot c \cdot 2\pi r\, dr \quad \text{giving} \quad B_t = -4\pi\,\varrho_0 \frac{\sigma^2}{r} \left(e^{-\frac{r^2}{2\sigma^2}} - 1\right)$$

The longitudinal electric field is depressed by the Lorentz factor γ , and the radial electric field can be derived by a two-dimensional Gauss theorem:

$$2\pi r\, E r = 4\pi \int_0^r \varrho_0\, e^{-\frac{r^2}{2\sigma^2}}\, 2\pi r\, dr$$

giving

$$E_r = -4\pi \cdot \varrho_0 \frac{\sigma^2}{r} \left(e^{-\frac{r^2}{2\sigma^2}} - 1\right)$$

In the beam-beam crossing the charges of the negative bunch are therefore affected by the following force:

$$\vec{f} = -e\left(\vec{E} + \frac{\vec{V}}{c} \wedge \vec{B}\right) = 8\pi e \cdot \varrho_0 \frac{\sigma^2}{r^2} \left(e^{-\frac{r^2}{2\sigma^2}} - 1\right) \vec{r}$$

where use has been made of the above formulae for B_t and E_r. For small displacements

$$\vec{f} \sim -4\pi \cdot e \cdot \varrho_0\, \vec{r}, \text{ viz.} \quad f_x = -4\pi \cdot e \cdot \varrho_0 \cdot x, \quad f_z = -4\pi \cdot e \cdot \varrho_0 \cdot z$$

We see therefore that the perturbation is equivalent to a focalizing effect. This is measured by the relative momentum deviation

$$\frac{\Delta p_{x,z}}{p} = \frac{f_{x,z} \cdot \Delta t}{p},$$

Δt being the duration of beam-beam overlap in the laboratory, $\Delta t = \frac{L/2}{c}$

We thus have

$$f_{x,z} = -4\pi \cdot e \cdot \varrho_0 \cdot (x, z) = -4\pi \; e \; \frac{Ne}{2\pi \; \sigma^2} \; \frac{(x, z)}{L}$$

$$\frac{\Delta p \, x, z}{p} = \frac{1}{p} \, f_{x,z} \cdot \Delta t = -\frac{1}{m \, c \, \gamma} \; \frac{2 \, Ne^2}{\sigma^2 \; L} \; \frac{L}{2c} \cdot (x, z) = -\frac{N \, re}{\gamma \; \sigma^2} \cdot (x, z)$$

We can now re-write $\xi_{x,z}$ as follows

$$\xi_{x,z} = \frac{1}{4\pi} \, \frac{\beta x, z}{(x, z)} \, \frac{N \, re}{\gamma \, \sigma^2} \, (x, z) = N \, \frac{r_e \, \beta x, z}{4\pi\sigma^2 \gamma}$$

If the beam has (more realistically) an elliptical section, one gets

$$\xi_{x,z} = N \frac{r_e}{2\pi \gamma (\sigma_x + \sigma_z)} \; \frac{\beta_{x,z}}{\sigma_{x,z}}$$

Now N can be related to the beam currents, $I = h \, \frac{N_{ec}}{2\pi R}$ and

$$\xi_{x,z} = \frac{I}{I_o} \, \frac{R}{h} \, \frac{mc^2}{E} \, \frac{\beta_{x,z}}{\sigma_{x,z} (\sigma_x + \sigma_z)}$$

The luminosity formula becomes, in terms of $\xi_{x,z}$:

$$L = \frac{c \, h \, E^2}{2R \, r_e^2 (mc^2)^2} \; \frac{\xi_x \, \xi_z}{\beta_x \, \beta_z} \, (\sigma_x + \sigma_z)^2$$

The radial displacement of an electron of energy E with respect to the ideal orbit is usually expressed by the dispersion ψ defined as

$$x = \psi \, \frac{E - E_o}{E_o}$$

The syncrotron radiation generates energy fluctuations whose standard deviation is usually expressed in terms of an adimensional parameter σ_p defined as

$$\sigma_p^2 = \frac{\langle (E - E_o)^2 \rangle}{E_o^2} = 3.84 \times 10^{-13} \; \frac{E^2}{(mc^2)^2} \; \frac{1}{2\varrho} \qquad (\; \varrho \text{ in meters})$$

The horizontal beam dimensions - as well as the vertical ones, coupled to them by a mixing factor ε - are determined by these fluctuations. One can show that the following relation holds

$$\sigma_x = \sigma_p \sqrt{\frac{1}{1 + \varepsilon^2} \, 2M \, \beta_x + \psi^2} \qquad\qquad \sigma_z = \sigma_p \sqrt{\frac{\varepsilon^2}{1 + \varepsilon^2} \; 2M \, \beta_z}$$

where M is a function with the dimensions of a length which is uniquely defined by the properties of the orbits over the section of the bending magnets. The following identity holds

$$\frac{\sigma_x^2}{\beta_x} + \frac{\sigma_z^2}{\beta_z} = \sigma_p^2 \, (\frac{\psi^2}{\beta_x} + 2M) = 2 \, \sigma_p^2 \, M^*$$

This formula shows that M^* (dimension of a length) gives a weighted measure of the beam linear size at the intersection. By isolating a $2 \, M^* \; \sigma_p^2$ factor the luminosity formula can now be re-written as

$$L = \frac{c \, h \, E^2}{2R r_e^2 (mc^2)^2} \; \frac{\xi_x \, \xi_z}{\beta z} \; \frac{(\sigma_x + \sigma_z)^2}{\sigma_x^2 + \frac{\beta x}{\beta z} \; \sigma_z^2} \; 2M^* \, \sigma_p^2$$

and setting
$$\eta = \frac{\xi_x}{\xi_z} = \frac{\sigma_z}{\sigma_x}\,\frac{\beta_x}{\beta_z}\ , \qquad L = \frac{c\,h\,E^2}{2Rr_e^2(mc^2)^2}\,\frac{\xi_x\xi_z}{\beta_z}\,\frac{\left(1+\eta\frac{\beta_z}{\beta_x}\right)^2}{1+\eta^2\frac{\beta_z}{\beta_x}}\,2M^*\sigma_p^2$$

The maximum value of ξ_x, ξ_z is obtained for $\xi_x = \xi_z = \xi_M$ (and $\eta = 1$), and therefore the maximum luminosity (as far as the acceptable tune-shifts are concerned) is by making use of the explicit expression for σ_p^2 :

$$\boxed{L = K_L \frac{E^4}{R\varrho} hM^* \xi_m^2 \left(\frac{1}{\beta_x} + \frac{1}{\beta_z}\right)}$$

with $K_L = c/(2r_e^2(mc^2)^4) \times (3.84 \times 10^{-11}\,\mathrm{cm}) = 1.06 \times 10^{38}\,\mathrm{GeV}^{-4}\mathrm{S}^{-1}$, and $\beta_{x,z}$ are the betatron wave lengths at the crossing point. Along similar lines one can derive the energy dependence of the maximum beam intensity. Since

$$N = \frac{2\pi E}{mc^2 r_e}\,\xi_x\,\sigma_x\,\frac{\sigma_x+\sigma_z}{\beta_x}$$
, one can write identically (isolating a $2\,M^* \cdot \sigma_p^2$ factor)

$$N = \frac{2\pi E}{mc^2 r_e}\,\xi_x\,\sigma_x\,\frac{\sigma_x+\sigma_z}{\beta_x}\,\frac{2M^*\sigma_p^2}{\frac{\sigma_x^2}{\beta_x}+\frac{\sigma_z^2}{\beta_z}} = \frac{2\pi E}{mc^2 r_e}\,\xi_x\,\frac{1+\sigma_z/\sigma_x}{1+\frac{\beta_x}{\beta_z}\left(\frac{\sigma_z}{\sigma_x}\right)^2}\,2M^*\sigma_p^2$$

which gives at most ($\eta = 1$, $\xi_x = \xi_z = \xi_M$) :

$$\boxed{N = K_N \frac{E^3}{\varrho} M^* \xi_M}, \quad \text{when} \quad K_N = \frac{2\pi}{(mc^2)^3}\,\frac{3.84\times10^{-11}}{r_e\,(\mathrm{cm})} = 6.41\times10^{12}\,\mathrm{GeV}^{-3}\,.$$

The specific luminosity L/N is therefore
$$L/N = (K_L/K_N)(\xi_M/R)\,E\left(\frac{1}{\beta_x}+\frac{1}{\beta_z}\right)$$
The number of particles in a beam is limited in practice by injection problems and also by the need of limiting the single beam longitudinal instability. In ALA a rather safe of 150 mA was assumed as maximum current.

For a given current, the luminosity can only be increased by a suitable choice of machine parameters. It is seen in the previous formula that R and $\beta_{x,z}$ should be made as small as possible. Since the space needed in ALA along the ring to locate the various machine components $\gtrsim 70$ m, the adopted value for R is R = 11.14 m. On the other hand, β_x and β_z can be varied by varing the machine optics.

However, a lower limit to β_z is set by the bunch length for optical reasons, and therefore at ALA $\beta_z = 0.2$ m. It is also convenient to have $\beta_x > \beta_z$. At ALA $\beta_x = 1$ m. With the adapted numbers $\xi_M = 0.06$, $\beta_z = 0.2$ m, $\beta_x = 1$ m, R = 11.14 m, $N^+ = N^- = 2.2 \times 10^{11}$ (150 mA).

One gets
$L/N = 6.4 \times 10^{19}\,\mathrm{cm}^{-2}\mathrm{s}^{-1}\,\mathrm{particle}^{-1}$ and $L = 1.4\times10^{31}\,\mathrm{cm}^{-2}\mathrm{s}^{-1}$ at W = 3.4 GeV

The optical parameter M^* (0.82 m given by the formulas above, with $\varrho = 2.5$ m) can be made energy-dependent, in order to have a higher luminosity below W = 2.4 GeV.

Assuming a law like
$$M^* = M^*_{E_{MAX}}\,(E/E_{MAX})^{-m}$$
one has
$L = L_{Emax}\,(E/Emax)^{4-m}$ and $N = N_{Emax}\,(E/Emax)^{3-m}$.

Which means that if m = 3, N = constant and $L = L_{Emax} \cdot E/Emax$.

Indeed the ALA optics allows to make m = 3 from W = 1.6 to W = 2.4 GeV, which corresponds to increase M^* from 0.82 m to 3 m. Below W = 1.6 the luminosity follows the natural law E^4 and the beam current follows the law E^3.

An important parameter in the search for narrows resonancies is the energy speed of the e^+e^- interactions. With the adopted optics the c. m. energy distribution is expected to be roughly gaussian, with Γ_W (MeV) $\approx$ 0.45 W^2 (GeV^2).

The transverse dimensions of the source are negligible ($<<$ 1 mm^2), but its lenght is much larger. This is due to both the natural length of the radiofrequency bunches and to an anomalous lengthening which takes place at the bunch-bunch crossing. Using the 52.5 MHz new Adone radiofrequency the natural source length is expected to vary between $\sim$ 8 and $\sim$ 20 cm f. w. h. m. (see fig. 52). However, a 102.8 MHz RF will probably be adopted for ALA. In this case, it will be possible to operate with a fixed source length of $\sim$ 6 cm (r. m. s.) at all energies (this will be obtained by increasing the RF voltage and power up to $\sim$ 400 KV and $\sim$ 50 KW at the top ALA energy)(fig. 53)

A model wich fits well the data on anomalous source lengthening in the existing e^+e^- storage rings (46) predicts that this effect should be negligible for ALA (47). The use of a 102.5 MHz frequency should also allow to achieve an increase in luminosity of a factor of 1.4, as shown in fig. 54.

The beam lifetime with the expected average residual gas pressure of $\sim 10^{-9}$ torr is of the order of 10 hours. The injection in ALA has to be accomplished by means of two fast kickers along the ring that bend the incoming bunches toward the central orbit, followed by two magnets that set the bunches on an orbit inside the acceptance. The optics is designed such that these operations are possible without perturbing the stacked beams. On the other hand, the losses on the injected bunches as well as their intensity depend on the pre-accelerator that is used as an

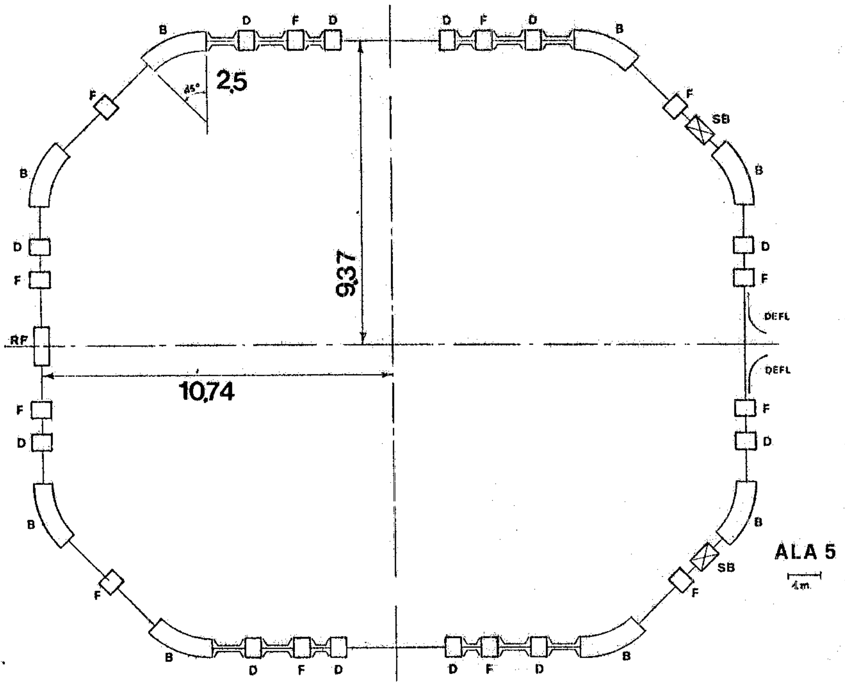

FIG. 50 - ALA layout.

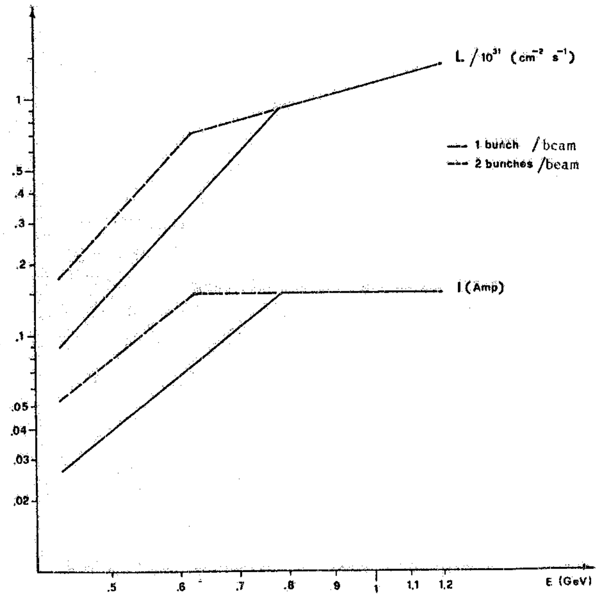

FIG. 51 - Luminosity and total current as a function of energy.

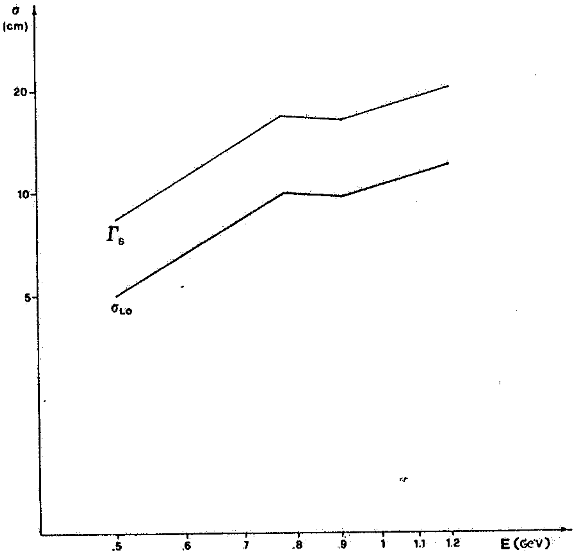

FIG. 52 - Natural r. m. s. bunch length (250 KV) σL_O and source distribution Γ_S (FWHM).

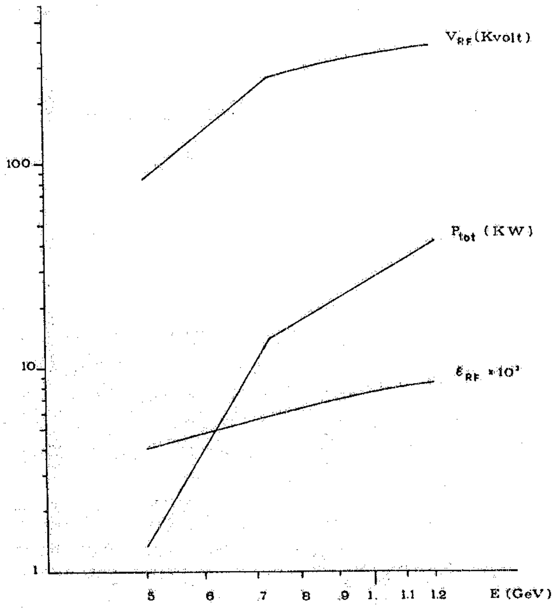

FIG. 53 - RF voltage, total power and energy acceptance.

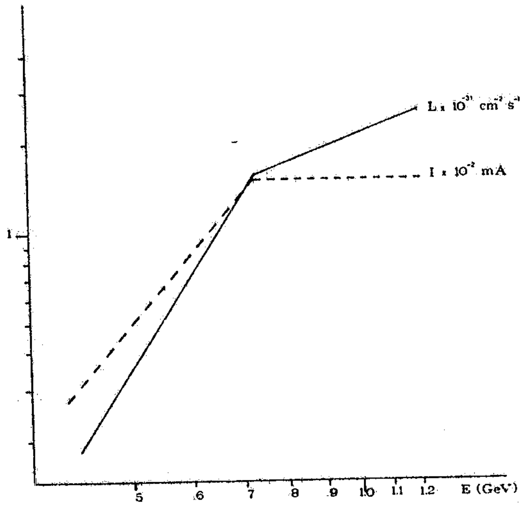

FIG. 54 - Luminosity per crossing and current per beam.

CHAPTER VI - THE MAGNETIC DETECTOR FOR ALA (MDA).

In this chapter the design and test work made by the physicists of the MDA Group is summarized. The author list is the following: M. Ambrosio, R. Baldini-Celio, G. Barbarino, S. Bartolucci, G. Battistoni, R. Bertani, S. Bertolucci, C. Cerri, F. Cervelli, R. Del Fabbro, G. Giannini, P. Giromini, E. Iarocci, P. Laurelli, M. M. Massai, G. P. Murtas, G. Paternoster, S. Patricelli, P. Patteri, G. B. Piano Mortari, A. Sermoneta, F. Sergiampietri, M. Spadoni, L. Trasatti, U. Troya. In the various sections mention will be made of the people who have been directly involved in the specific work. This applies in particular to the author of the present Thesis (see VI, 2).

The main parts of the detector, which is shown skematically in fig. 55, are:

a) a solenoid magnet, whith field parallel to the beam, whose coil is centered around the machine pipe
b) a charged particle detector with cylindrical symmetry inside the coil, which comprises an innerhodoscope of thin scintillation counters to start the time-of-flight measurement and a multilayer cylindrical drift chamber to measure the curvature of the tracks down to polar angles of $\sim 28^c$
c) a barrel hodoscope of scintillation counters, just outside the coil, to stop the TOF measurement
d) a photon detector behind this hodoscope contained inside the cylindrical magnet return yoke, that covers polar angles $\vartheta \gtrsim 36^c$ and extends over the full azimuth
e) a hadron detector sandwiching the magnet yoke, over the full azimuth.
f) a muon filter behind the hadron detector arranged in two vertical telescopes on both sides of the detector
g) small angle monitor counters and tagging counter of inelastic electrons.

We shall in the following describe in detail the feature of the various parts, including the results of tests performed before the end of 1978.

VI. 1 - THE MAGNET. (Designed by T. Taylor, CERN).

Since the free straight section of ALA is 3 m long, the magnet gap cannot be large than $\sim$ 2 m, in order to leave space for the compensators. A schematic drawing of a section of a quarter of the magnet is shown in fig. 56. The relevant dimensions are shown in the figure. The solid angle that the pole profiles (at $\sim 36^o$) leave free for the photon detector is 80%. The solid angle for p_{ch} measurement (90%) will be discussed later. The total weight is $\sim$ 60t. It should be noticed that the cylindrical return yoke (6 cm thick) is commercially available from the container industry.

The computed field map is shown in fig. 57. At the nominal field intensity (3, 82 KGauss) the field non-homogeneity is expected to be at most $\lesssim$ 5% on the coil edges. At the maximum momentum of the ALA secondaries (1.2 GeV/c) the radius of curvature is $\sim$10.5 m. For particles at 90^o, the bending over 70 cm path length generates a displacement of $\sim$ 2.3 cm, which is quite adeguate to allow an accurate momentum measurement by the inner drift chambers (see later).

A drawing of the section of the coil is shown in fig. 58 and the main coil parameters are collected in Table III.

The aluminium coil will have to be wound onto the inner cylindrical support under 200 Kg tension to allow coil stability when it heats up during operation. The coil will then be impegnated under vacuum with resin. The bore support tube will be supported from the inside until the assembly is properly polimerized. The special effort made to design a thin coil (3.1 cm Al equivalent, everything included), has implied a number of special feature (e. g. 45 independent water-cooling systems).

TABLE III

Coils

Al, total section	$18 \times 20\ \mathrm{mm}^2$
resistivity	$0,0278\ \Omega/\mathrm{mm}$
hole diameter	$\phi = 10$ mm
distance between wires	2 mm
length of solenoid	180 cm
number of turns	96
coil radius	80 cm
total coil length	452 m

weight	350 Kg	coil
	400 Kg	support
	150 Kg	resin
	900 Kg	total

Field

$$B = \frac{4\pi}{c}\ I\ n = 0.0126\ I(\mathrm{Ampere})\, n(\mathrm{coils/m})$$

magnetic field = 3.82 KGauss

Current	6375 A
power consumption	1.86 MW

45 water circuits, Δt (out - in) $\sim 20^\circ$, pressure $5\ \mathrm{Kg/cm}^2$

The problem of ensuring an easy access to the inner detectors is not an easy one and is still under study (by G. Gennaro and the Mechanical Design Team in Pisa). A tentative solution is indicated in fig. 59. The return -yoke and photon detector would first be rolled sideways together; next, the drift chambers and the outer TOF scintillators would be slided longitudinally to free one magnet pole, which can also roll sideways. This gives access to the coil that is conceived as a telescope such that one half of it slides lingitudinally inside the second half, and to the central chambers that can be opened sideways in two blocks. This system would allow the assemble and disassemble the detector without removing the machine pipe. This condition, however, gives complications in particular in the coil mechanics.

VI. 2. - The central chambers.

VI. 2. 1. - General design of the detector.

Central track measuring devices for storage rings based on sets of longitudinal drift cells have been emploied in a number of modern magnetic detectors (e. g. MARK II at SLAC, R 106 and R 807 at the ISR, CELLO at PETRA). These chambers combine excellent space resolution transverse to the wires - which is most important in a longitudinal field - with easiness of operation in a magnetic field (48). The factors determining the space resolution are basically three, as illustrated in fig. 60. The fluctuations of the electronics in the drift time measurement contribute a constant term of about $40\,\mu$. Next, when the particle crosses the chamber at very small distancies from the wire the cascade generating the drift pulse is cut-down with increasing statistical fluctuation of the collected charge. The dominant term at large distancies is contributed by the diffusion of the electrons during the drift and is proportional to the square root of the distance from the wire. The overall resolution over distancies of a few centimeters can be as good as 0,1 mm. As discussed in ref.(48), these features are not appreciably changed when the chamber operates in a longitudinal magnetic field. The drift velocity w is modified according to the formula

$$w_n = w \Big/ \sqrt{1 + 4\left(\frac{B}{E}\right)^2 \left(\frac{w}{c}\right)^2}$$

and therefore is still a constant. For $B \sim 4$ KGauss and $E \sim 3000$ V/cm (E should be kept constant over the full chamber volume), the change in drift velocity is about 0.3%.

Since the sagitta of the charged secondaries at the low energies that are typical at ALA can be easily made much larger than the precision of position measurement in the chambers, the relative error $\frac{\Delta p}{p}$ is dominated by multiple scattering (as will be discussed in more detail below). Thus one should build the chamber using as little material as possible. This is achieved in our design by reading the longitudinal coordinate along the wire with the method of charge division which provides for each hit a space-point (except for the left-right ambiguity) using information collected by the sense-wire only. The full useful volume is thus filled with drift cells according to the schema shown in fig. 61. The main mechanical parameters are quoted in Table IV.

TABLE IV - Main parameters of central chambers.

inner radius	12 cm
outer radius	72 cm
number of layers	11
length	160 cm
minimum drift space (inner layer)	0,4 cm
maximum drift space (outer layer)	2,4 cm
number of sense wires in one layer	96
angular opening of one cell	3.75°
total number of sense wires	∼ 1000
total number of field wires	∼ 2000

Sense wires:

30 ∅, Ni/Cr, tension 60 gr, resistivity 3000 Ω/m

Field wires:
100 ∅, Cu/Be, tension 120 gr.

total mechanical pressure on end caps ∼ 300 Kg

gas mixture: Argon 60% Ethane 40%

Across the chamber, ϑ_{scatt} generated by the gas is tipically ($p = 300$ MeV/c) about ∼ 4 mrad (r.m.s.). This is also the typical scattering angle when a 300 MeV/c particle crosses a wire, which happens with probability 1%.

The lines of force and the curves of equal delay from the sense wires are shown for $B = 0$ and $B = 4$ KGauss in fig. 62 and 63 (computed by S. Bertolucci and P. Giromini). On the basis of these computations an essentially constant drift velocity is expected. Direct measurements on a similar prototype have given excellent results, as will be shown later.

In the charge-division method (CDM) the sense wire is made of high resistivity material (∼ 3000 Ω/m) and the charges transported to the wire ends are measured. Qualitatively, these charges are inversely proportional to the distance from the point of impact of the avalanche to the wire. The maximum precision that can be obtained with this method is set by the equivalent noise charge (ENC) which is present at the wire ends. At normal temperature this limit is approximately $\frac{\Delta L}{L} \sim \pm 0,2\%$, viz $\sim \pm 3$ mm in our case (see later). This is as good as what one can achieve with the small angle stereo, which however would require three times more wires and would not give enough space points inside the available magnetic volume. An accurate test of the charge division technique has shown, as discussed below, that this limit can be very well approached in practice.

VI. 2. 2. - Estimated momentum resolution.

The expected momentum resolution has been computed in a number of ways. First one has checked with finite approximate formulas that the result was of the desired order of magnitude. The result of such a computation (due to P. Giromini) is shown in fig. 64. To be conservative, an error of $\pm$ 0.4 mm on the transverse coordinate y and of $\pm$ 16 mm on the longitudinal coordinate z was assumed. At a typical momentum of 500 MeV/c, the error $\frac{\Delta p}{p}$ generated by the φ resolution alone is shown in the left graph of fig. 64, as a function of the polar angle ϑ . When decreasing ϑ from 90° to smaller angles at a fixed total momentum, the bending radius grows because of the reduced $p_\perp$ and the resolution improves. However, at $\vartheta \sim 45^\circ$ the particle begins to miss the outer chamber planes (see upper graph in fig. 64) and $\frac{\Delta p}{p}$ jumps-up in steps. The error contributed by the z-measurement is shown in the central graph, again for p = 500 MeV/c. Assuming to derive p from the measurement of z at an exactly known radial distance d, one has $p = \frac{p_{/\!/}}{\cos\vartheta}$, with $\cos\vartheta = \frac{z}{\sqrt{z^2+d^2}}$ and $\frac{\Delta p_{/\!/}}{p_{/\!/}} = \frac{\Delta z}{z}$.

This gives $\frac{\Delta p}{p} = \cos^2\vartheta \frac{\Delta z}{z}$, giving an increasing error when ϑ is decreased from 90°, as seen in the figure. The contribution by multiple scattering, which is momentum independent since both the bending angle and the scattering angle are $\propto \frac{1}{p}$, is shown in the right graph of the figure. The increasing error in steps at $\vartheta \sim 45^\circ$ is due to the decreasing path in the magnetic field. The overall resolution is therefore expected to be $\sim$ $\pm$ 4% at this momentum, for $\vartheta \gtrsim 45$. One sees in fig. 64 that at $\vartheta \sim 28^\circ$ the error grows violently. One can estimate from here that the useful solid angle for momentum measurement will be $\sim$ 90%. In practice, the overall error will of course depend on momentum, because the contribution by the first two terms is $\frac{\Delta p}{p} \sim p$.

VI. 2. 3. - Montecarlo computed momentum resolution.

In order to get a better estimate of the actual errors, a Montecarlo generation of the points to be measured and a best-fit reconstruction of the tracks in the chambers has been made by R. Del Fabbro. In this computation, the contribution of the wire material was neglected and the gas was supposed to be concentrated in eleven equally-spaced cylindrical layers.

With reference to the frame shown in fig. 65, the trajectory of a particle emitted at $(0, 0, z_0)$ with polar angle ϑ will be an helix, with longitudinal and transverse velocities

$$\beta_{/\!/} = P_{/\!/}/E \ , \qquad \beta_\perp = P_\perp/E$$

The radius of curvature and the angular velocity of the rotation are

$$P = P_\perp c/eB \ , \qquad = \frac{eB}{m_o c\gamma} = \frac{\beta_\perp c}{\varrho}$$

(c = speed of flight) (B = magnetic field)

$(\varrho = 3.3 \frac{P_\perp}{B} \text{ cm}(\text{Mev}/c)^{-1}\text{KGauss})$

The equations of motion are

$$x = R\left[-\cos(\omega t + \phi) + \cos\phi\right], \qquad y = R\left[\sin(\omega t + \phi) - \sin\phi\right]$$

$$z = z_o + \beta_{/\!/}\, ct \ .$$

The equation of the x, y trajectory is

$$(x - R\cos\varphi)^2 + (y + R\sin\varphi)^2 = R^2$$

viz. a circumpherence of radius R and centre at

$$x_c = R\cos\varphi \qquad y_c = -R\sin\varphi$$

In terms of x_c, y_c which are the effective unknwns, the equation is

$$x^2 + y^2 - 2\,x\,x_c - 2\,y\,y_c = 0$$

The x, y coordinates are measured up to 11 times in the intersections of the trajectory with the chamber sensitive planes. This gives the information by which x_c, y_c are deduced with a best-fit procedure. $R \sim \frac{1}{p_\perp}$ is in turn derived as $R = \sqrt{x_c^2 + y_c^2}$.

The assumed measurement errors were again $\sigma z = \pm 16$ mm, while $\sigma_x = \sigma_y$ where derived from the error on the drift distance, $\sigma_{drift} = \pm$ (0.4 + $\delta \bullet$ 0,0444 mm). The dip angle δ is the angle between the radius and $p_\perp$ at the impact points. The weight by which the error is increased when $\delta \neq 0$ is derived from other experiments. From fig. 65 one sees that the radius of the i^{th}-layer is $\varrho_i = 2 R \sin \frac{\omega t_i}{2}$ which gives $t_i = \frac{2}{\omega} \sin^{-1} \left(\frac{\varrho_i}{2R} \right)$

This allows to remove the time from the z-equation of motion

$$z_i = z_o + \beta_{//} c \frac{2}{\omega} \sin^{-1} (\varrho_i/2R) = z_o + 2R \frac{\beta_{//}}{\beta_\perp} \sin(\varrho_i/2R)$$

In this equation, R is known (from the best-fit to the x, y measurements), z_i are measured a number of times and the unknowns z_0 and $\beta_{//}/\beta_\perp$ can be derived in a best-fit analysis. Thus the production parameters can be fully reconstructed:

$$\phi = \tan^{-1}(-y_c/x_c) \ , \quad \theta = \tan^{-1}(\beta_\perp/\beta_{//}) \ , \quad p_\perp(\mathrm{MeV/c}) = (B(\mathrm{Kgauss})/3.3)\,R(\mathrm{cm}),$$

$$p_{//} = \frac{\beta_{//}}{\beta_\perp} p_\perp \ , \qquad p = p_\perp \sqrt{1 + (\beta_{//}/\beta_\perp)^2}$$

In our Montecarlo computation pions are generated at various polar angles and at $\varphi = 0, z_0 = 0$ for a number of significant momenta. The trajectories are followed inside the field and the impact points on the chambers are recorded. Next, these coordinates are read out with the previously mentioned experimental resolutions and the best helix is fitted through the data, ending with the reconstruction of z_0, φ, ϑ, $p_\perp$, $p_{//}$, p. The distribution of the reconstructed parameters is finally compaired with the input values to give the resolution.

The Montecarlo calculation was first run neglecting the effects of multiple scattering. As mentioned before, the momentum resolution $\frac{\Delta p}{p}$ is expected to grow with p. We shall now give a more detailed estimate of this effect. In an arc of angle γ and radius R, the cord c and the arrow f are given by

$$c = 2R \sin \gamma/2 \qquad\qquad f = R(1 - \cos \gamma/2)$$

giving $R = \frac{c^2}{8f}(1 + (\frac{2f}{c})^2)$. In our case $R \sim \frac{c^2}{8f}$ $\quad (\frac{f}{c} << 1)$

Therefore $\frac{\Delta p}{p} = \frac{\Delta R}{R} = \frac{\Delta f}{f}$

and $\frac{\Delta p}{p} = \Delta f \frac{8R}{c^2} = \frac{\Delta f(\mathrm{cm})}{c^2(\mathrm{cm}^2)} 8 \cdot 3.3 \frac{p_\perp(\mathrm{MeV/c})}{B\ (\mathrm{KGauss})}$

we write $\frac{\Delta p_\perp}{p_\perp} = K p_\perp(\mathrm{MeV/c})$ $\qquad$ where $K = 26.4 \frac{\Delta f\ (\mathrm{cm})}{c^2(\mathrm{cm}^2) B\ (\mathrm{KGauss})}$

Montecarlo results on $\frac{\Delta p_\perp}{p_\perp}$ are shown in fig. 66 for $\vartheta = 30°$ and $\vartheta > 50°$ as a function of p. The fitted curves give $K = 1.58 \times 10^{-4} \mathrm{MeV}^{-1}$ and $K = 4,29 \times 10^{-5} \mathrm{MeV}^{-1}$ respectively. In the latter case (c = 70 cm) this corresponds to $\Delta f \sim 0,3$ mm. This is also the order of magnitude of Δf at $\vartheta = 30°$, where c = 35 cm.

The dependence of $\frac{\Delta p_{//}}{p_{//}}$ on $p_{\perp}$ can be estimated as follows.

$$p_{//} = \frac{\beta_{//}}{\beta_{\perp}} p_{\perp} = R_{\beta} p_{\perp} \quad (\text{where } R_{\beta} = \beta_{//}/\beta_{\perp}), \qquad (\frac{\Delta p_{//}}{p_{//}})^2 = (\frac{\Delta R_{\beta}}{R_{\beta}})^2 + (\frac{\Delta p_{\perp}}{p_{\perp}})^2$$

From the previously derived linear expression $z = z(\beta_{//}/\beta_{\perp})$ one gests

$\Delta R_{\beta}/R_{\beta} = \Delta z/z$

At any distance from the axis, $z = \varrho/\mathrm{tg}(\theta)$. Thus in our case $\frac{\Delta R_{\beta}}{R_{\beta}} = \langle\frac{\Delta z}{\varrho}\rangle\, \mathrm{tg}\theta$,

with $\langle\Delta z/\varrho\rangle$ being the effective z-resolution weighted over the distance. At an intermediate angle $\vartheta = 60^{\circ}$ ($\mathrm{tg}\vartheta \sim 1,7$), since the effective $\frac{\Delta z}{\varrho}$ must be $\frac{1,6}{70} \sim 0,023$, one estimates $\Delta R_{\beta}/R_{\beta} \sim 4\%$ while $\Delta p_{\perp}/p_{\perp}$ is $\sim 1\%$.

Thus to a first approximation $\Delta p_{//}/p_{//} \sim \langle\Delta z/\varrho\rangle\, \mathrm{tg}\theta$, independent of p. In our Montecarlo computation, at typical momenta (200-400 MeV/c) one finds at $\vartheta \gtrsim 50^{\circ}$ the results quoted in fig. 66, b. One sees that at $\vartheta = 60^{\circ}$, $\Delta p_{//}/p_{//} \sim 5\%$ which is close to our estimate. As far as the overall momenta resolution is concerned, one easily finds

$$\Delta p/p = \sqrt{K^2 p_{\perp}^2 + 2\sin^2\theta\cos^2\theta\,(\frac{1}{2}\,\frac{\langle\Delta z^2\rangle}{\varrho^2} - K^2 p_{\perp}^2)}$$

and the results of the Montecarlo computation are shown in fig. 66, c. They check very well with the estimate given in the left and central part of fig. 64. The distribution of the reconstructed z_0's is shown in fig. 67.

After having understood the effect of the errors of measurement, multiple scattering was taken into account.

Starting from the intersection, the secondaries cross the pipe (5×10^{-2}cm of steel, $\frac{L}{x_0} = 0,0284$) the TOF counters (5×10^{-1}cm of scintillator, $\frac{L}{x_0} = 0,0116$) the chamber wall ($\sim 10^{-1}$cm of aluminium, ($\frac{L}{x_0} = 0,0112$). This gives

$$\vartheta_{ms} \sim \frac{3.17}{p\,(\mathrm{MeV/c})} \quad (\text{walls})$$

at the entrance of the useful volume. The gas mixture is assumed to be 60% Ar ($x_0 = 1,1\times10^{+4}$cm) and 40% C_2H_6($x_0 = 3,3\times10^{+4}$cm). Therefore for a radial crossing of the chamber (60 cm path-length) one has

$$\langle\theta_{ms}\rangle \simeq \frac{0,88}{p\,(\mathrm{MeV/c})} \qquad (\text{gas})$$

In the computation, the gas was assumed to be concentrated in 11 cylindrical surphaces at the sense-wire distancies. The effect of the wires themselves was neglected. Because of the large scattering in the walls, the fit was made to a circumpherence in the azimuthal projection after rilaxing the condition of passage through the beam axis by generating the tracks at the chamber entrance. The results of the computation are shown in fig. 68. It is noticed a large loss of resolution on $p_{\perp}$ with respect to the case of zero multiple scattering (full line in fig. 68, a) and a smaller increase of $\Delta p_{//}/p_{//}$ (fig. 68, b). Alltogether one predicts a rather ϑ-independent $\frac{\Delta p}{p}$. The overall resolution is shown in fig. 69, as a function of p. The parameters of the fitted straight line $\frac{\Delta p}{p} = a\,p + b$ are

$a = 7,5\times10^{-3}\,\mathrm{MeV/c}^{-1}$, $\qquad b = 1,6$

In conclusion, the results of the Montecarlo calculation have confirmed, with many more important details, the estimates of fig. 64.

VI. 2. 4. - Tests of the charge-division method.

In order to understand the practical problems of operating a central drift-chamber detector with charge-division read-out, I have joined for three months in the group of experiment R 807 (49) at the CERN ISR and helped in setting up and running a prototype chamber. The results of that work are described in detail below.. I express my deepest appreciations and thanks to the colleagues of that group, in particular to the Group Leader C.Fabjan and to A. Redge, E. Rosso, R. Hogue, T. Ludlam.

The drift chamber which we used in the test was a sector of a cylindrical detector comprising three azimuthal cells. Each cell had a 4 ° opening angle, an inner radius of 204 mm and an outer radius of 328 mm (fig. 70). The drift space varied from 7 mm to 11 mm. Each cell had 16 sense wires, staggered by 0, 4 mm to solve the left-right ambiguity. The radial distance between a sense wire and the nearest potential wire was 4 mm. Notice that in MDA we hope to eliminate the potential wires between one sense wire and another along the radious, since the computed field (fig. 62, 63) is still good enough. The first and the last wires of each cell where the electric field has greater non-homogenity were not used.

The sense wires (Ni/Cro, 25 μ in diameter) were 1411 mm long, with a resistance of 3800 Ω . For a comparison, there were also 7 wires 30 μ in diameter with a resistance of 2500 Ω . Potential wires were Cu/Be, 100 μ in diameter. The gas was a mixture of Argon (60%) and Ethane (40%). The mechanical tension was 40 gr for the sense wires and 120 gr for the potential wires.

The supply scheme to the field wires is shown in fig. 71. Notice the bypass capacitors C_{bypass}, which are used to keep the voltage stable by removing the positive charges which are deposited on the electrodes during the chamber operation. The power supply (HV) was set at -5380 V, which gives -3300 V at one extreme (V_1) of a cell. In order to compensate for the variable cell width and to keep the drift velocity constant, the voltage difference between a field wire and the adjacent one is close to 20 V, giving about -2500 V in V_2. The sense wires are grounded. The voltage of the field wires interlieved to the sense wires is V_P. V_P could be varied between -1400 and -1650 V.

The scheme of the read out electronics is shown in fig. 72. The preamplifier is connected directly at the wire end. The output signal runs through 3 mt. of cable to reach the time pick-off (TPO). Three 60 m long cables carry the time information and the two analog information on charges A and B from the TPO to the TDC and to shaping amplifiers.

The preamplifier (49) (fig. 73) is a low noise, low input impendence (75 Ω) circuit, amplifying current to voltage with a gain of 30 mV at the open output for 1 mA of input. The parasitic capacity at the T1 collector determines the rise time at the output. It is of course important that the rise time be fast to give a good knowledge of the drift time. For input signals with rise time of 10 ns the output rise time is 25 ns. The output impendence is 50 Ω . There are two output lines, one positive and one negative, balanced and twisted together to avoid the cable cross talk. z_0 (close 32 KΩ) is chosen for each preamplifier, such as to produce the same gain. There is also a calibration input, with an input impendence of 30 KΩ .

The scheme of the TPO (49) is shown in fig. 74. The TPO is a discriminator with a 3 mV threshold which is triggered by the sum of the signals from the preamplifiers connected at the ends of one wire. The 50 ns long output pulse runs through a 60 m long twisted pair, at the end of which is converted to NIM standard and stops a TDC.

The scheme of the shaping amplifier (49) is shown in fig. 75. Transistors T_4, T_5, T_6, T_7 amplify the input charge. On the T_6 base there is a signal which, after a fast rise, decreases with a time constant of R_{15} C_3 = 4. 7 μs/ This signal arrives to the T_6 emitter and to the T_8 collector, where at zero time it splits into two equal parts (since z_0 is the characteristic impendence of the delay line). After a time equal at the delay time, the current reaches the T_6 collector and then comes back through T_8 into z_0, being twice larger and opposite in polarity. Since the delay line is not matched one has, after twice the delay time, a reflected signal which brings the output back to zero. This signal is eventually amplified, such that the output aplitude is proportional to the charge injected by the wire. The three above circuits have been designed by J. Lindsay and W. J. Willis.

The logic of the electronics used for the calibration of the chain is shown in fig. 76. The clock pulse from the computer stats timing unit 1 whose end-mark after 350 ns opens a 600 ns gate to the chamber ADC. The output pulse of TU1 is shortened to 120 ns to gate ADC 2, where the injected charge into the test input of the chamber is monitored. The computer output also operates a pulse whose output is fed into the test input and can be varied to simulate different injected charges by the wire.

To operate the chamber on the test beam the arrangement of fig. 77 and the circuitry schematized in fig. 78 were emploied. In normal conditions C_2 has two activated inputs and one input waiting for the trigger signal from C_1. A particle crossing the chamber is detected by scintillation counters, S_1 (in front) and S_2, S_3 (behind) and triggers both C_1 and C_2. A prompt output from a timing unit inhibits C_2 while a 10 μs delaied end mark restores the LAM grader. The C_2 signal is suitably shaped to generate a 700 ns gate to the ADC's (reading Q_1, Q_2) and the stop pulses to the TDC's. The data are at this point read-out by the computer (which inhibits the LAM grader). The read-out cycle lasts less than 10 μs. The beam emploied was a 4 GeV/c π^- beam whose width was defined to 2 mm by the trigger counters.

In the calibration with the pulser, the pulse shape at the key points along the chain when the electronics was properly operating was as shown in fig. 79. A typical calibration curve is shown in fig. 80.

Data on test beam was collected with the chamber set at two orthogonal directions on a plane normal to the beam ($\alpha = 0°$ and $\alpha = 90°$ in fig. 77). The ratio $\frac{A}{A+B}$ was recorded (A and B being the digital readings of Q_1 and Q_2) as a function of the longitudinal position of the beam along the wire. A typical result is shown in fig. 81, where one sees that linearity is very good. It is interesting to observe that when the beam is positioned at the end of the wire one finds that Q_1 is still slightly different from zero. This is because the input resistence of the preamplifier (75 Ω) is not negligible, being equivalent to 2. 5 cm of wire (resistivity 30 Ω/cm).

With the correct choice of the bypass capacitors (fig. 71) the spread of the data at a definite beam position was also quite small as seen in fig. 82. It is shown below that this resolution ($\pm$ 6 mm) is not far from the limit due to the thermal noise on the wire.

One can get an estimate of the gas gain in the following way. With a 50 ns, 480 mV input calibration pulse the reading A + B = 1950 was found. Since the input impendence is 30 KΩ , the input charge is $0,8 \times 10^{-12}$ Coulomb. On the other hand, the typical reading on the beam was A + B = 800, i. e. the charge deposited by the beam was $Q_s = 0,33$ pC $1,7 \times 10^6$ electrons. The beam crossed $\sim$ 1 cm of Ar-Ethane gas with a total ionization of $\sim$ 135 electrons. The gas gain is thus about 10^4.

The chamber noise is given by the thermal noise of the resistive anode. The equivalent charge is (50)

$$\overline{ENC}^2 \sim KT \frac{1}{R} \tau$$

with: R = wire resistence, τ = width of the output signal, T = absolute temperature, K = Boltzman constant. Since the output pulse is 300 ns long and R = 3800 Ω , one has $\overline{ENC} \sim 3 \times 10^3$ electrons. The estimate for the ultimate resolution is therefore

$$\Delta L/L = \Delta Q/Q = ENC/Q_s \sim 2 \times 10^{-3}$$

On the other hand, the experimental resolution of $\sim$ 10 mm f. w. h. m. (fig. 82) corresponding to a standard deviation of $\sim$ 4. 2 mm, gives

$$\frac{\Delta L}{L} \sim 3 \times 10^{-3}$$

One thus concludes that one is near to the ultimate limit of the technique. In order to lower the noise, tests were made with delay lines 200 ns long. The results are quoted in Table V. It is seen that the resolution is improved by approwimately 30%. A comparison was also made between the performances of the 25 μ and the 30 μ wires. There are strong electric fields in the chamber and for $\sim$ 140 cm long wire at a tension of 40 g the arrow is close to 100 - 200 μ . This effect was accurately measured as a function of the applied field with the help of a narrow laser beam mounted on a high-precision goniometer. The results are shown in fig. 83. For a 25 μ wire the elastic limit is close to 40 gr, while for a 30 μ wire is 90 gr, such that it is possible to use a tension of 50 - 60 gr. It was found in a test that the working performances of the 30 μ wire are good enough. For example, fig. 84 shows that the resolution (V_p = -1650 V) is still 5×10^{-3} (f. w. h. m.). As a result of these tests, 30 μ thick wires with 60 gr tension will be used in the experiment.

TABLE V - Performances of different delay lines.

	WIRE 1 (300 NG)			WIRE 2 (200 NG)			WIRE 3 (300 NG)			WIRE 4 (200 NG)		
Longitudinal coordinate (cm)	A+B	$\frac{A}{A+B}$	FWHM (mm)	A+B	$\frac{A}{A+B}$	FWHM (mm)	A+B	$\frac{A}{A+B}$	FWHM (mm)	A+B	$\frac{A}{A+B}$	FWHM (mm)
0	800	70	19	900	82	9	1000	72	14	1000	80	12
30	800	281	16	900	294	10	800	291	12	900	288	10
60	800	494	9	900	505	8	1000	508	10	1000	497	8
90	800	715	18	800	713	11	800	712	12	900	705	10
120	900	935	26	900	924	16	1000	935	29	1000	921	16
< FWHM > mm			18			11			15			11

The performances of the chamber under high rates were also testes. The positive ions accumulate near the anode where the electric field is larger and where the avalanche is located: their drift time to the anode is of the order of hundreds of ns. Under high rates this positive charge in the chamber, which gives a space charge effect, can cause troubles. By varying the beam intensity, the total charge A + B was measured and the results are plotted in fig. 85. One can see a clear decrease for high rates. However, the chamber is expected to operate well even for rates as high as at the ISR (up to about 10^5 charge tracks per cell) and therefore no problem is anticipated at ALA, where the rate of beam-beam events is down by $\sim 10^7$ with respect to the ISR. As a matter of fact, the overall radiation density at ALA will be dominated by machine background.

Another factor which can cause the operation of the chamber to deteriorate with time is polimerization of the gas due to radiation. This effect was studied using a small chamber of the same characteristics as the one previously described but with wire length of 30 cm. We have started measurements of the total A + B signal, with the chamber irradiated with a radioactive source (Sr^{90}, 50 m Curie, 10^9 β-desintegration per second) collimated to $\sim$ 2%. The results are shown in fig. 86 and again indicate that the chamber will be able to operate for long times at the ISR. The same conclusion should be valid fo ALA, although the background radiation will be much higher than at the ISR.

The height of the output pulse was studied as a function of the electric field in the cell (for 25 μ wires). The results are shown in fig. 87. The function A + B is an exponential in the field: Ln (A+B) is fitted very well by a A comparison was also made between 25 μ and 30 μ wires. The results is shown in fig. 88 (where the quoted signal is an average between the output of two wires). Although the 25 μ wires are better, quite a sufficient pulse height can be obtained with the 30 μ wires. The spread with wich A + B is measured in the two cases is shown as an example in fig. 89. The resolution is $\sigma \sim \pm$ 50% for 25 μ wires and $\sigma \sim \pm$ 100% for 30 μ wires. Therefore the loss of information in a dE/dx measurement is appreciable if 30 μ wires are adopted.

In order to measure the drift time, the chamber was moved transverse to the beam by accurately measured steps. A typical result (using a 2 mm wide beam) is shown in fig. 90. Notice that at $z \gtrsim 9$ the beam crosses the wire, and the measured time distance (the stop being provided by the trigger) begins to decrease. It was found in all cases that the data can be well fitted by straight lines with slope $\sim$ 15 channel/mm. The time scale that is needed to derive the velocity was obtained bv reducing by 60 ns the delay of the stop signal. An average difference of 35 channels was found in the output. Thus 1 channel = 1. 7 ns, and $v_{drift} \sim 40$ mm μs^{-1}. A direct check of this result was made by noticing that the difference between reading of even and odd-numbered wires in one cell was $\sim$ 12 channels. This must correspond to 0, 8 mm, which is the staggering between the wires, and corresponds to $v_{drift} \sim 40$ mm/μs. The conclusion of the tests made at CERN on the charge division method for chambers similar to the one to be used in MDA can be sintetized as follows. The method can work: it gives $\sigma \sim \pm 5$ mm at the centre and $\sigma \sim \pm 9$ mm at the edge of a 140 cm long wire. The linearity is very good when bypass capacitors are placed on wire ends. A delay line of 200 ns in the shaping apmlifier is better than 300 ns, in particular because it allows to use 30 μ wires with a mechanical tension of 60 gr. However, the dE/dx ability of the method is reduced. The gas gain is close 10^4 with a field of $\sim$ 3 KV/cm. In these conditions the drift speed is close 40 mm/ μs. A staggering by $\pm$ 0. 4 mm looks adeguate to solve the left-right ambiguities. Argon 60%, Ethane 40% is a good mixture. Finally, although some information on the total charge can be derived from the A + B signal, more work would be necessary in order to make it useful for a dE/dx measurement.

VI. 3. - The time of flight system.

The arguments discussed in Chapters I ÷ V show the extreme importance of separating pions, kaons and protons. This can be done in MDA by a combined measurement of p_{ch} and TOF (giving $\frac{1}{\beta}$) or p_{ch} and $\frac{dE}{dx}$ (giving $\frac{1}{\beta^2}$ at ALA energies). The job is increasingly difficult with increasing particle momentum. The order of magnitude of the momenta involved is seen in fig. 91. a, b (courtesy of P. Spillantini), which show the differential and integrated momentum distributions of pions in $e^+e^- \longrightarrow 2\ \pi^+\ 2\ \pi^-$ and kaons in $e^+e^- \longrightarrow K^+K^-\ \pi^+\ \pi^-$ at W = 1. 6 GeV according to phase space. We shall therefore worry about momenta $\lesssim$ 600 MeV/c.

The method of particle separation based on p_{ch} vs. TOF has been studied for MDA by G. Barbarino and S. Patricelli. The TOF counters in MDA are arranged in two cylindrical layers at $\sim$ 10 and $\sim$ 90 cm from the beam. The dimensions are 200 x 4 x 0.5 cm^3 (16 counters), and 300 x 18 x 2 (4) cm^3 (32 counters). We plan to stick a photomultiplier at both ends of the counters. The estimates that are described in the following are relative to a single output. We expect an improvement by about a factor of $\sqrt{2}$ in resolution with respect to be estimates below by exploiting the information from both ends. We show in fig. 92 the TOF vs p relation for pions and kaons for $p \lesssim 600$ MeV/c and over a 75 cm path length. One sees that at 500 MeV/c τ_K $\tau_\pi \sim 1$ ns. This sets the order of magnitude of the resolution required to $\Delta\tau < 0.5$ ns. In the same figure is also plotted the specific ionization of kaons and pions in units of minimum ionization (right scale). It is well known that the start time of a fixed discriminator threshold depends on the pulse-height of the triggering pulse. This effect was calibrated in the laboratory and a law of this type was found

$$\tau_h - \tau_{h_o} = K \left(\frac{1}{\sqrt{h}} - \frac{1}{\sqrt{h_o}} \right) \text{(Ref. 51)}$$

The value of the constant K was found empirically by optimizing the time resolution provided by each counter, as explained in the following. Experimental tests were made in collaboration with the dibarion Rome-Group, by installing a counter telescope comprising two scintillators (H, N) of realistic size as shown in fig. 93. The electronics logic is also shown in the figure. In order to reduce the background trigger rate a coincidence was requested between the signal from high threshold discriminators fed by the signals from the two extremes of each scintillator (H, N) under study. The distance $S_1 - S_2$ = 7 m = 20 ns was used like a monitor for tagging incident pions and protons. For fixed positions of H, N relative to the beam (defined to about 0, 5 x 0, 5 cm^2 by C), the time distribution of the p. m. outputs from H and N relative to S_2 was measured. Example of such data are shown as full hystograms in fig. 94. a, b. The broken hystograms give the data after applying the correction for pulse-height dependence of trigger time. It is seen that the correction is most effective ($\gtrsim$ 10% improvement in resolution) for the largest counter, where fluctuations are largest.

In long counters like those being considered, the output pulse-height suffers not only large statistical fluctuations, but also varies stronghly in a systematic way depending on the distance of the particle from the photomultiplier. If f(t) is the time distribution of creation of ionization centers along the track and $\frac{1}{\tau} e^{-t/\tau}$ is the normalized decay probability for emission of scintillation light ($\tau \sim 3.3$ ns), the natural time distribution of the light emission per unit of solid angle is

$$\frac{dI}{dt} = \frac{1}{4\pi\tau} f(t)^{-t/\tau}$$

If the source is at distance d from the photocathode, the light received at time t was emitted at the delayed time $t - \frac{d\,n}{c \cos\vartheta}$, where ϑ is the polar angle of light emission relative to the photomultiplier, $\frac{c}{n}$ is the speed of light in the scintillator, and $\frac{d}{\cos\vartheta}$ in the path. Assuming that one collects all and only the light emitted below the total reflection angle ϑ_0, the time distribution of the light arrival on the photomultiplier is

$$\frac{dI}{dt} = \frac{1}{4\pi\tau} \int_0^{\theta_0} f(t - \frac{dn}{c \cos\theta}) \, e^{-\frac{1}{\tau}(t - \frac{dn}{c\cos\theta})} d\Omega =$$

$$= \frac{1}{2\tau} e^{-t/\tau} \int_0^{\theta_0} f(t - \frac{dn}{c\cos\theta}) \, e^{\frac{dn}{c\cos\theta}} d\cos\theta \quad ;$$

The distribution computed according to this formula as a function of d (after assuming a step function for f (t) is shown in fig. 95. Notice that d = 50 cm is a realistic estimate for the length of the light-pipe. The pulse height scale is derived by assuming 10^4 useful photons for cm of plastic, a quantum efficiency of 10%, a photomultiplier gain of 10^8 and an output resistence of 50Ω . It is seen that for standard values of discriminator threshold (10 to 30 mV on 50 Ω) the trigger time is expected to vary more than 1 ns when the impact point varies by 3 m (fig. 42). This shows very clearly the importance of employing low threshold discriminators (and consequently of using different discriminators for triggering and for TOF measurement), as shown in fig. 93. The dotted hystogram is obtained after applying the pulse-height correction (as in fig. 94 a, b). The overall resolution is about ± 0.35 ns. One sees that the two particles are satisfactorily separated. Notice that the p/π ratio in the beam is about 5%, which is also of the same order as the expected K/π ratio at ALA. These results are considered satisfactory, also in view of the fact that in the off-line analysis, when the impact point on the scintillators will be separately determined from the reconstructed tracks in the central chambers, one will be able to correct the time reading of each p. m. and to further improve the resolution. Fig. 96 shows in detail the expected jitter for two and four cm thick scintillators and for different level of discrimination. When reading separately the pulses at the two scintillator ends and taking the mean of the time information (fig. 93) this effect is compensated to a first order.

In the experimental tests, counters H and M were set at a distance of 38 cm such that the TOF difference between pions and protons in the 600 MeV/c positive beam ($\sim$ 1.1 ns) was very similar to that expected for 500 MeV pions and kaons in the experiment. Typical results of the analysis are shown in fig. 97.

VI. 4. - The photon detector.

A problem of great importance in MDA is the detection of low energy photons. While in the reconstruction of low energy π^0's and η's decaying into two gammas the space resolution is often more important, a good energy resolution is essential down to low energy in the search for radiative decays. These are in practice conflicting requirements (at list if one wants to limit the cost), and one must make a compromise when choosing the experimental technique. The MDA team has taken the attitude to test a number of detector prototypes in order to make the final decision as much as possible on the basis of pratical data. One such prototype will be an assembly of sodium iodide chrystals or chrystal fragments immersed in a suitable liquid. This detector is conceptually simple and mechanically similar to a matrix of lead-glass blocks, and should be relatively easy to assemble and operate. The main parameter to be checked is the cost as a function of resolution achievable with different types of chrystals. Work on this type of detector has started since a few months, and the first tests will be made in spring 1979.

Typical resolution curves for a number of photon detectors at $E_\gamma < 500$ MeV are shown in fig. 98. The band enclosed between Pb-glass and NaI counters should be considered as the area of acceptable resolutions for this experiment. This can be understood first of all on the basis of the expected photon energies from π^0-decay. For example, the reaction $e^+e^- \longrightarrow 4\pi$ at W = 1500 MeV gives a γ spectrum with $< E_\gamma > \sim 140$, as shown in fig. 99 (phase-space Montecarlo). In addition and more important, the radiative photons expected at ALA are also in the same energy range (10 - 200 MeV, of the same order as the spacing between resonances), as possibly anticipated by the inclusive photon spectrum reported in fig. 100. This figure shows (ref. 52) that $\bar{p}p$ annihilation at rest the observed photons (hystogram) are much more abundant than what expected on the basis of isospin conservation in pion production (full curve). If baryonium states will be produced at ALA, their decay products are likely to show the same anomaly.

The prototype detectors which have been studied in detail are liquid argon calorimeter specially designed for high resolution at low energy called LELAC, and a cheap and practical version of a sandwich calorimeter employing resistive streamer tubes called TULAC (tube calorimeter). Details on these two photon detectors will be given in the following.

VI. 4. 1. - TULAC.

The design of this detector is due to G. Battistoni, E. Iarocci, M. M. Massai, G. Nicoletti and L. Trasatti. The detector emploies proportional tubes of original conception (53). If the cathode of a proportional tube is made of high resistivity material (a carbon-glue coating on a platic dielectric), induced pulses signalling a traversing particle can be detected outside the tube. The principle of operation is illustrated in fig. 101. In this particular example the induced pulses are read-out by a wire wrapped as an helix around the plastic tube. The helix/dielectric/shield sandwich works as a delay line whose specific inductance and capacitance can be approximately computed as the difference between those of the inner and of the outer cylindrical conductors. This allows to derive the characteristic impendence z and the propagation time τ of the line

$$z_o = \sqrt{\frac{L}{C}} = 377 \frac{1}{\sqrt{\varepsilon_r}} \frac{d}{p} (\Omega), \qquad \tau = \sqrt{LC} = \frac{\sqrt{\varepsilon r}}{C} \frac{\pi(D + d)}{p}$$

where ε_R is the dielectric relative constant, D the helix diameter, d the distance between helix and shield, and p the helix pitch. Typical experimental values for z_0 and τ are (PVC tube, 17 mm inner, 19 mm outer diameter with a 40 μ sense wire and a 2 KΩ/cm resistive cathode coating, equipped with a 1 mm pitch helix covered with a 0.15 mm thick teflon foil and 50 μ Al shield) τ_{ex} = 3 ns/cm, z_{0ex} = 92 Ω , while the predicted values on the basis of these formulas are τ_{th} = 2.9 ns/cm, z_{0th} = 76 Ω . In these detectors the wire pulse is negative with rise-time of $\sim$ 20 ns, and the helix pulse is positive with rise-time varying from a minimum of 30 ns for short propagation distances to about 150 ns for distances of 2 - 3 m.

The resistive tube technique has been continousily improved to achieve easyness of construction, reliability, better resolution. The tubes are chosen to operate with a Argon-Isobutane mixture (typically 50% each, more isobutane being needed for tubes of smalled diameter) in the limited stremar mode. In this regime the anode potential is high enough to initiate strong discharges such as to provide large (at least 40 mV over 50Ω) output pulses. Such large pulses are necessary if one wants to exploit induced pulses on sorrounding electrodes in the read-out, as explained below. The concentration of isobutane, which absorbe the ultraviolet photons emitted in the discharge, is large enough to prevent the propagation of the discharge along and across the tube. Modules comprising eight tubes of square section as small as 8 x 8 mm^2 have been developed, on which signals induced by the discharges are read-out through orthogonal stips. A sketch of such a 8-tube is shown in fig. 102. The eight wires are short-circuited and connected directly to HT. Longitudinal strips 0, 6 cm wide on the outside of the insulating tube are read-out rather than the wires. The transverse coordinate is provided by transverse strips, typically 2 cm wide, on the opposite side of the tube.

The system is sandwiched between two 1 mm thick PVC insulating layers and two grounded 50 μ thick aluminium shield layers. With this system the output pulses are transmitted on the characteristic impendence of the read-out cable and have a rise and fall time which is determined by the capacitance of the strip relative to the shields. The relevant parameters (strip surfaces, thickness of insulator) can be chosen such as to give $\tau_{rise} < \tau_{fall} \lesssim 200$ ns for pulses $\gtrsim 10$ mv/50Ω. The wire pulse height depends on the wire diameter, on the gas mixture and on the applied potential, and is chosen to be $\gtrsim$ 50 mV/50Ω .

The operation of sizable assemblies of resistive tubes has been tested in the central detector of the $\gamma\gamma 2$ Adone experiment, comprising 330 circular tubes 18 mm in diameter and 80 cm long. In this detector 384 transverse strips in addition to the 330 tube wires were read-out. Typical parameters of the detector (fig. 103) were 50 KΩ/cm resistivity of the conductive coating, 100 μ wire thickness, and 65% Ar, 35% C_4H_{10} gas mixture. The detector has worked well, with 96% layer efficiency for single tracks (ref. 53). A detailed comparison among the performances of single and multiple circular tubes 18 mm in diameter, and single and multiples square tube 8 mm in diameter has also been made (ref. 54). The dependence of rate on the applied potential (SR^{90} source) for a tube of the Adone Experiment is shown in fig. 104 for various Argon/Isobutane concentration. One observes that it is easy to obtain a large plateau (as a consequence of the limited streamer mode of operation which provides a pulse-height distribution with a sharp lower cut). The recovery-time of the tube depends on the applied voltage. Below ~ 3.7 KV it is as small as ~ 100 μs$\cdot$cm. At voltages of the order of 4.2 KV it increases to ~ 300 μs$\cdot$cm because of a number of after-pulses following the primary one. Even so, the tube performances look fully adequate for a machine of a relatively low background rate as ALA. The efficiency of a layer of 18 mm diameter tubes has been measured with cosmic rays and found to be ~ 96% (ref. 54). For a 8 x 8 mm^2 square tube the HV plateau is less wide but still quite acceptable (see fig. 105). On compairing with fig.104 one sees that larger C_4H_{10} concentrations are needed to get wide plateaus. Similar curves are obtained (at a potential lower by ~ 1000 KV) if 40 μ diameter wires are used rather than 100 μ ones (as in fig. 105). The recovery time is still ~ 200 μs$\cdot$cm even at the highest plateau potentials (~ 5.5 KV). The efficiency of a layer is measured with cosmic rays to be ~ 98%. The improvement with respect to the layer of circular tubes is to be attributed to the reduced dead-spaces in between the square tubes.

In MDA, resistive tubes working in the limited streamer mode can be employed in a number of ways. The main photon-detector can be made out of lead-tube sandwiches. Also, a number of sheets can be sandwiched around the magnet yokein order to detect neutral hadrons. Finally, the muon detector is made out of tube layers interleaved with iron walls. These detectors will be described later. We shall outline here the design of the photon detector employing resistive tubes as sensitive elements. A sketch of TULAC is shown in fig. 106. The system has an octagonal section with $\frac{\Delta\varphi}{2\pi} \sim 97\%$. Polar angles larger than $\vartheta_{MIN} \gtrsim 37°$ are covered, corresponding to $\frac{\Delta\Omega}{4\pi} \sim$ 76%. The length of the detector is as large as the ALA straight section, i. e. 3.0 m. A realistic stratigraphy of each element of the octagon is shown in fig. 107. Thirty tube layers interleaved Pb-sheets of thickness add up to a total of 6 x_0. A Pb-scintillator sandwich completes the energy measurement of the cascade. Noticе that the first layer of counters has been introduced for an additional TOF measurement on charged hadrons (after traversal of ~ 0.3 λ_{int}). The overall thickness of the detector is 8 x_0. Such a system would employ ~ 22000 tubes (of 10 x 10 mm^2 section). The information bits to be read-out would be ~ 22000 from the parallel strips and 24000 from the longitudinal ones (2 cm wide). The ϑ, φ projections of the cascade centroid would thus be measured to $\lesssim$ 2 cm and $\lesssim$ 1 cm respectively. The photon energy would be sampled twice, by the multiplicity of the longitudinal and transverse strips. The number of traversed layers, and more the pulse-height in the Pb-scintillator sandwiches, would implement the energy measurement.

The energy resolution of such a calorimeter is hard to estimate. One expect it to improve when decreasing the tube section: this is why tubes as small as 8 x 8 mm^2 have been developed. It will also depend on the $\frac{dE}{dx}$ sampling made by means of scintillation counters. A Montecarlo computation (by G. Battistoni and L. Trasatti) is in progress to evaluate these effects, while a prototype calorimeter will be tested in spring 1979. Results of the computation have been obtained in the case of a calorimeter comprising 30 layers of 10 x 10 mm^2 square PVC tubes, interleaved with Pb-Al sheets up to a total of 6 x_0, set behind a $\frac{1}{3}$ x_0 Al-layer (to simulate the magnet coil). Layers have been assumed to be 100% efficient. Electrons are assumed to be lost when they reach $\sim$ 0,35 MeV (approximate energy needed to cross the tube wall). The physical processes taken into account are pair production, Compton scattering and photoelectric effect for photons, bremsstrahlung and single and multiple scattering for e^+ and e^-, and annihilation for positron. Electrons and positrons loose energy both for ionization and for soft photon emission. The computed detection efficiency for photons and electrons up to 200 MeV are shown in fig. 108 for two possible photon signatures. The average number of hit tubes is shown in fig. 109. a, b. The photon energy resolution, based on tube counting only, is shown in fig. 110. The standard deviation of the measurement is $\sim$ 20% at all energies.

The small calorimeter prototype which is ready for test on a beam is sketched in fig. 111. Three hundred cylindrical tubes as those employed at Adone are assembled in 20 layers and interleaved with Pb-sheets up to 4 x_0. A thin counter in front of the detector is used to separate charged particled from photons. A thick counter behind provides some pulse-height information. An example of Montecarlo predicted distribution for this set-up is shown in fig. 112.

VI. 4. 2. - LELAC.

The design of this detector is due to C. Cerri, F. Sergiampietri and M. Spadoni.

Notwistanding the mechanical and criogenic difficulties associated to the use of large volumes of liquid Argon (boiling point $\sim$ 70 °K), liquid-Ar calorimeters have been used in several modern experiments for a number of important quality feature favouring a stable and linear response to energy loss. The principle of operation is the following. When a charged particle (the electrons in the e. m. shower in our case) crosses a sheet af liquid Ar between two planar electrodes, the ionization electrons drift under the action of the uniform electric field and are collected by the anodic plate. In such a geometry the field does not reach values high enough to generate an avalanche (notice the difference with respect to wire chambers, where $E \sim \frac{1}{R}$. Liquid Argon can be purified enough (less than a few p. p. million residual oxigen) that the action of electronegative elements can be neglected and the collected charge made precisely equaly to the primary ionization. The signal provided by the calorimeter is therefore calculable

$Q = \frac{\Delta E}{W} \cdot e$, with ΔE = energy loss in the gap, W = ionization potential in Ar (23 eV), e = electron charge. Liquid Argon is chosen rather than gas in order to have a reasonably short radiation length (x_0 = 14 cm).

The natural pulse shape provided by a cell is determined by the electron drift velocity in the liquid, which corresponds to risetimes of a few hundreds of ns a gap a few mm wide. On the other hand, with the adopted electronic times as long as 100 μs can be needed for amplification and digital conversion by the electronics. This value sets the resolving time of the detector.

Conceptually the calorimeter is very simple: it consists of a series of planar metal electrodes immersed in the liquid and set at ground and high voltage alternatively. The positive electrodes are suitably split to provide space information. A prototype calorimeter (LELAC) with proper parameters for providing optimum detection of low energy photons will be described in the following. To design such a calorimeter a number of general arguments must be taken into account, according to the following lines (ref. 55). The charge flow on the anodic plate is equivalent to a current generator feeding in parallel a condenser (the two plates separated by a sheet of liquid Ar) and the input circuit of the read-out amplifier. An equivalent circuit is shown in fig. 113. A transformer with input/output winding ratio 1/n is needed to adapt the impedence. C_D is the detector capacity, and C_A is the equivalent input capacity of the amplifier ($C_A \sim 20$ pF in the adopted electronics). One can show that the optimum energy transfer by the transformer is obtained when $n = \sqrt{\frac{C_D}{C_A}}$. With $n = n_{opt}$ the voltage signal on the amplifier input is $V_{in} \simeq \frac{Q\ \text{ionization}}{2\sqrt{C_D C_A}}$

This formula shows that any thermal noise in the amplifier (more precisely, in the emitter resistence R_A of the field-effect transistor in the amplifier, $R_A \sim 60\ \Omega$ in the adopted electronics) is equivalent to a fake charge $Q_{noise} \sim 2\sqrt{C_D\ C_A}\ V_{noise}$. At a temperature T the noise signal is given by (ref. 50) $V^2_{noise} = 4\,KT\;R_A\,\Delta\omega$ where $\Delta\omega$ is the frequency band of the amplifier. One sees therefore that $Q_{noise} \sim 2\sqrt{C_D}\,\sqrt{C_A}\,\sqrt{4\,KTR_A\,\Delta\omega}$, i. e. $Q_{noise} \propto \sqrt{C_D}$, C_D being the only parameter depending on the design of the detector. In order to have Q_{noise} as low as possible, one must minimise C_D. Since one must eventually integrate over the physical size of the shower, this can be done in practice only by increasing the gap size.

An important phenomenon to be taken into account when choosing the detector parameters are the sampling fluctuations of the charge released in the sensitive volume, which influence directly the energy resolution. These are not only due to the overall ratio of sensitive (Ar) to dead (metal plates) volume, but also grow with the gap width. This is because the gap width gives the range of variation of track length both at the start and at the stop of each ionizing track in the calorimeter. Although the precise law by which effect depends on gap width is not fully clear, the situation is qualitatively as illustrated in fig. 114.

Using available information from previous detectors one find, for the particular parameters of our electronics and for aluminium plates of the geometry illustrated below, that the overall (r. m. s.) fluctuations are smallest for a gap δ = 2.5 mm. In the LELAC prototype a slightly different δ has been chosen for mechanical convenience, δ = 3, 2 mm. The electrodes have been made of Aluminium (small atomic number and still good mechanical resistance), with thickness 1.0 and 0.5 mm for the HV and ground electrodes respectively (minimum thickness being limited by mechanical considerations). The HV plate is a strip 2, 5 cm wide and of average length ∿ 40 cm. The ratio of energy loss in Argon and in the plates is very large (66%) while the energy loss per cell is very small ($\lesssim$ 1 MeV). These values are dictated by the requirement of good energy resolution for low photon energies.

A drawing of the container of the prototype calorimeter LELAC is shown in fig. 115. The relevant parameters of the calorimeter are quoted in Table VI.

TABLE VI - LELAC parameters.

Ground plates	number	129
	dimensions (cm^2)	40x40
	thickness (cm)	0.05
Signal (HV) plates:	number	17x128
	dimensions (cm^2)	2.5x40
	thickness (cm)	0.10
Liquid argon gaps:	number	256
	dimensions (cm^2)	40x40
	thickness (cm)	0.32
Mean density (g/cm^3)		1.64
Energy loss/cell (MeV)		1.02
a % of energy lost in Argon		0.66
Total radiation length:	longitudinal	8.03
	transversal	1.6
Channel:	longitudinal number	8
	transversal number	17
	total number	136
	gaps/channel	32
	dimensions (cm^2)	2.5x40
	length (cm)	12.64
	length (rad. L.)	1.0
	capacitance (pF)	1064
	ENE (MeV r. m. s.)	0.46

The electrodes are octagons, with diameter $\Phi \sim 50$ cm. The HV electrode is split into 17x2.5 cm wide strips at 1 mm from each other. The strips are inclined by 45° with respect to the vertical axis. In future tests they will be alternatively inclined right and left. The 128 HV plates are divided longitudinally into 8 groups of 16 electrodes, and for each group all strips at equal distance from the axis are connected toghether to make a channel. In total one has thus 17 x 8 = 136 read-out channels. The energy measurements is obtained by adding the charge collected in all channels over which the signal is larger than the noise. The hand-estimated energy resolution, after taking sampling fluctuations and noise into account, turns out to be 10%, 7%, 3% at E_γ = 50, 100, and 500 MeV respectively (standard deviation).

A Montecarlo calculation has been developed (by M. Spadoni) to provide a more accurate estimate of the space and energy resolution expectet from LELAC. The physical processes taken into account were the same as for the TULAC Montecarlo. At the end of the cascade, electrons are assumed to loose all their energy uniformely along their residual range when they reach E = 1.5 MeV. Photons are stopped at E = 0.5 MeV. The energy dependence of the resolution is given in fig. 116. It follows approximately the law $\Delta E/E \sim 3.7/\ E$ % (f.w.h.m.).

The longitudinal and radial development of the cascade are illustrated in fig. 117 and 118, respectively, for 50 and 100 MeV incident electrons. Although for incident photons fluctuations of the order of tens of centimeters will be added on the depth of cascade origin, one sees that LELAC thickness ($\sim$ 1 m) should be sufficient to contain well all photons of interest at ALA. The radial dimensions of the cascades are of the order of centimeters, such that in the off-line analysis it should be possible to locate the cascade centroid to a few mm.

It is worth observing that $\frac{dE}{dx}$ measurements on the non-showering charged particles (μ, π, K, p) can also be made in a calorimeter like LELAC, provided each longitudinal cell is read-out separately. $\frac{dE}{dx}$ curves for liquid argon, for large (10 cm) and small (1 cm) sampling are shown in fig. 119. It is seen that a momenta as large as 400 MeV/c, $\Delta E_K/\Delta E_\pi$ is still $\sim$ 2.5. After taking into account fluctuations in energy loss and ripple due to electronics noise, one estimates that with 17 traversed cells by 400 MeV/c pions and kaons, the two pulse-height distribution would overlap at 8% of their maximum. The precise signal to-background ratio would of course depend on the rate of the rare particle to be separated. On the other hand, the available gaps in LELAC are as many as 256.

One can extend the electrode design of LELAC to a large coverage calorimeter for MDA, in an octagonal arrangement with inner radius of about 90 cm and outer radius of about 160 cm, as discussed for TULAC (fig. 106). The electrode strips in the octagon section would have to be set alternatively parallel and orthogonal to beam axis. For such a configuration the calorimeter volume would be $\sim 20\ m^3$, and the number of independent read-outs $\sim$ 9000.

VI. 5. - The μ -detector.

The importance of tagging single muons can be found in a search for leptonic or semileptonic decays of heavy leptons, unstable quarks, etc., as discussed previousely. However, this problem is experimentally difficult because of the low muon energies involved. On the other hand, the problem of separating $e^+e^- \longrightarrow \pi^+ \pi^-$ from $e^+e^- \longrightarrow \mu^+ \mu^-$ is much easier because of the back-to-back configuration of two monocromatic particles and is interesting in itself, since a clear separation between these two channels is necessary if one wants to extend the measurement of the pion form-factor to higher energies. This problem has been studied for MDA by S. Patricelli and U.Troya.

A straightforward way to tag the μ's is to filter them out in absorbes interlieved with detectors. A scheme of a possible arrangement is given in fig. 120. The overall thickness of the main detector, including the magnet return-yoke, is equivalent to $\sim$ 12,7 cm of Fe. Seven iron shields, 8,3 cm thick, are set behind the yoke and the particle transversal is detected in between them. One shows in fig. 120 the probability that a pion of a given energy is either absorbed or suffers a nuclear scattering at angles $\geq 25°$. This probability is near 100% after a few traversals. For instance for E_π = 1 GeV, this probability is $\simeq$ 95% after traversing five shields, while the probability for 1 GeV muons to suffer a Mott scattering at $\vartheta > 25°$ is $\sim$ 3%. Therefore a fiducial region $\vartheta < 25°$ is sufficient to accept $\gtrsim 90\%$ of the good μ -pairs, even at the lowest energies. There is, however an additional contamination due to π-decay in flight ($\vartheta_\mu \leq 5°$ even at the lowest ALA energies). We show in fig. 121 the probability for one pion from the reaction $e^+e^- \longrightarrow \pi^+ \pi^-$ to decay in flight such as to be accepted as a direct muon. We show in fig. 122 an estimate (ϱ -tail for the π form-factor) of the two competing cross-sections. It is seen that $\sigma_\pi/\sigma_\mu \gtrsim 1\%$ even at the highest energies. One thus concludes that the measurement is possible.

To cover an angular range $45° \leq \vartheta \leq 135°$ and $-45° \leq \varphi \leq +45°$ with such telescopes one would need $\sim$ 240 t of iron. As detectors, double layers of resistive tubes would be employed. For a space resolution of 2 x 2 cm^2, one would need $\sim$ 2 x 2000 three meter long tubes.

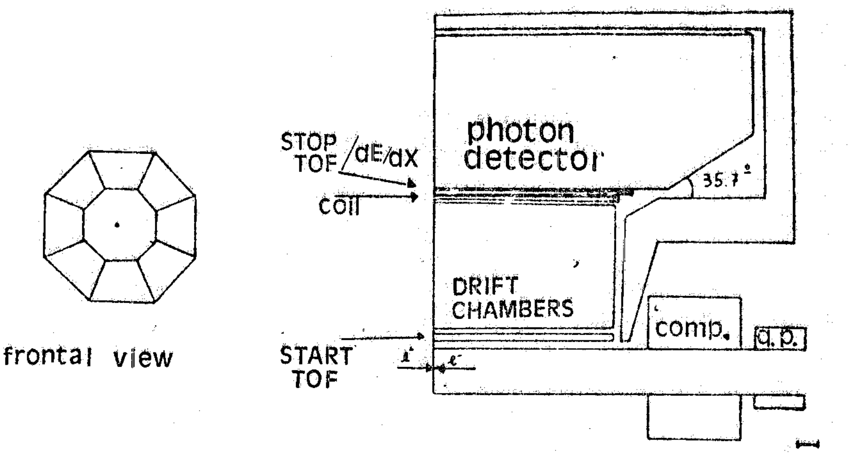

FIG. 55 - Schematic drawn of the detector.

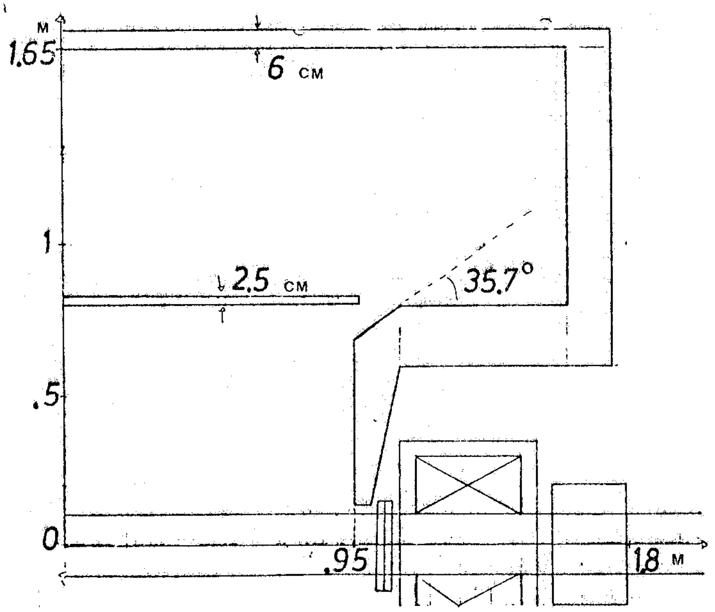

FIG. 56 - The magnet.

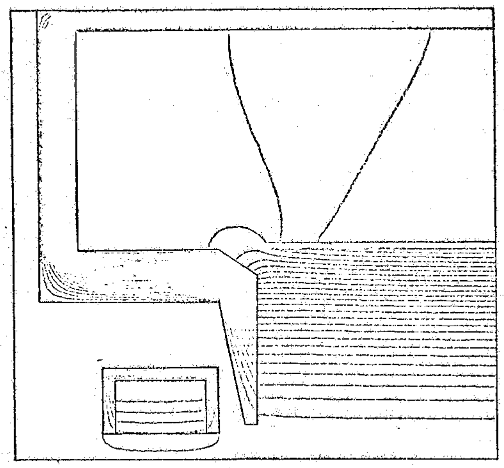

FIG. 57 - The computed field map.

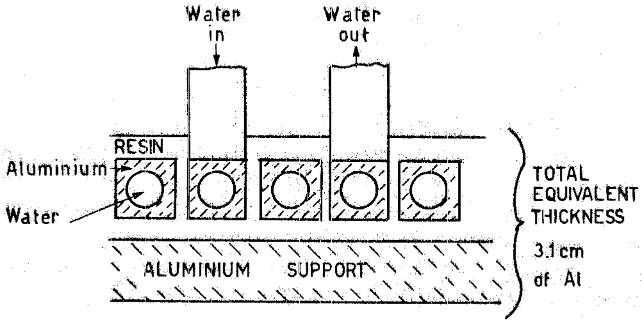

FIG. 58 - Drawing of the section of the coil.

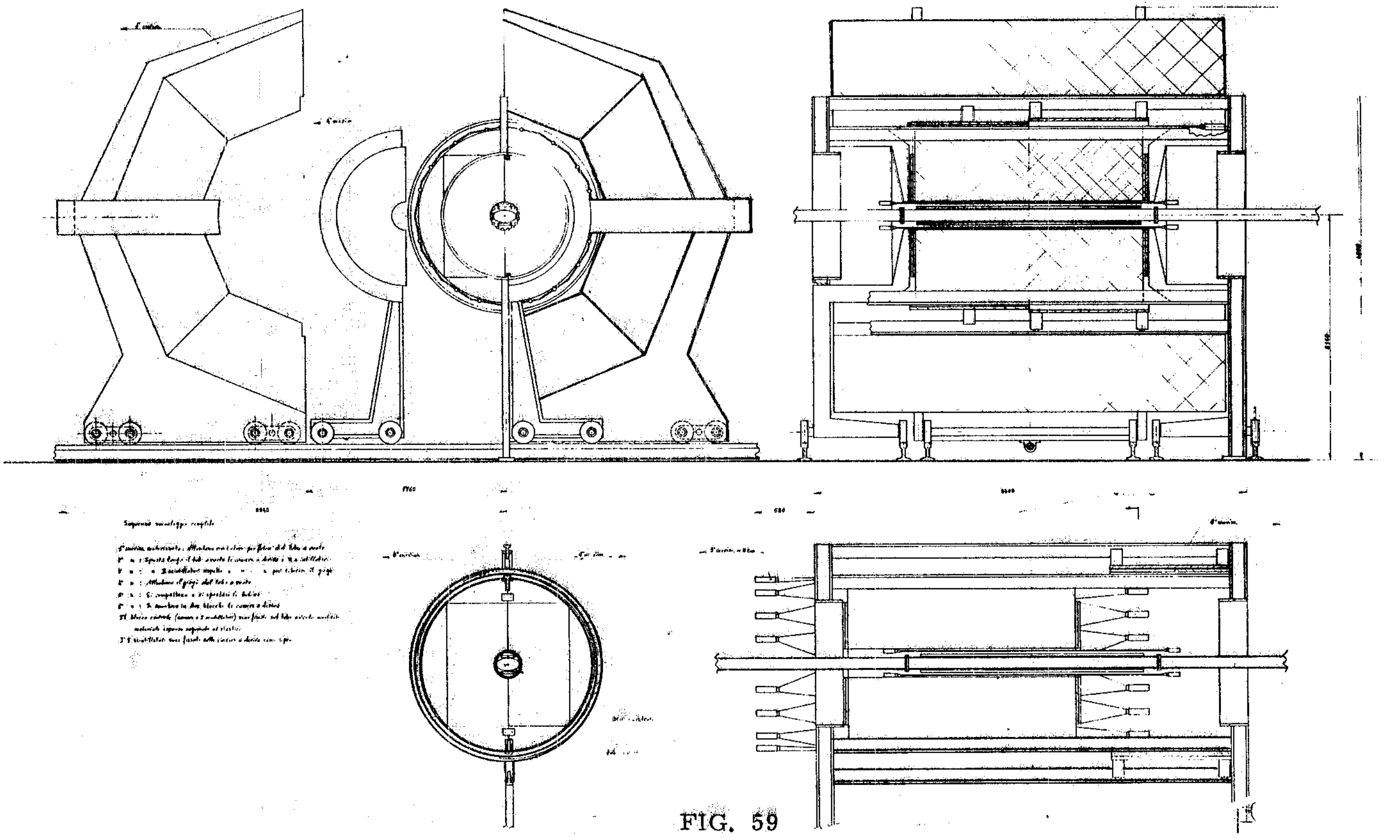

FIG. 59

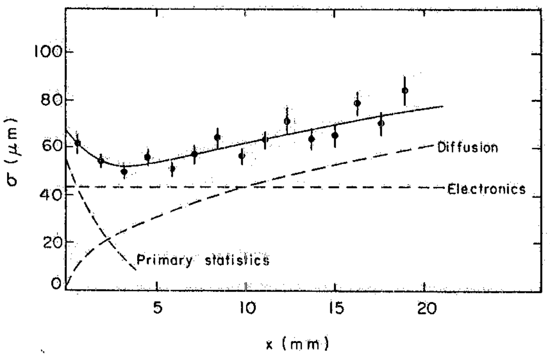

FIG. 60 - Measured intrinsic accuracy in the drift chamber as a function of drift space. The experimental results have been decomposed into three contributions : a constant electronics dispersion, a physical diffusion term function of the square root of the drift space, and a contribution of the primary ion pair statistics.

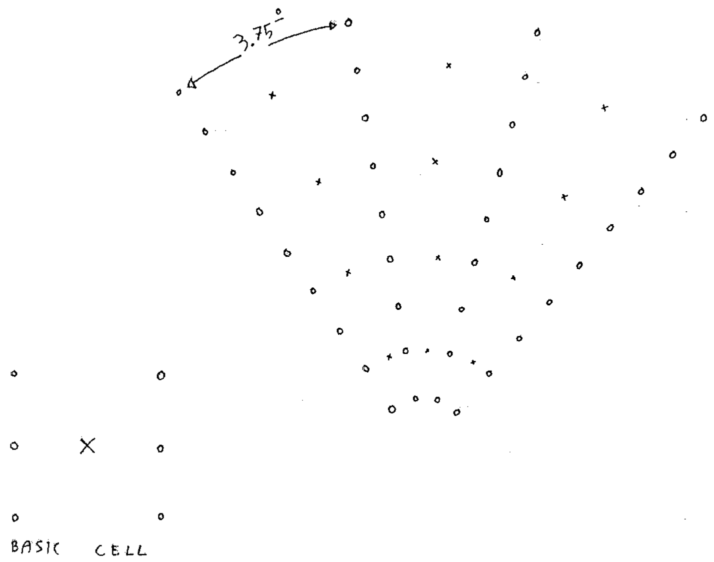

FIG. 61 - Drift cell arrangement in the central chamber.

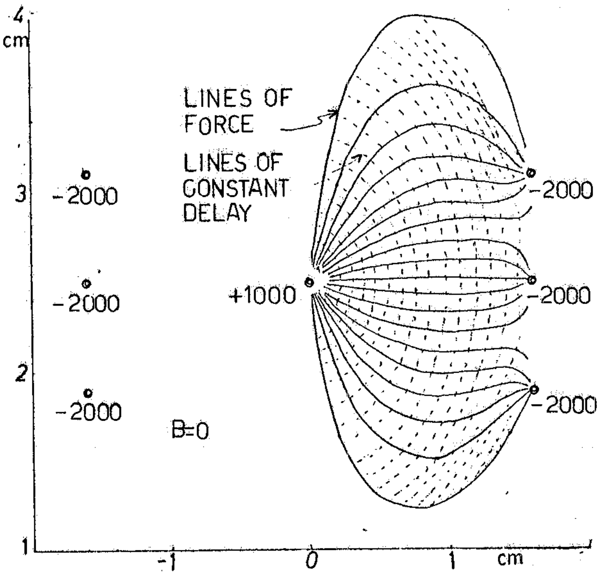

FIG. 62 - Lines of force and of equal delay for zero magnetic field.

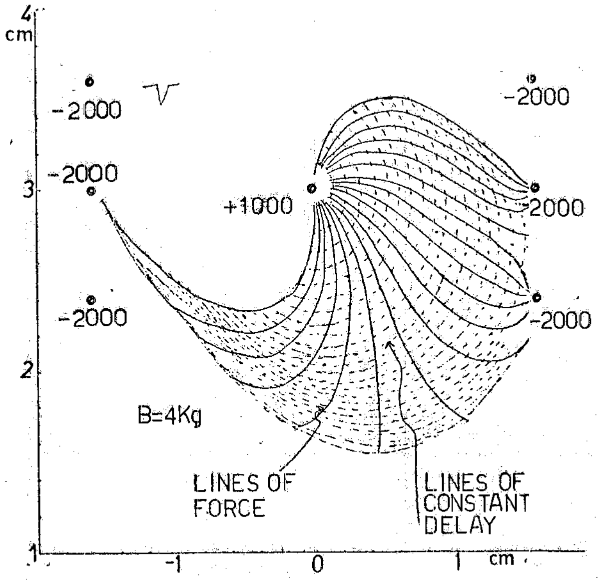

FIG. 63 - Lines of force and of equal delay for B = 4 KGauss.

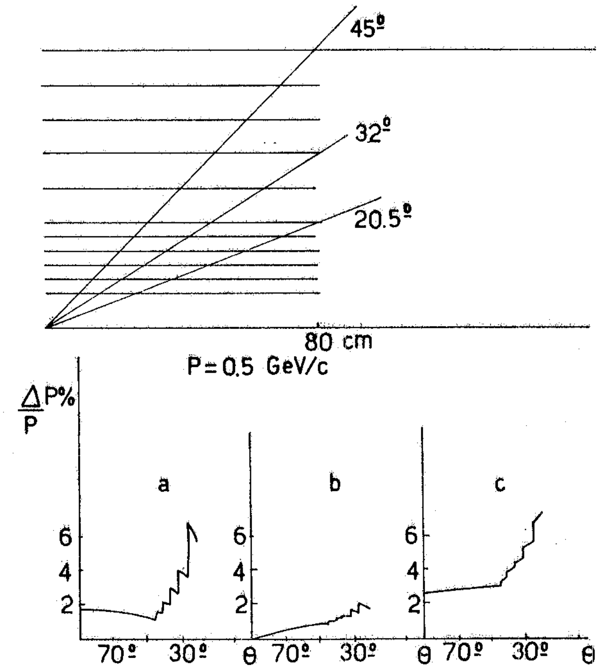

FIG. 64 - Expected resolution p/p:
a) contribution from error on ;
b) contribution from error on z ;
c) contribution from multiple scattering.

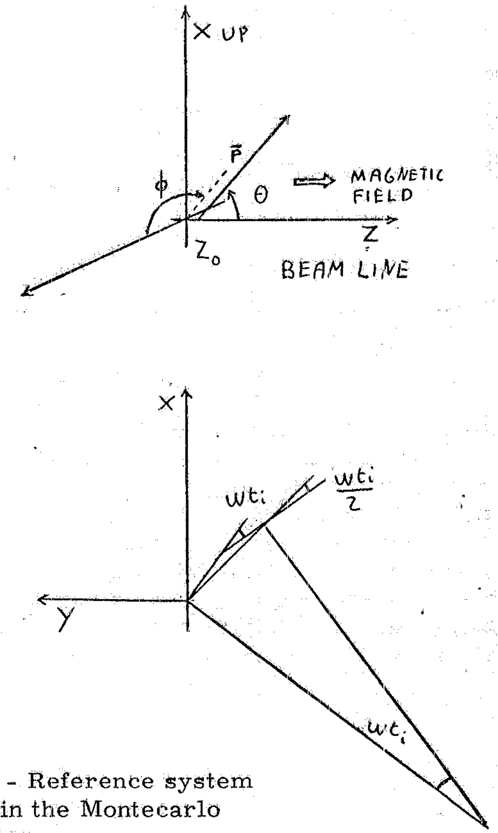

FIG. 65 - Reference system adopted in the Montecarlo calculation.

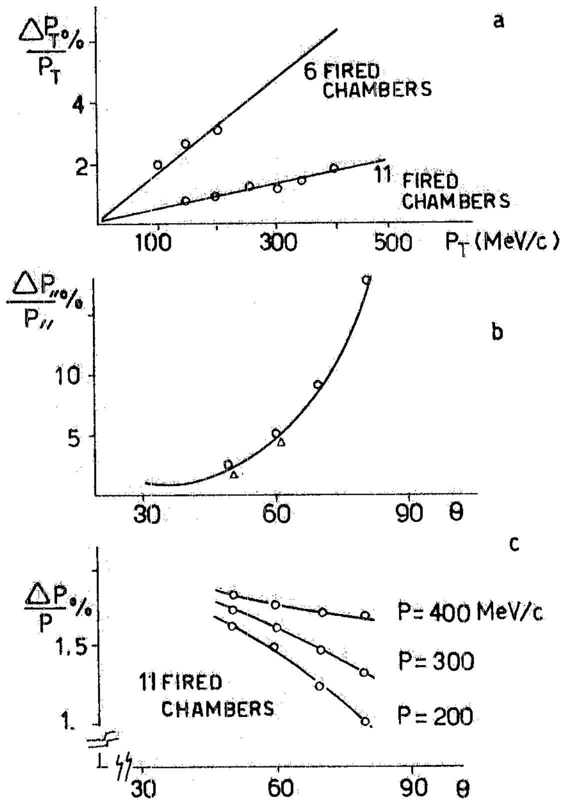

FIG. 66 - Montecarlo computed momentum resolution.

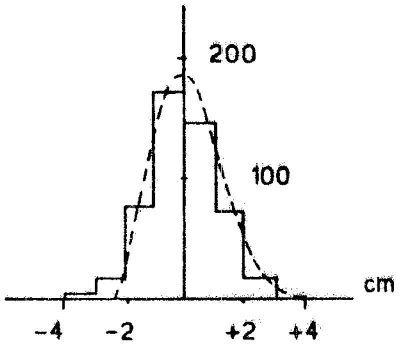

FIG. 67 - Target point reconstruction.

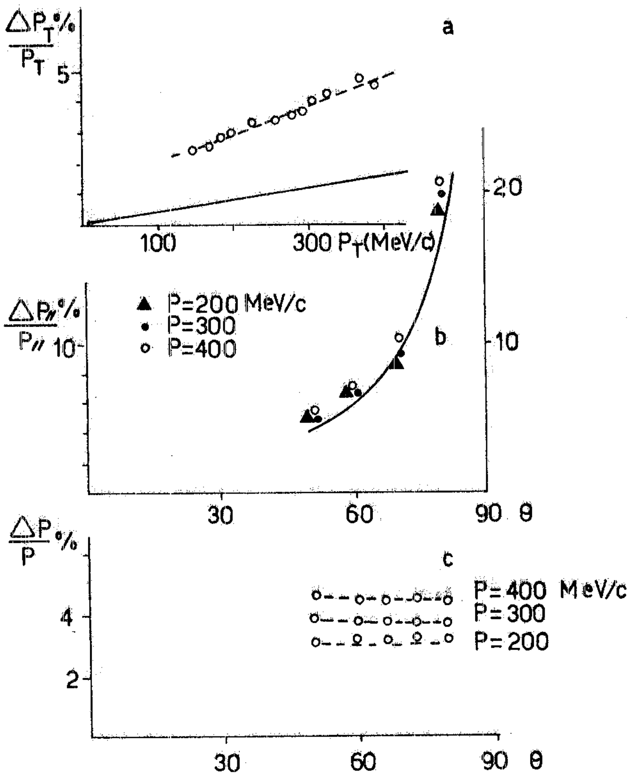

FIG. 68 - Montecarlo computed resolution with multiple scattering taken into account.

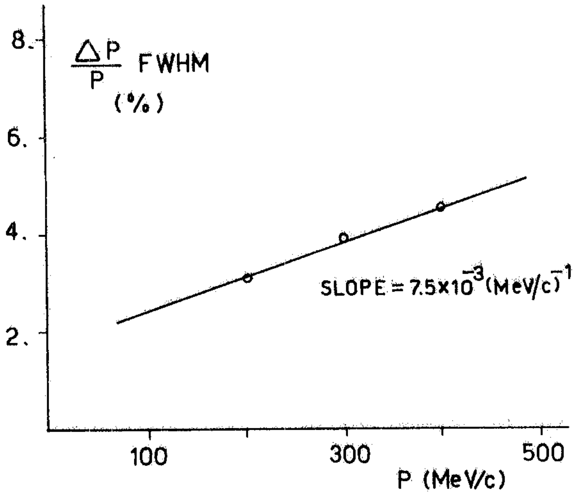

FIG. 69 - Overall momentum resolution.

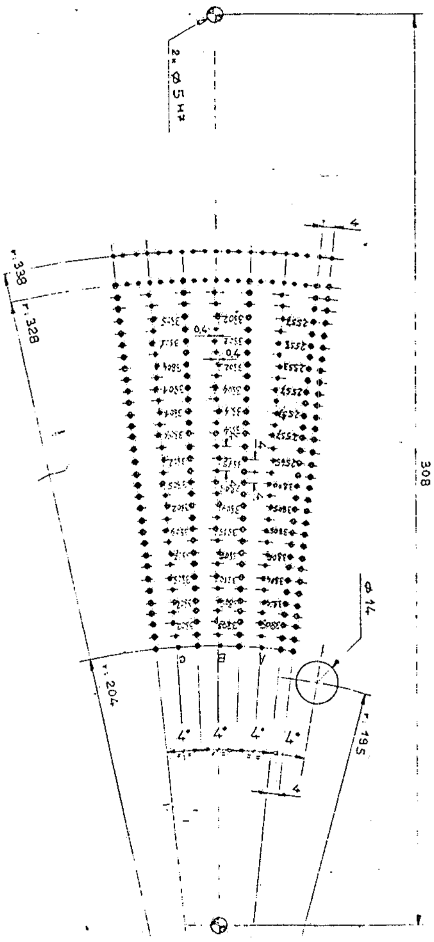

FIG. 70 - Schematic view of the R 807 prototype chamber.

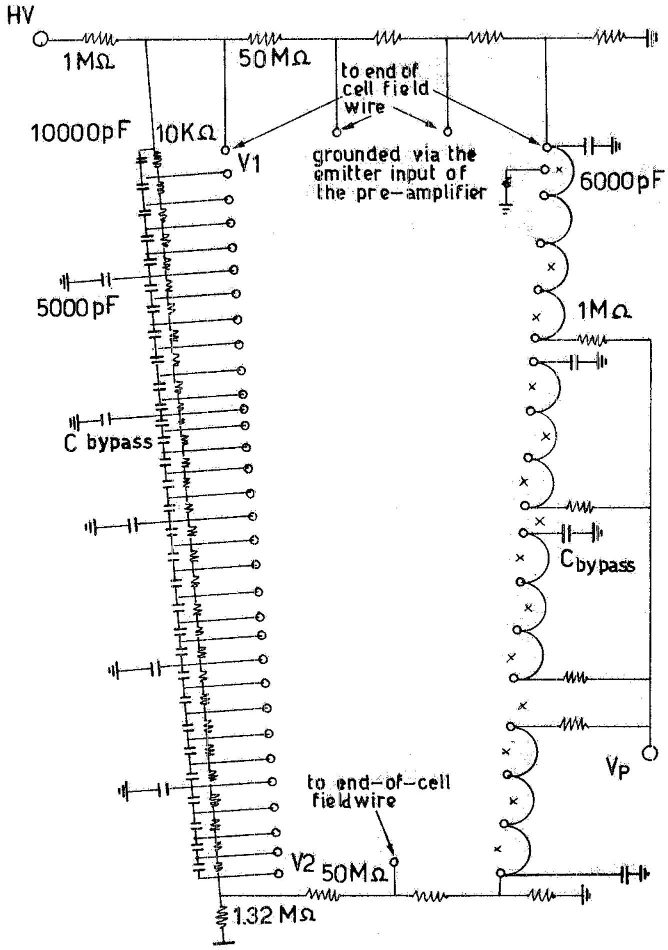

FIG. 71 - Supply scheme.

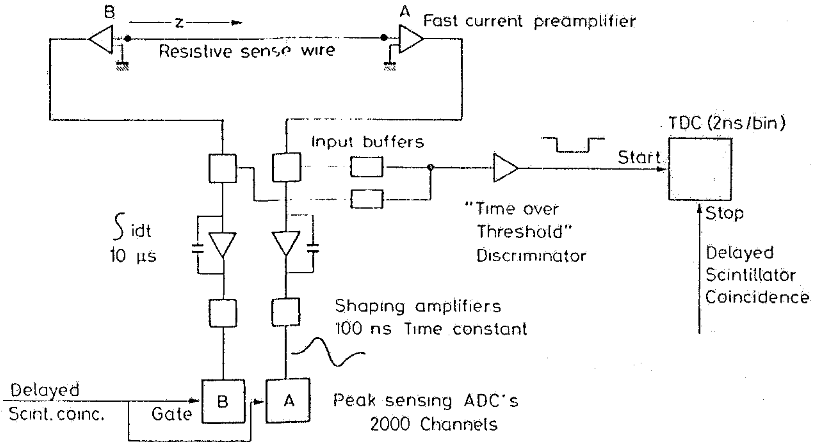

FIG. 72 - Block diagram of read-out electronics.

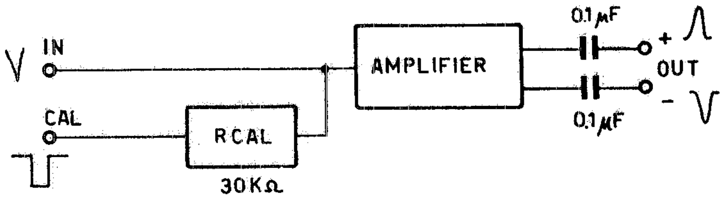

FIG. 73 - Preamplifier for drift chambers (R 807).

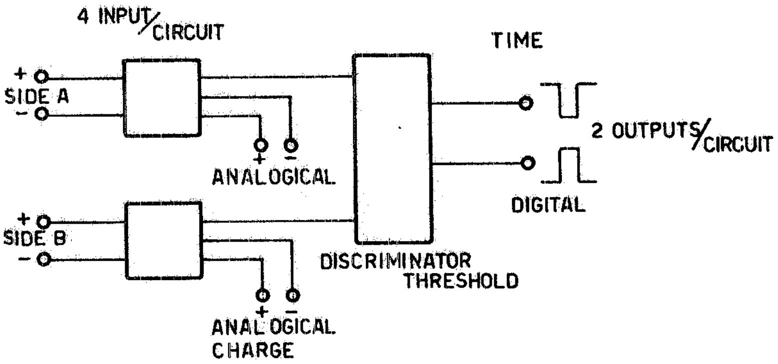

FIG. 74 - Time pick off.

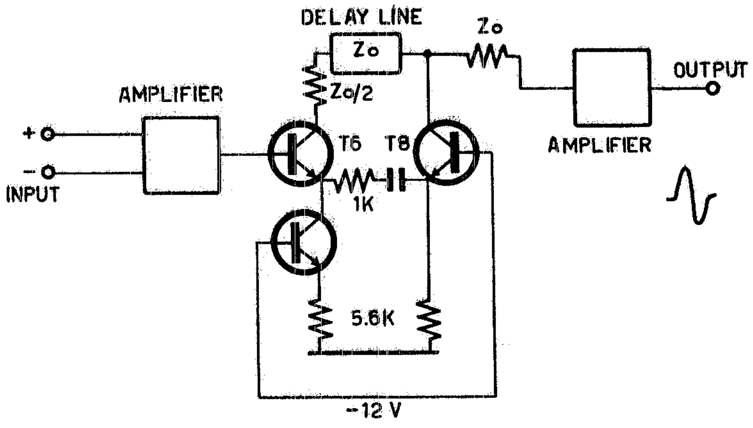

FIG. 75 - Charge and shaping amplifier.

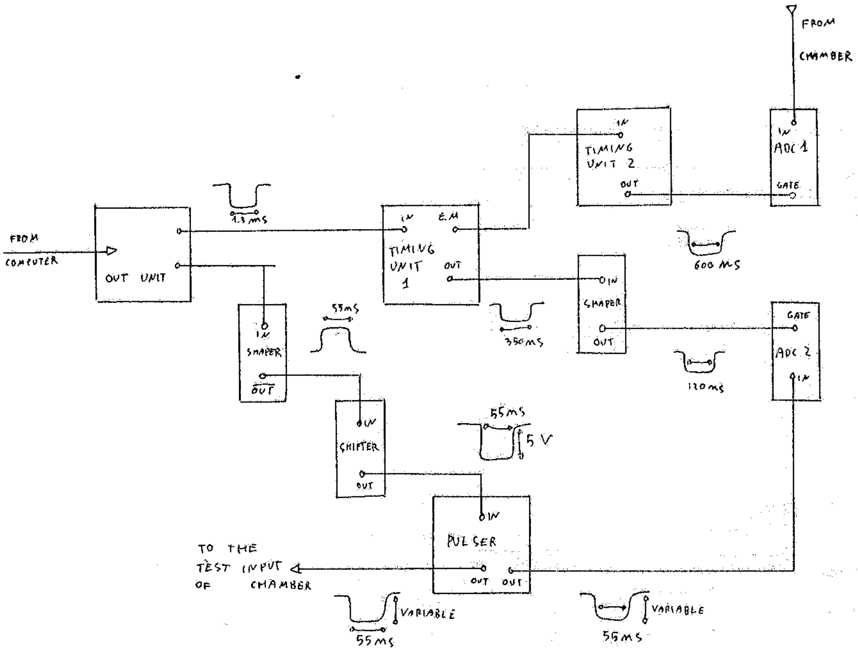

FIG. 76 - Electronics for the calibration.

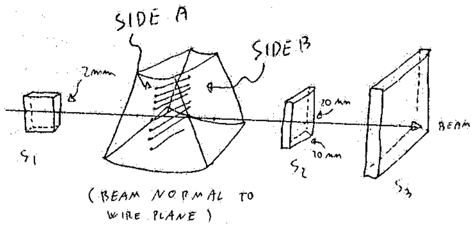

FIG. 77 - Arrangement on the test beam.

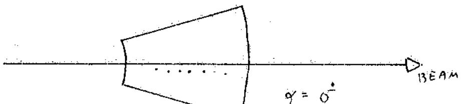

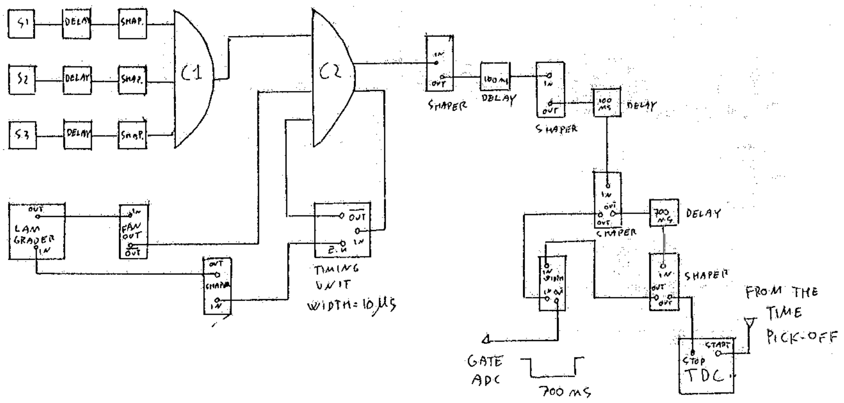

FIG. 78 - Electronics for data taking on the test beam.

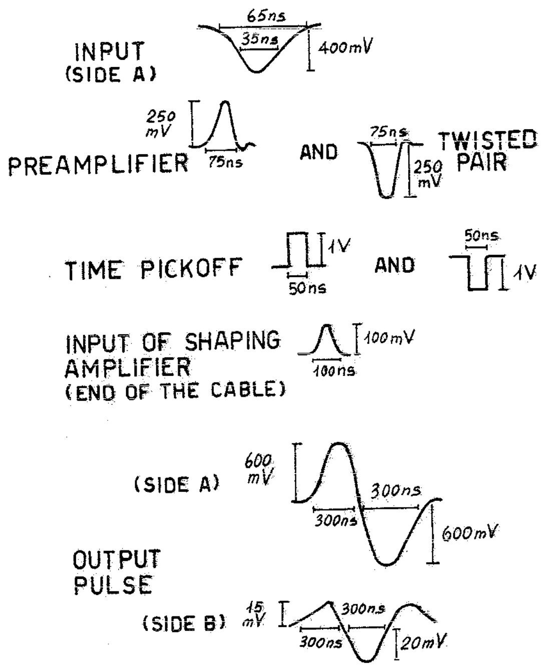

FIG. 79 - Pulses on the key points of the electronics.

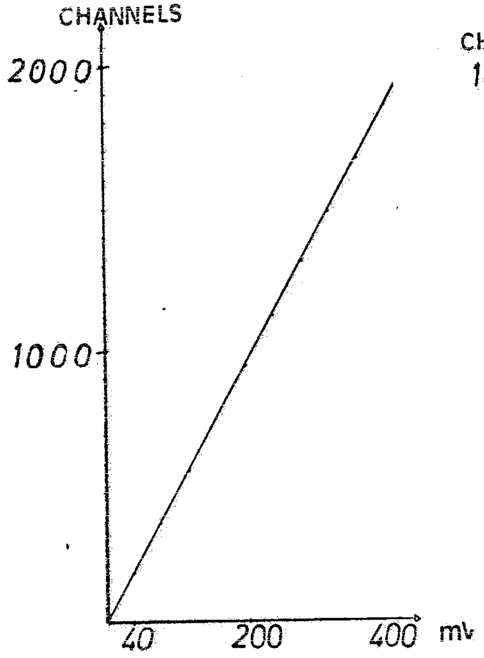

FIG. 80 - Typical ADC calibration curve.

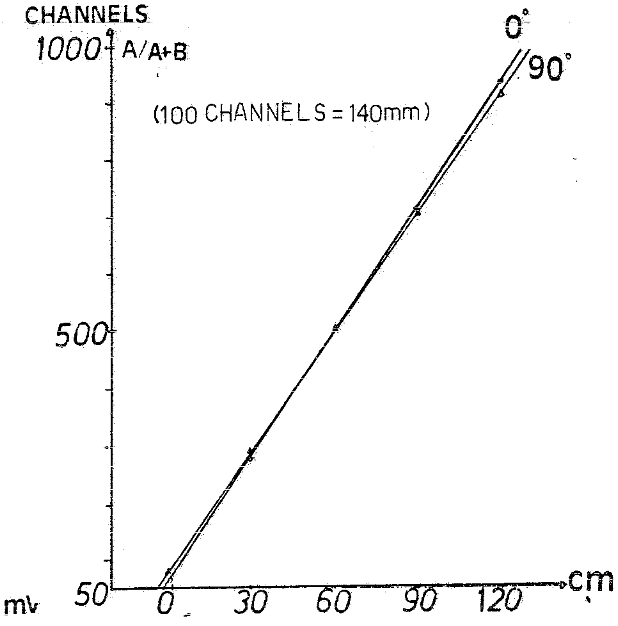

FIG. 81 - Linearity of charge division for two different positions of the beam (see Fig. 77)

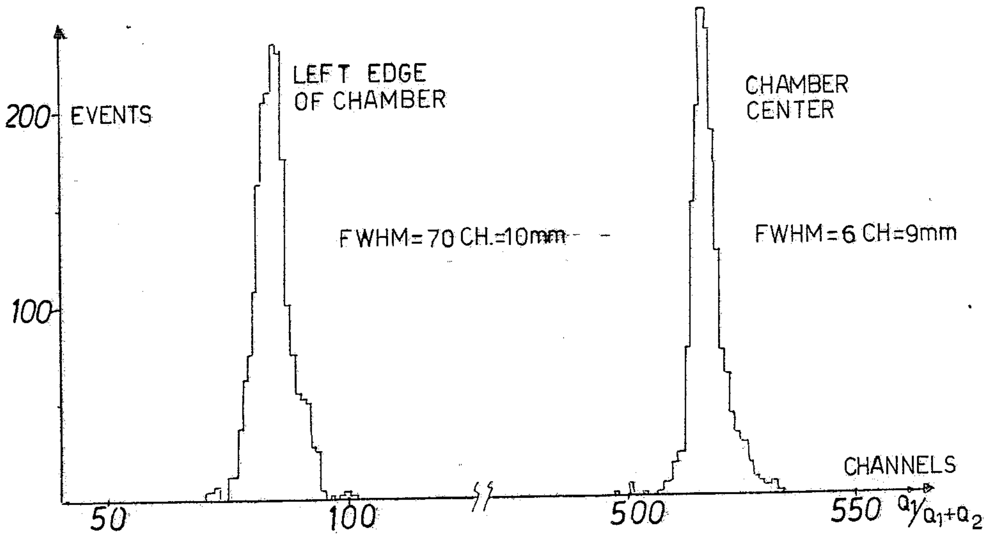

FIG. 82 - Charge division distributions.

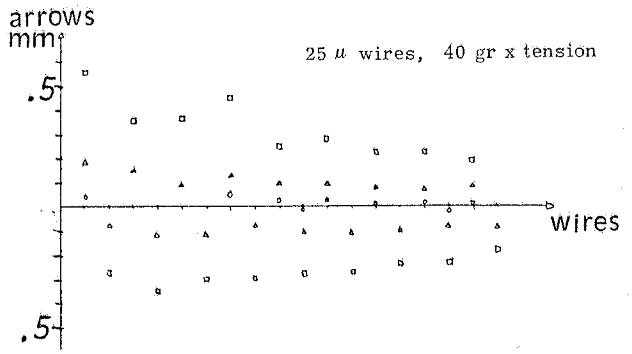

FIG. 83 - Arrows of 25 μ wires in different electric fields :

V_p = - 700 ; V_1 = - 2000 V ;
V_p = - 1400 ; V_1 = - 4000 V ;
V_p = - 2000 ; V_1 = - 6000 V .

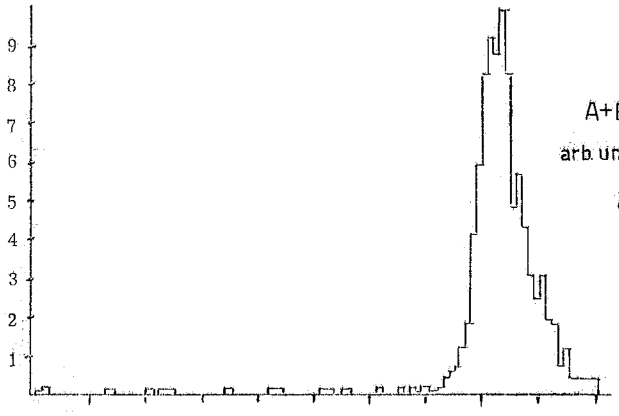

FIG. 84 - Distribution of $Q_1/Q_1 + Q_2$ for a 30 μ wire.

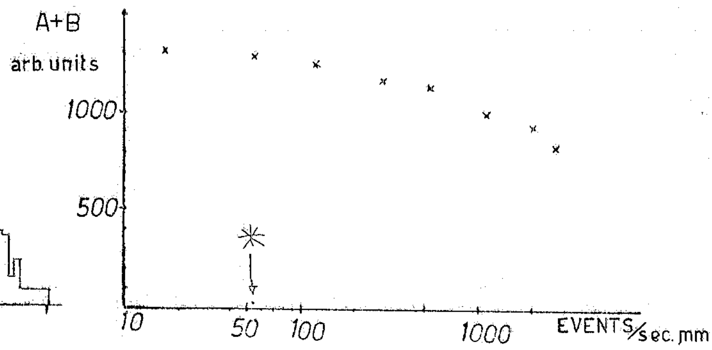

FIG. 85 - Rate test with the beam : the star shows the estimated ISR-rate.

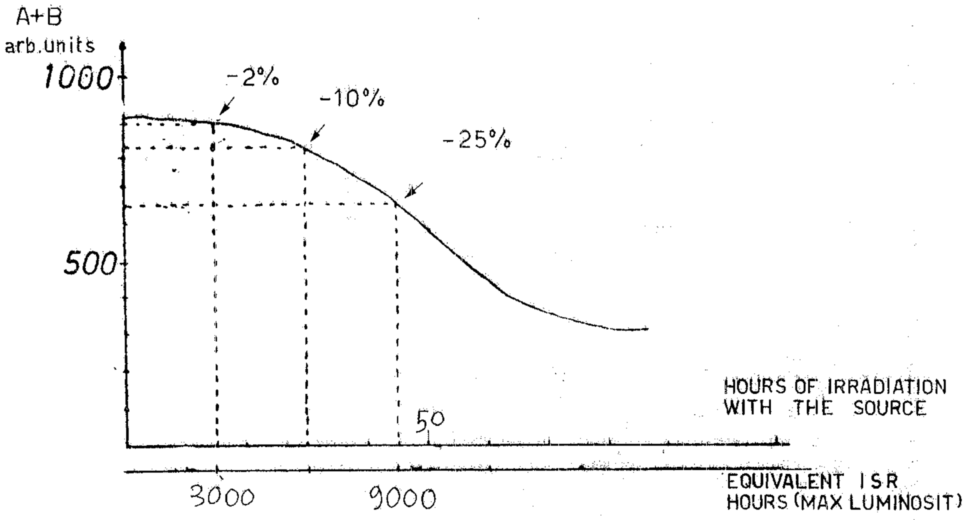

FIG. 86 - Rate test with ^{90}Sr radioactive source.

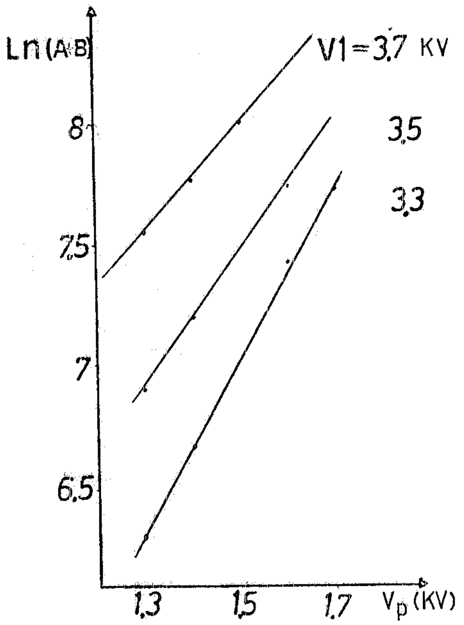

FIG. 87 - Collected charge as a function of the potential.

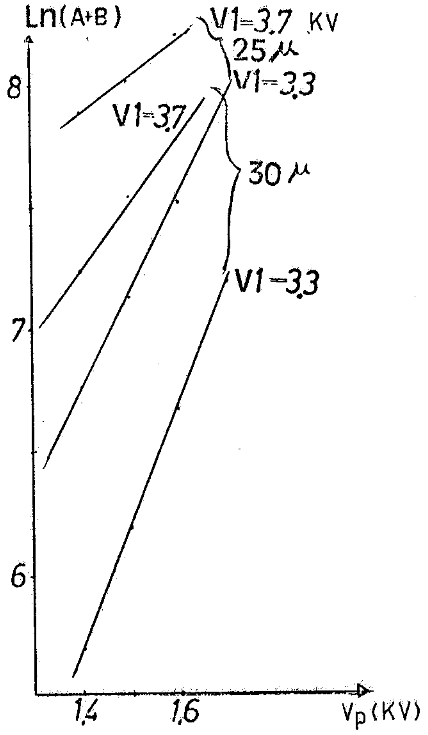

FIG. 88 - Charge collected for 25 and 30 μ wires.

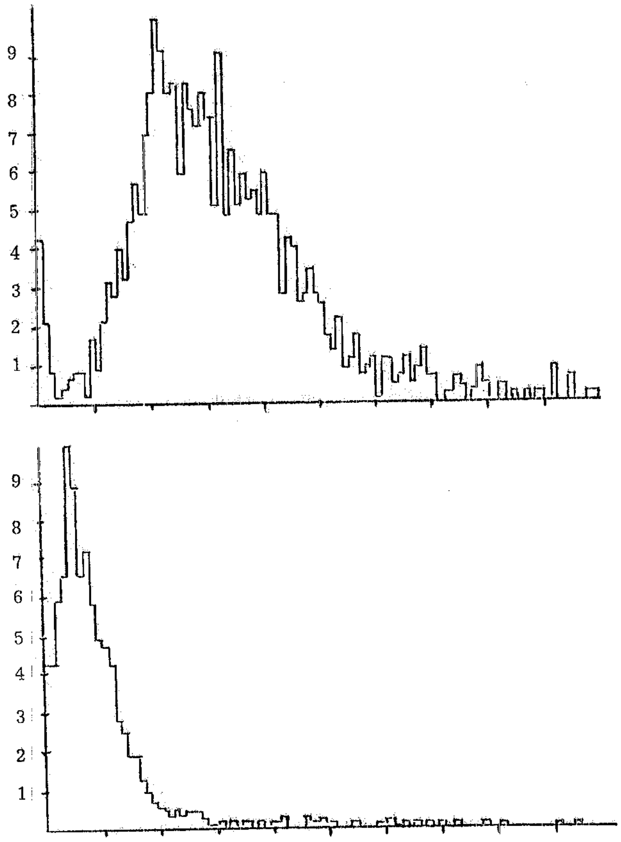

FIG. 89 - Two measurement of A+B for (a) 25 μ wire and (b) a 30 μ wire.

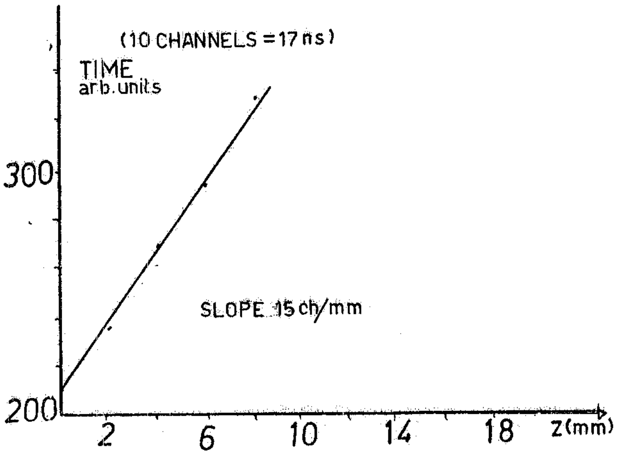

FIG. 90 - Results of the drift time measurement.

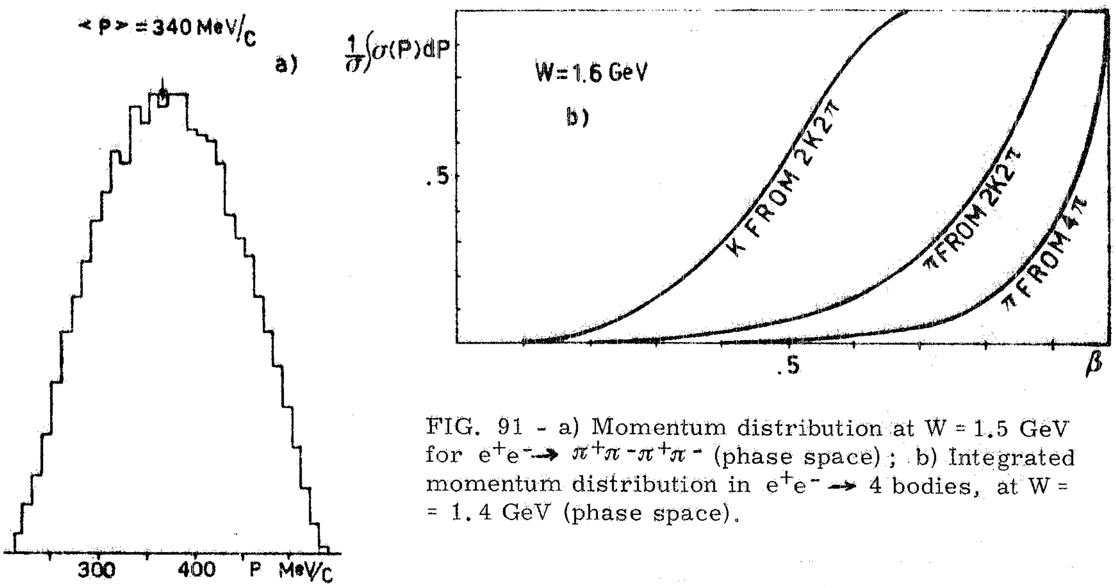

FIG. 91 - a) Momentum distribution at W = 1.5 GeV for $e^+e^- \rightarrow \pi^+\pi^-\pi^+\pi^-$ (phase space) ; b) Integrated momentum distribution in $e^+e^- \rightarrow$ 4 bodies, at W = = 1.4 GeV (phase space).

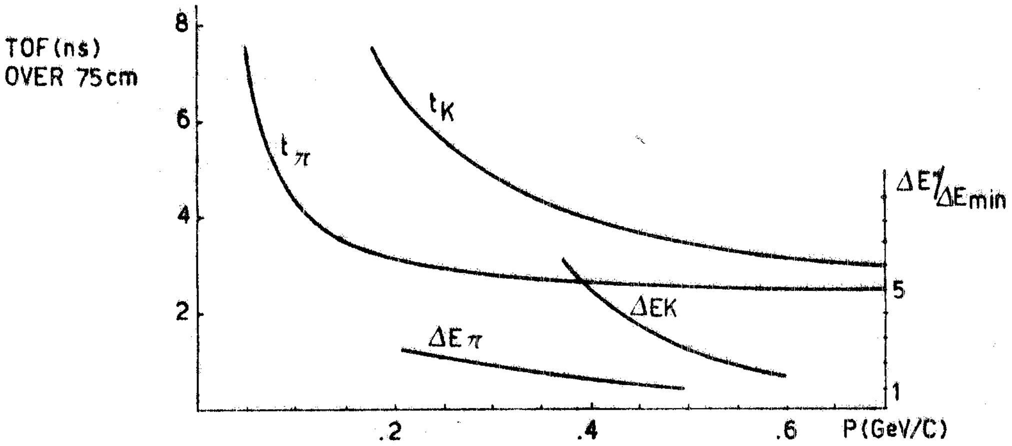

FIG. 92 - TOF vs. momentum for π and K, and energy loss in the TOF counter.

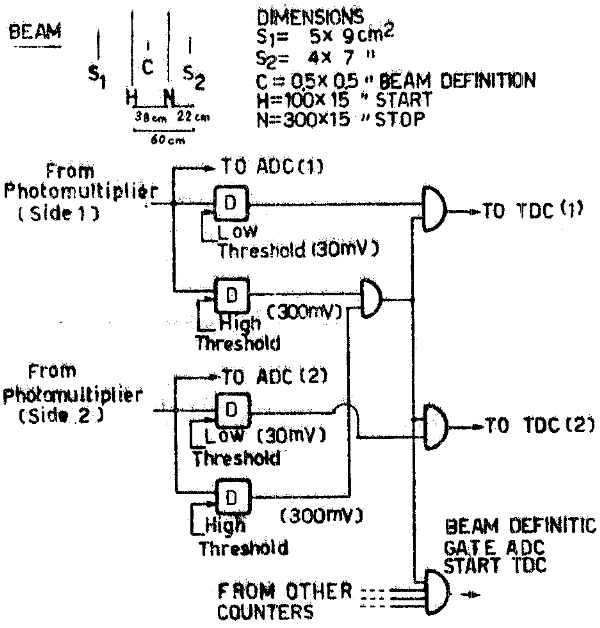

FIG. 93 - Set-up and electronics for the test of TOF at PS (CERN).

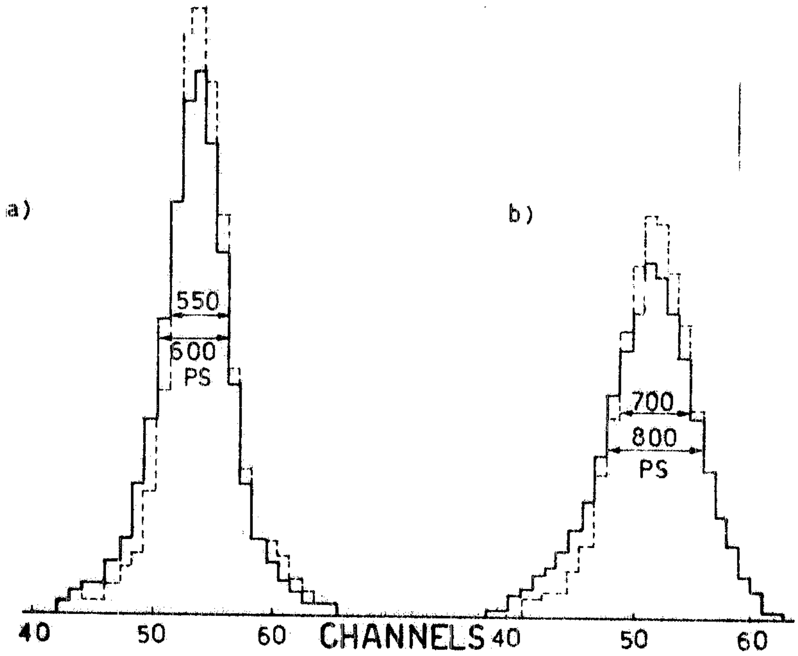

FIG. 94 - TOF distribution in M and N counters :
a) = (H_i - S_2) ; b) = (N - S_2) . The broken lines are the data corrected for pulse height.

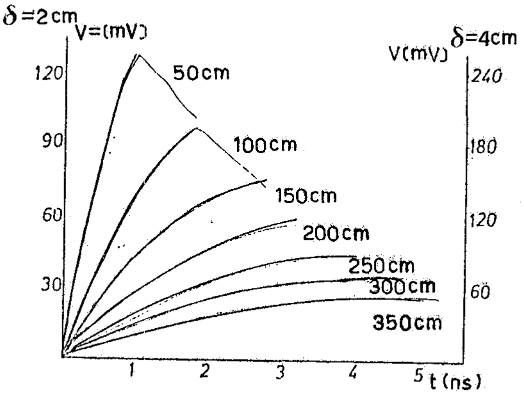

FIG. 95 - The light yield at different distances from the photocathode for two thicknesses (δ = 2, 4 cm) of the plastic scintillator.

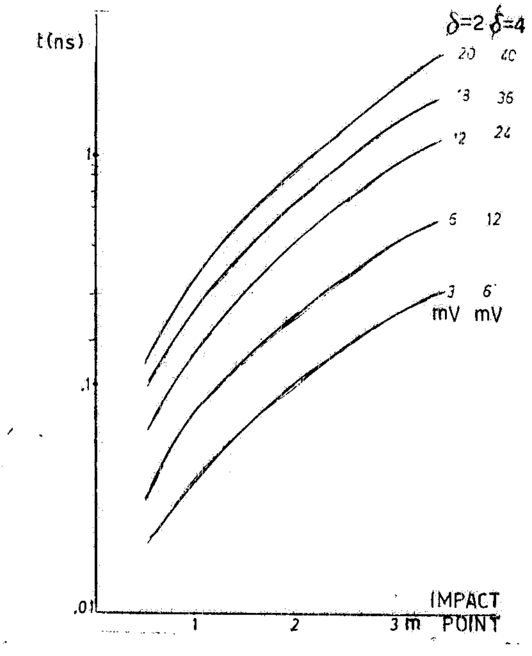

FIG. 96 - Expected time jitter for different impact points with different level of discrimination.

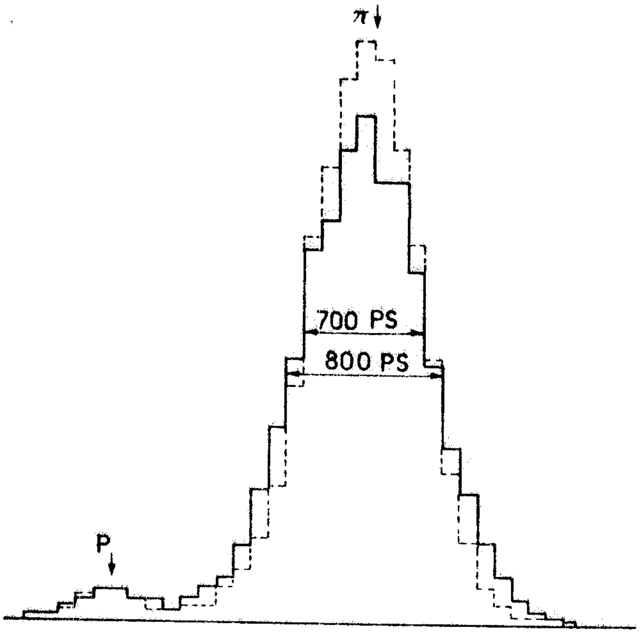

FIG. 97 - (M-N) TOF and p/π discrimination.

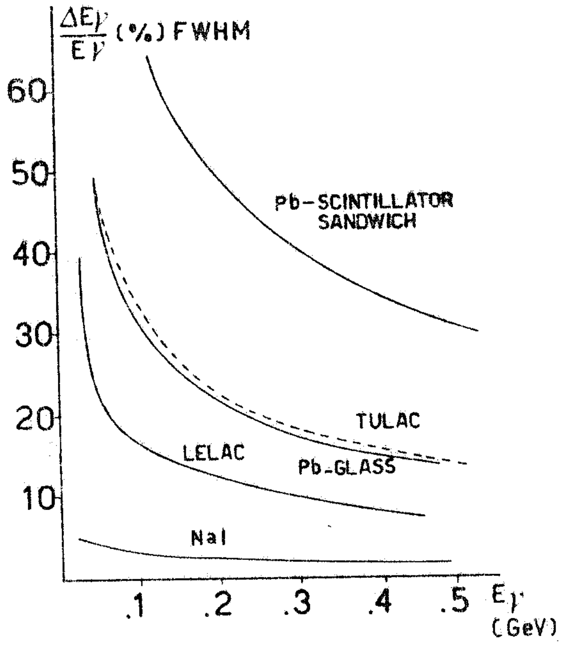

FIG. 98 - Typical resolution of different photon detectors.

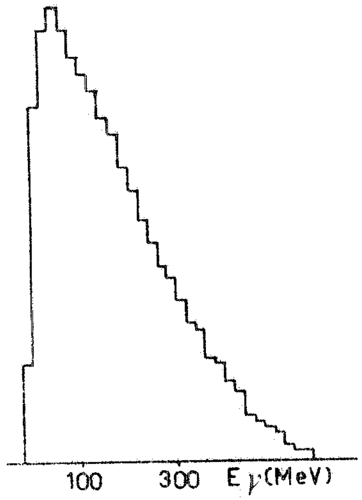

FIG. 99 - Photon momentum distribution in $e^+e^- \rightarrow \pi^+\pi^-\pi^0\pi^0$, at W = 1.5 GeV (phase space).

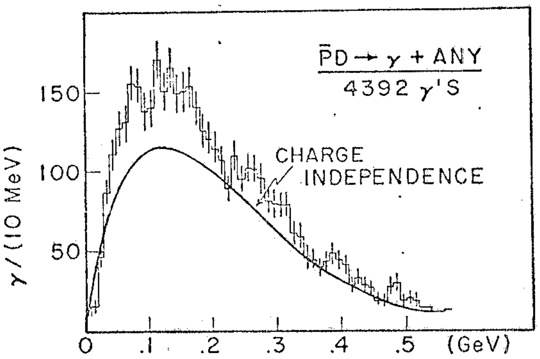

FIG. 100 - The γ energy spectrum from annihilations at rest in deuterium. The γ energy has been obtained by measuring those γ's which coverted in the chamber in the chamber into e^+e^-. This sample is four times greater than the sample reported. The curve shown is the expected spectrum from charge independence obtained from the measured $\pi^{\pm}$ spectrum and normalizing to 3.02/3.77 or the ratio of γ's expected from charge independence over the observed.

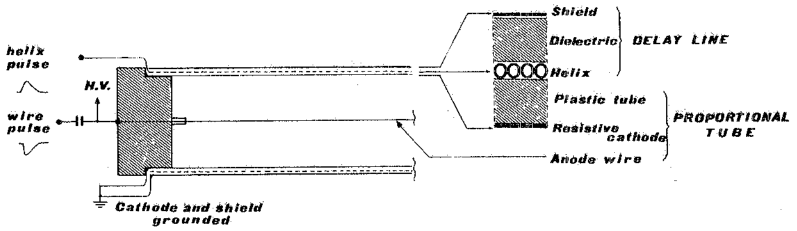

FIG. 101 - Longitudinal cross-section of a proportional tube with resistive cathode and external helical delay line.

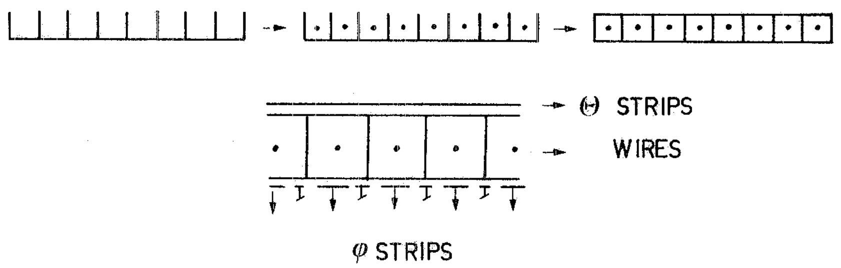

FIG. 102 - Sketch of 8-tube prototype.

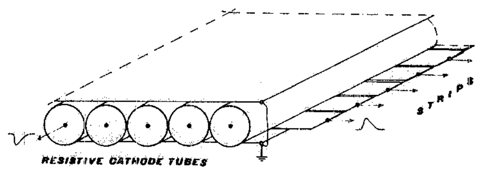

FIG. 103 - Resistive tubes with strips as pick-up electrodes.

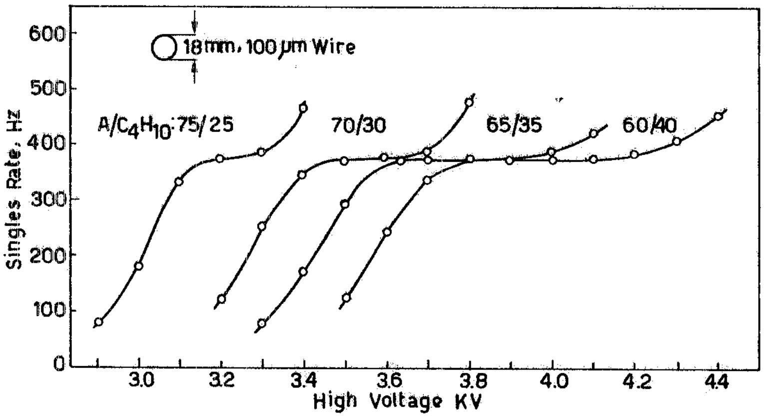

FIG. 104 - Singles rate (Sr^{90} source) vs. H.V. for a tube of the Adone experiment (18 mm diameter, 80 cm length, 100 μm wire) for different concentrations of the argon-isobutane gas mixture. The electronics dead time was 0.5 μs, the threshold 30 mV/50 Ω .

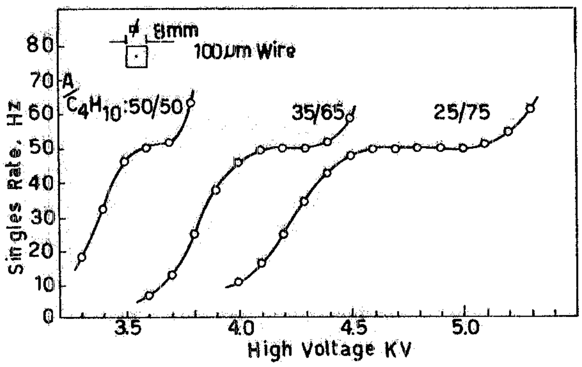

FIG. 105 - Singles rate (Sr^{90} source) vs. H.V. for an 8x8 mm^2. Al tube with a 100 μm sense wire for different concentrations of the argon-isobutane gas mixture. The electronics dead time was 0.5 μs, the threshold 30 mV/50 Ω .

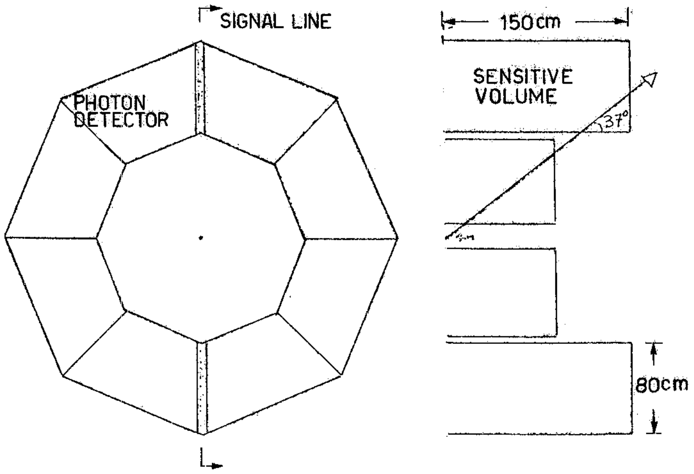

FIG. 106 - Sketch of TULAC;

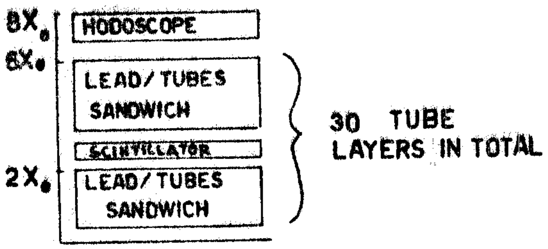

FIG. 107 - Stratigraphy of TULAC.

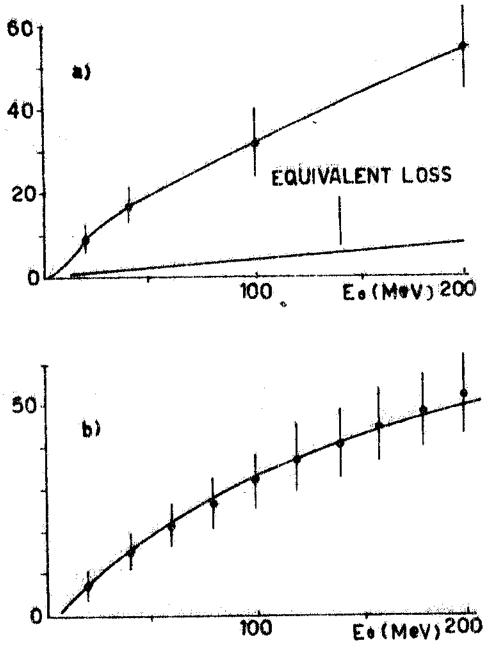

FIG. 109 - Average number of hit tubes, for incident electrons (a) and photons (b).

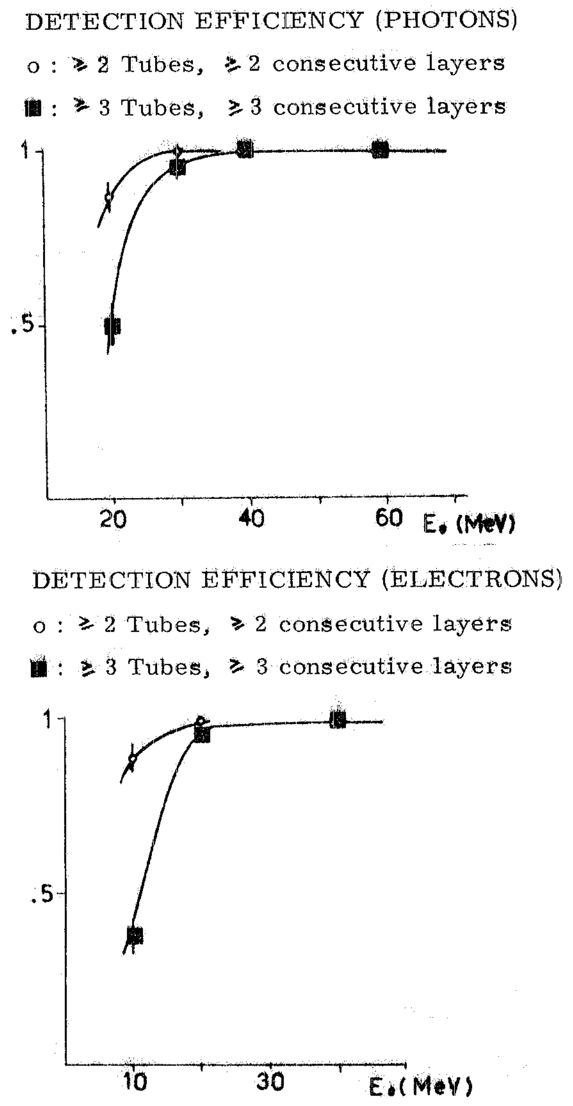
DETECTION EFFICIENCY (PHOTONS)

o : ≥ 2 Tubes, ≥ 2 consecutive layers

■ : ≥ 3 Tubes, ≥ 3 consecutive layers

DETECTION EFFICIENCY (ELECTRONS)

o : ≥ 2 Tubes, ≥ 2 consecutive layers

■ : ≥ 3 Tubes, ≥ 3 consecutive layers

FIG. 108 - Detection efficiency for photons and electrons in a prototype of TULAC.

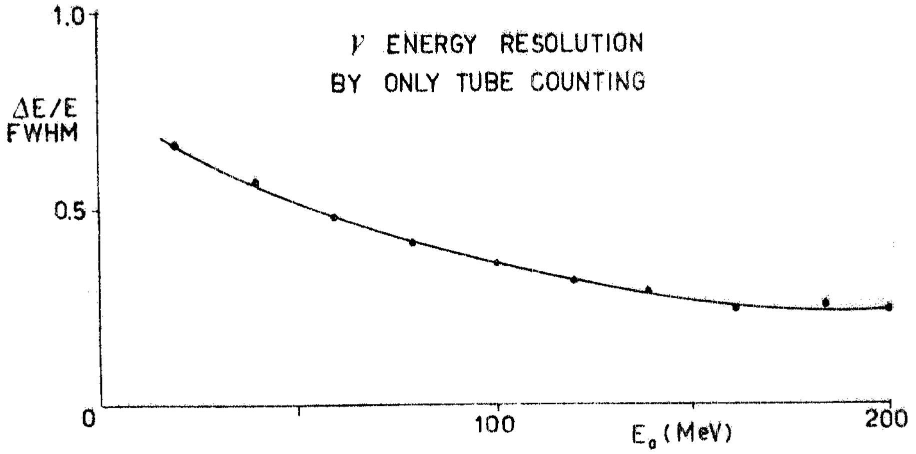

FIG. 110 - Photon energy resolution for different energy.

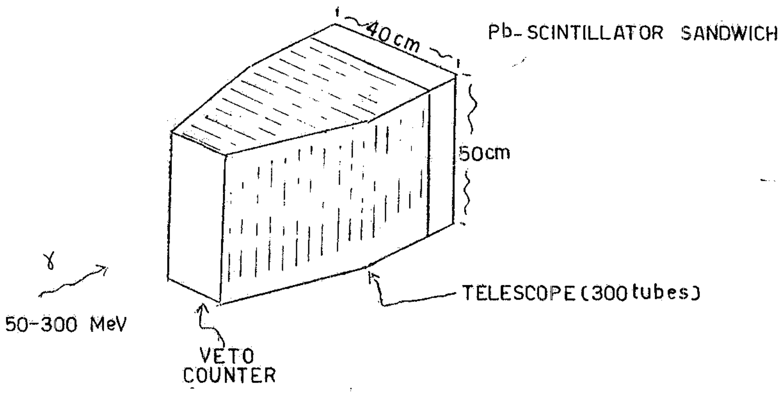

FIG. 111 - Calorimeter prototype.

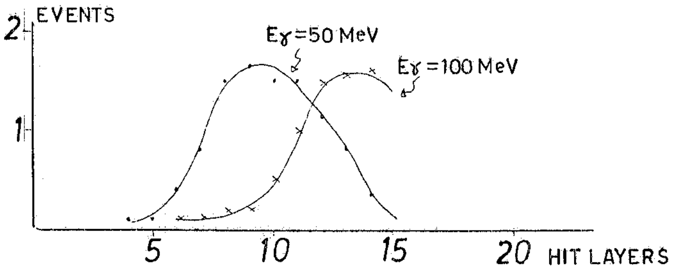

FIG. 112 - Montecarlo calculated event distribution for the TULAC prototype.

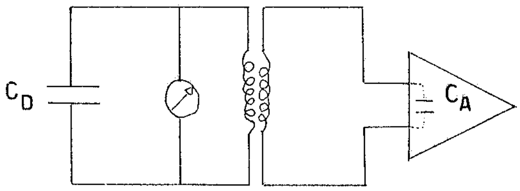

FIG. 113 - Equivalent circuit of one channel of the Ar calorimeter.

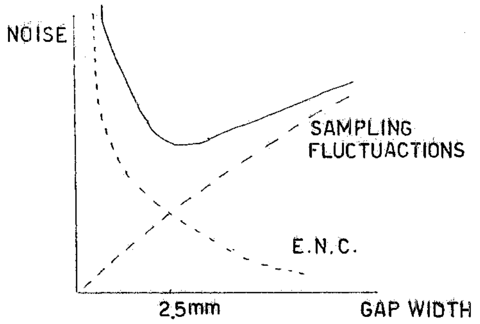

FIG. 114 - Noise as a function of the gap width. The full line is the sum of the two contributions.

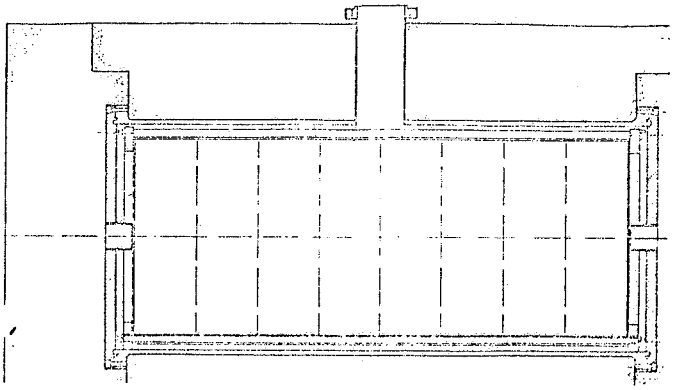

FIG. 115 - LELAC container.

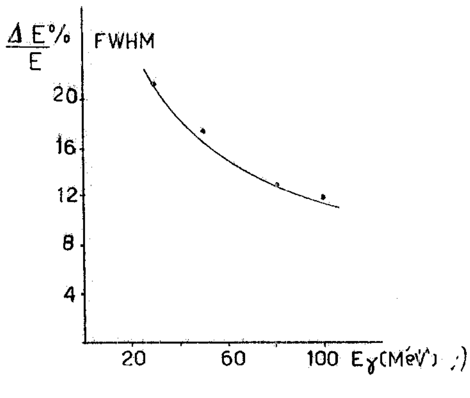

FIG. 116 - LELAC resolution $\Delta E/E$ (Montecarlo calculation).

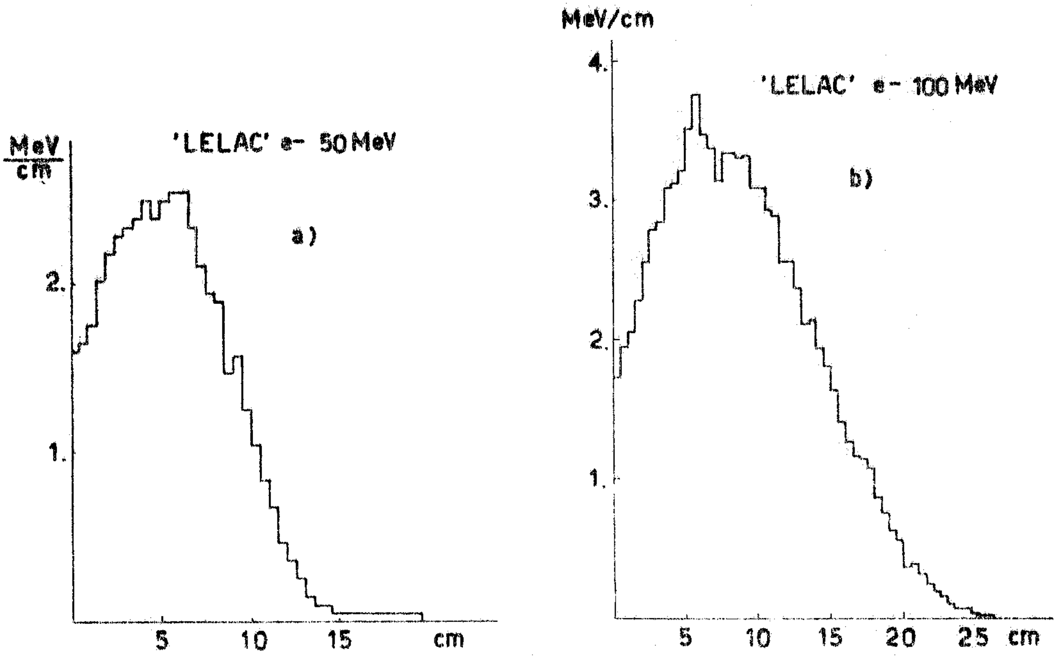

FIG. 117 - Longitudinal development of the cascade for electrons of 50 MeV (a) and 100 MeV (b) (Montecarlo calculation).

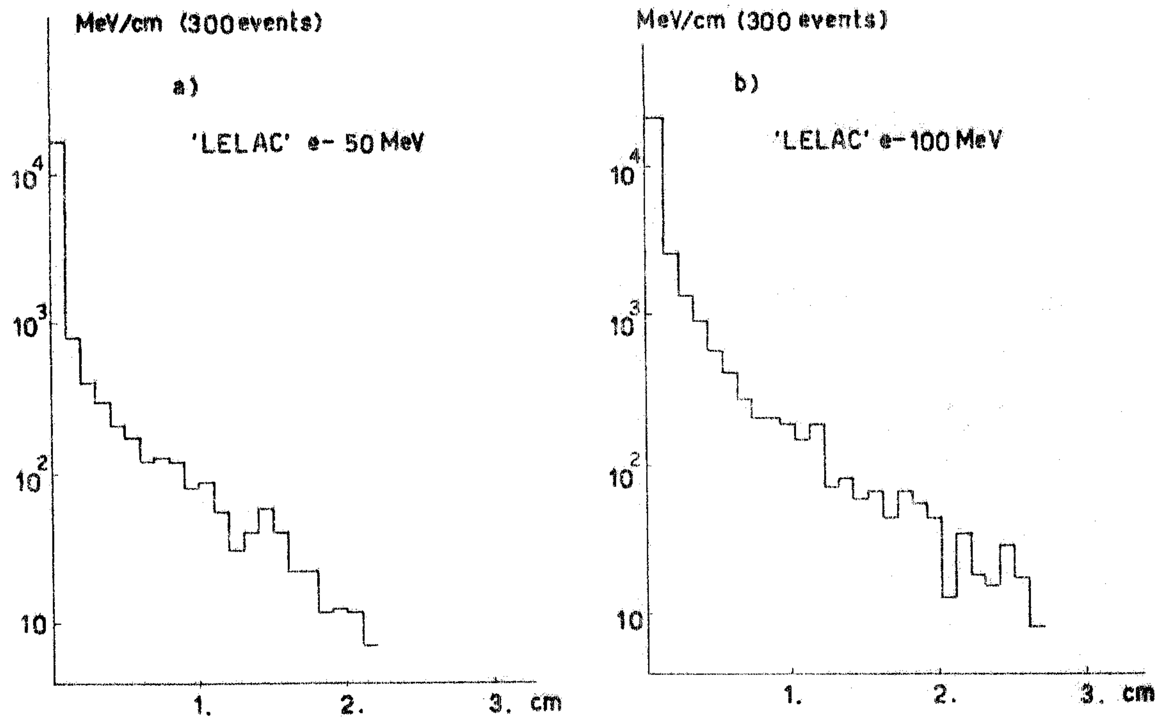

FIG. 118 - Radial development of the cascade for electrons of 50 MeV (a) and of 100 MeV (b) (Montecarlo calculation).

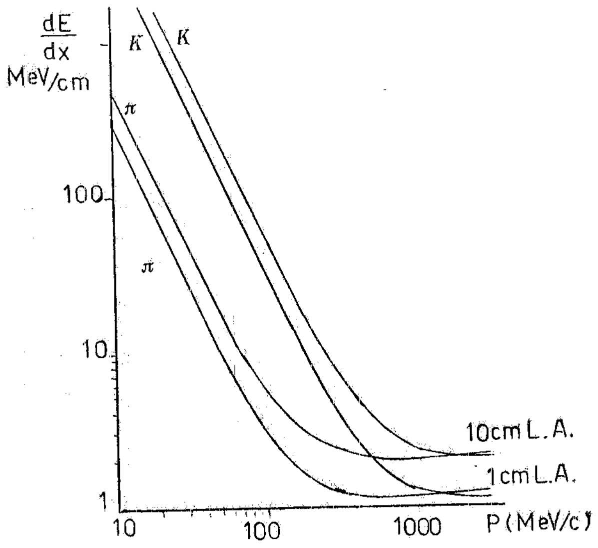

FIG. 119 - dE/dx for π and K in liquid argon, for 1 and 10 cm sampling.

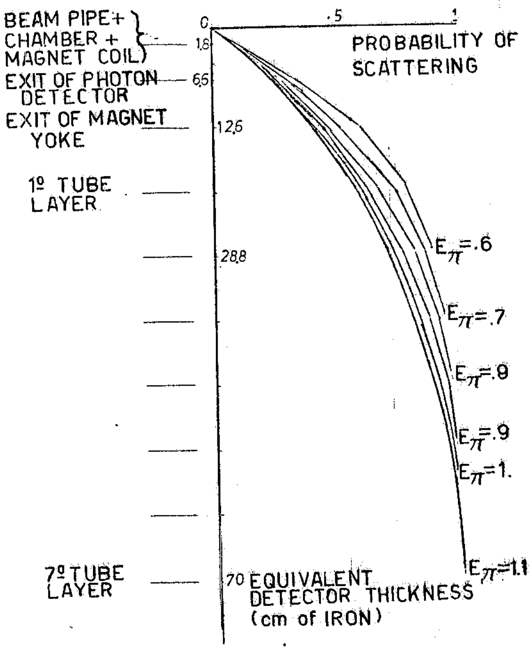

FIG. 120 - Scheme of the μ filter and probability for pions to suffer a large angle ($\theta > 25°$) nuclear scattering.

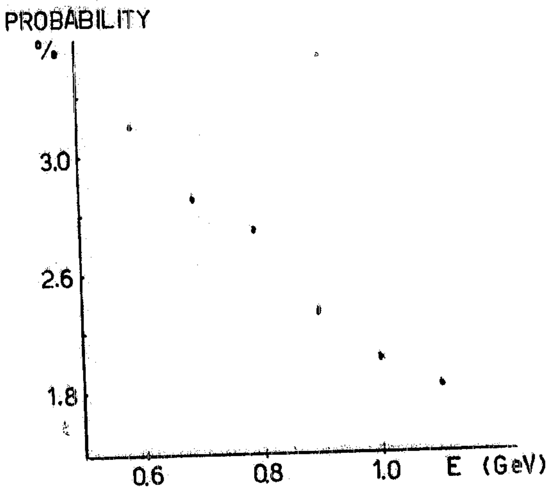

FIG. 121 - Probability (%) for a pion to decay in flight.

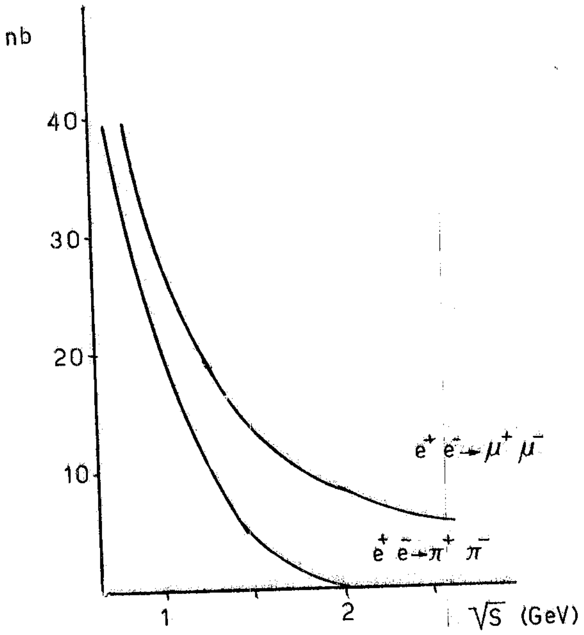

FIG. 122 - Cross sections for $e^+e^- \rightarrow \pi^+\pi^-$ and $e^+e^- \rightarrow \mu^+\mu^-$ (within the acceptance of the μ-filters).

CHAPTER VII - EXPECTED PERFORMANCES OF THE APPARATUS.

VII. 1 - Many body reconstruction.

The capability of to detect a number of typical final states has been studied by G. Paternoster and U. Troya with a Montecarlo calculation. Ten thousand events have been generated at W = 1500 MeV for each of the following final states: $\pi^+\pi^-\pi^0$, $\pi^+\pi^-2\pi^0$, $2\pi^+2\pi^-\pi^0$, $2\pi^+2\pi^-2\pi^0$. An event was accepted by the trigger if at least one charged prong entered the central chambers with $p_\perp > 50$ MeV/c. The p_{ch} resolution assumed was as computed by Montecarlo (Chapter VI, 2,). The space resolution of the photon detector was assumed to be $\sigma_x = \pm 2$ cm (it was checked that the efficiency was sensibly independent of σ_x, as long as $\sigma_x \lesssim 5$ cm). The reference photon energy resolution was taken to be $\sigma = 2 \cdot \sqrt{E}$ (MeV) (corresponding to ~ 50% f. w. h. m. at $E_\gamma = 100$ MeV, with a lower cut $E_{min} = \frac{15}{\sin\vartheta}$ MeV. Out of the events accepted by the trigger, the sample of reconstructe events is defined as those events for which the correct multiplicity is reconstructed. The event multiplicity is derived according to the following rules. If the observed $n_{ch} = 1, 2$ one concludes that $n_{ch}^{true} = 2$ (excepted for a minor correction which is possible when 3 or 4 photons are detected, see below). If $n_{ch} = 3$ or 4, $n_{ch}^{true} = 4$. If no photon is detected, the missing mass MM is worked worked out and $n_{\pi^0} = 1$ is assumed if $m_{\pi^0} - 50\ \text{MeV} \leq \text{MM} \leq m_{\pi^0} + 50$ MeV, $n_{\pi^0} = 0$ otherwise. For one detected γ, $n_{\pi^0} = 1$ if MM = 0 to within $m_{\pi^0} + 50$ MeV, $n_{\pi^0} = 2$ otherwise. For two detected photons, $n_{\pi^0} = 1$ if $m_{\pi^0} - 50\ \text{MeV} \leq \text{MM} \leq m_{\pi^0} + 50$ MeV and $n_{\pi^0} = 2$ otherwise. For 3 or 4 detected photons, $n_{\pi^0} = 2$. In addition, for events with two observed prongs, the photon combinations consistent with the π^0-mass are searched for, and the π^0-mass is attributed them and the overall missing mass of the event is computed. If this is inconsistent with zero (50 MeV tolerance for 4 γ's, m_{π^0} +50 MeV for 3 detected γ's), one assumes $n_{ch} = 4$. The results of the computation are shown in Table VII.

TABLE VII - Reconstruction efficiency with $\sigma_{E_\gamma} = 2\sqrt{E}$

$\pi^+\pi^-\pi^0$	88%	trigger efficiency =	97%
$\pi^+\pi^-\pi^0\pi^0$	78%		98%
$\pi^+\pi^-\pi^+\pi^-$	90%		100%
$\pi^+\pi^-\pi^+\pi^-\pi^0$	80%		100%
$\pi^+\pi^-\pi^+\pi^-\pi^0\pi^0$	94%		100%

The dependence of reconstruction efficiency on energy resolution of the photon detector is shown in fig. 123. It is seen that in all channel the efficiency can only be increased by a few percents by improving the resolution. It should be observed, however, that the merit of energy resolution has to be found in the possibility of measuring directly reactions with single monocromatic photons. Moreover, since these reactions are likely to have quite small cross-sections, any leakage from misidentified events of large cross-section would contribute a relatively large background. An example of such a situation is mentioned in the following paragraph.

VII. 2. - Photon-photon processes.

In addition to one-photon annihilation, the two-photon process $e^+e^- \rightarrow e^+e^- \underbrace{\gamma\gamma}_{\hookrightarrow X}$ (56) gives rise to particle production as shown schematically

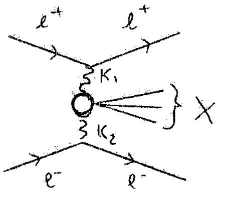

The produced mass m_x ($m_x = \sqrt{s}$ of the photon-photon system) is $m_x^2 = 4 k_1 k_2$, where k_1, k_2 are the three-momenta of the quasi-real photons. In the laboratory frame, X has a momentum which is in general different from zero, with components $k_\perp = k_{\perp,1} + k_{\perp,2}$ and $k_\parallel \simeq k_1 - k_2$. This process has been observed in the past both at Novosibirsk and at Adone (57). A Frascati experiment made use of special tagging counters of the final state electrons. R. Del Fabbro and G. P. Murtas have studied the possibility of performing $\gamma\gamma$ physics at ALA.

The two colliding electrons of energy E radiate quasi-real photons within a typical angle $\sqrt{m_e/E}$ $\sim$ 20 mr and produce a state X of mass m_x with cross-section (58)

$$\sigma_{ee \to X} \simeq 2 \left(\frac{\alpha}{\pi}\right)^2 \ln^2 \left(\frac{E}{m_e}\right) \int_0^{4E^2} \frac{dr}{r} \, F(x) \; \sigma_{\gamma\gamma \to X}(s)$$

where $F(x) = (2 + x^2)^2 \; \mathrm{Ln} \, \frac{1}{x} - (1 - x^2) \; (3 + x^2)$ and $x = \frac{\sqrt{s}}{2E}$ is the relative energy of the system. Integration of this formula gives

$$\sigma_{\gamma\gamma \to X} = \frac{\alpha^4}{m_X^2} \ln^2 (E/m_e)$$

Since this cross-section grows at high energy (for fixed Mx) one expects this effect to be more important at the large e^+e^- machines. Even at ALA/MDA, however, one can estimate that the rate of a number of processes in which low mass-states are produced is not negligible. We show in fig. 124 the two-photon cross-sections for μ-pair and π-pair production (58), where one sees that they become comparable to the annihilation cross-sections at the ALA energies. Since the X-state produced as $\gamma\gamma \to X$ must be $J^C = 0^+, 2^+$, it is interesting to consider the production of the lightest meson resonances with these quantum numbers, i. e. π^0, η (550), η' (960). In particular, η' production is interesting as a means for measuring the $\eta \to \gamma\gamma$ coupling constant. The estimated rate of η' and η production (using the experimental $\gamma\gamma$ coupling = 0,85 KeV for η, and the existing upper limit $\Gamma_{e^+e^-} = 20$ keV for η') is given in fig. 125, for an integrated luminosity of 2.6×10^4 nb^{-1} (30 full days at 10^{31} cm^{-2} s^{-1} luminosity).

The detection probability in MDA for $\gamma\gamma \to \eta$ and $\gamma\gamma \to \eta'$ has been computed with a Montecarlo program (taking into account the geometrical cuts only) for the dominant branching ratios

$$\eta \to \gamma\gamma \; , \; \pi^+\pi^-\pi^0 , \; \pi^0\pi^0\pi^0 \qquad \eta' \to \eta \, \pi^+\pi^- , \; \eta \, \pi^0\pi^0 , \; \gamma \, \pi^+\pi^-$$

for three different cases: a) all final state particles detected, b) one particle missed, c) more than one particle missed (in practice, these events are lost). The results are shown in Table VIII for different beam energies. One sees, for example, that at the top ALA energy about 30% of the η' decays are fully accepted in the detector. This corresponds to $\sim$ 8000 events in the above-mentioned integrated luminosity (fig. 125).

In general, the experimental signature for $\gamma\gamma$-production should be found either in associated final state electrons or in the small observed energy inside the main detector. Although an efficient tagging is probably essential, it will also be important to exploit the available energy signature. How well this will be done will depend on the energy resolution of the charged as well as of the neutral component. With reference to the study of a particular resonance like the η', an addition signature can be found in the total effective mass (which is different from the observed energy, since the X-laboratory momentum is in general $\neq 0$). In the η' case the $\gamma\pi^+\pi^-$ decay, which contributes about 50% of the fully accepted events (see Table VIII), is a good candidate to provide a peak in the effective mass spectrum.

A reaction of interest at ALA is also $e^+e^- \to e^+e^- \; \pi^+\pi^-$ whose cross-section can be estimated in the approximation of point-like pions. $\pi\pi$ resonance (like the σ) can give additional contribution in this channel (58). However, at W = 2.4 GeV, the expected total yeld is only $\sim$ 500 events for $\int L \, dt = 2,6 \times 10^4$ nb^{-1}. Moreover, a large fraction of events is expected to be lost in the dead cones of the experiment at small angles, since the differential cross-section is forward-peaked (in particular in the laboratory, because of the longitudinal motion of the $\pi\pi$ system). We therefore have little hope to collect a significant amount of data in this channel. The most clear-cut signature for two-photon reaction would be the observation of at least one of the final state electrons. The feasibility of this has been studied for ALA/MDA by R. Del Fabbro. We show in fig. 126 the magnetic elements of ALA down-stream of the intersection point. Q_D, Q_F are defocusing and focusing

TABLE VIII - The probabilities of detecting various decay modes of the and ' are given for different conditions of detection (see text).

DECAY			E=.8GeV			E=1			E=1.1			E=1.2			E=1.3			E=1.5		
			a	b	c	a	b	c	a	b	c	a	b	c	a	b	c	a	b	c
η	$\gamma\gamma$		48	35	17	43	42	15	43	44	13	46	42	12	50	37	13	58	26	16
	$\pi^+\pi^-\pi^0$		26	47	27	22	42	36	21	42	37	22	44	34	24	45	31	31	49	20
	$3\pi^0$		8	30	62	6	24	70	6	24	70	7	25	68	8	27	65	9	33	58
η'	$\eta\pi^+\pi^-$	$\eta\to\gamma\gamma$	8.6	6.1	3.6	7.3	6.6	4.2	7.5	7.2	4.0	5.7	8.0	4.8	6.4	7.1	5.3	6.2	8.0	4.9
		$\eta\to\pi^+\pi^-\pi^0$	5.2	7.0	3.8	3.1	6.7	4.7	3.4	6.3	5.2	2.7	6.3	6.1	3.0	5.5	5.7	2.7	5.4	6.3
		$\eta\to3\pi^0$	1.1	3.2	6.9	1.1	2.8	7.6	.7	3.0	7.3	.7	2.1	8.5	.6	2.4	7.8	.6	2.5	8.5
	$\eta\pi^0\pi^0$	$\eta\to\gamma\gamma$	3.7	3.4	2.5	3.0	4.3	3.0	3.3	3.8	3.1	2.6	4.1	3.4	2.7	3.7	3.6	3.2	3.8	3.4
		$\eta\to\pi^+\pi^-\pi^0$	1.9	3.4	2.3	1.0	2.8	3.6	1.2	2.9	3.6	1.1	2.9	3.5	1.2	2.8	3.9	1.1	2.4	3.9
		$\eta\to3\pi^0$	.5	1.7	4.2	.5	.1	5.1	.7	1.3	4.3	.2	1.4	4.7	.2	1.3	4.2	.3	1.3	4.7
	$\gamma\pi^+\pi^-$		19.3	3.8	3.0	17.8	11.1	2.8	16.6	11.2	3.5	16.0	12.2	3.2	16.7	12.3	3.1	15.6	11.6	3.2

quadrupoles in the horizontal plane. Since the electrons are emitted at small angles (~ 50% at $\vartheta < \sqrt{\frac{m_e}{E}}$) they cannot be seen in the main detector, but they could be observed by suitable counters or chamber when they exit the pipe after crossing a number of magnetic elements. The actual orbits depend in a complicated way on electron energy and scattering angle. Such orbits have been computed in a number of cases. The result is shown in a particular case in fig. 127 (upper plot, scattering angles ϑ = 20 mr, $\varphi = \pi$; lower plot, ϑ = 20 mr, φ = 0), for four values of the relative energy retained by the electrons. For larger scattering angles the exit point is in general nearer to the entrance of the first quadrupole and the opposite is true for smaller scattering angles.

The relationship between point of exit from the pipe and electron momentum is not unique and therefore one cannot in any realistic way measure the momentum of these electrons. However, it is possible signal them with a system of counters sorrounding the beam pipes. With a limited coverage (a couple of meters on each side) one finds that this can be done with an efficiency ~ 50% for detecting both electrons. This would be enough to save an appreciable rate for reactions like η , η' production. Only on the basis of practical experience it will be possible to state whether with this method one will be able to achieve a sufficient improvement of the signal/background ratio for studies of γ γ reaction. It should be observed that a very dangerous background is contributed from not-reconstructed annihilation events. With the aid of the Montecarlo calculation mentioned in the previous paragraph, the apparent cross-section at W = 1500 MeV for a number of topologies of such events have been computed. The production cross-section have been used as measured at Adone. The results are shown in Table IX and compaired with the cross-sections of the same topologies from 2π , η and η' production as discussed above. It is seen that the expectal rates are roughly the same. A separation of γ γ events from this background can only came from flags of accompanying inelastic electrons and from visible energy measurement (lower energy being in general associated to γ γ events). Of course, it would also help to performe a more complete reconstruction of the events (for instance, by implementing the detector at small angles).

TABLE IX - Cross-sections detected for not-reconstructed one photon events (nb).

Exp. Chan.	$\pi^+\pi^-\pi^0$	$\pi^+\pi^-\pi^0\pi^0$	$2\pi^+2\pi^-\pi$	$2\pi^+2\pi^-2\pi^0$	TOT.	2 PHOTON CROSS SECTION
2ch + One	.001	.12	.035	.006	.162	3. nb
2 + 1	.002	.65	.2	.06	.912	.6
2 + 2		.77	.23	.23	1.23	.64
2 + 3		.91		.5	1.4	.12
2 + 4		.005		.33	.33	.66
4 + 1			.14	.16	.3	.3

VII. 3. - An unconventional perspective: the search for quark-imps.

A search for fractional charge quarks would be highly interesting at ALA/MDA, since no real good measurement was done until now at e^+e^- machines. Although an effort in this direction will certainly be made, one must realize that the detection method requires accurate repeated $\frac{dE}{dx}$ measurements. $\frac{dE}{dx}$ information will be provided by the TOF counters, whose resolution will however be rather limited resolution since they are quite long. As mentioned at the end of Chapter VI, 2, the central chambers are not likely to produce accurate $\frac{dE}{dx}$ information. Further $\frac{dE}{dx}$ information might eventually come from the photon detector, whose resolution cannot be specified yet. All in all, a quark search based on $\frac{dE}{dx}$ is likely to be vary difficult. The situation will be less difficult if quarks have integer charge (and mass different from any known particle), as expected in the Pati-Salam model (Chapter V), and relatively long lifetime.

Surprisingly enough, the problem might be easier if quarks have short apparent lifetime, as the imps which were mentioned in Chapter V. G. Bellettini and T.T.Wu have studied how these particles could possibly be signaled in MDA. We consider the two following production processes 1) $e^+e^- \rightarrow q + \bar{q}$, 2) $e^+e^- \longrightarrow \pi^+ + \bar{u} + d$ (quark charges $-\frac{2}{3}$ e, $-\frac{1}{3}$ e). Both reactions would be detectable in an upgrated detector, as shown in fig. 128. Two small planar drift chambers have been added immediately above and below the elliptical beam pipe to extend the tracking to smaller distancies, while a double layer of resistive tubes detects the hadrons (the imps) interacting in the magnet yoke. Reaction 1) would be signaled by two (low ionizing) tracks produced back to back, disappearing after a while in the cylindrical chambers, but still interacting in the magnet yoke and even more at a position indicating that bending has continued after disappearence. For charges $\pm \frac{1}{3}$ e, m_q = 500 MeV, W = 2 MeV the expected displacement with respect to a straight line is ~ 15 mm on the magnet coil and ~ 46 mm on the yoke. The interaction probability in the yoke is ~ 40% if the cross-section has normal hdronic values. The detection efficiency would be ~ 10% and ~ 4% for one and two interacting imps respectively. Reaction 2), one will have different observed configurations depending on the direction of the final state particles and on the track length of the imps. Even if only the π^+ is tracked in the chambers, the accompanying two hits (~ 1% probability) or one hit (~ 15% probability) in the hadron detector will provide powerful signature (notice that these cannot be attributed to photons, that would be absorved in the photon detectors in front). Moreover, these events would apparently not conserve the charge. This signature, however, would be of greater weight if forward and background track measuring devices are installed at $\vartheta < 30°$ (see fig. 75), to reduce the number of misindefied normal events.

To give an idea of the level of sensitivity of such a measurement on inclusive imp production cross section one can argue as follows. We guess that for imps of charge $\frac{1}{3}$ e $\sigma(e^+e^- \rightarrow q + x)$ $\frac{3}{9}$ $\sigma_{\mu\mu} \cdot \varepsilon$ where the factor 3 accounts for two quarks produced in $e^+e^- \xrightarrow{3} q\bar{q}$ and for some more production in many body channels, and ε is a suppression factor due to interactions in the final state. Therefore

$$\sigma(e^+e^- \longrightarrow \text{imp} + x) \sim 7 \times 10^{-33} \cdot \varepsilon \quad \text{cm}^2 \text{ at } W = 2 \text{ GeV}.$$

With a solid angle of the hadron detectors of ~ 25% the rate of single interacting imps at ALA can be estimate as $R \sim 10^{-2} \cdot \varepsilon \ s^{-1}$.

Therefore, even if ε is as smaller as $\sim 10^{-3}$ one would get approximately one event/day. This can be considered the ultimate sensitivity of the measurement.

- Conclusions.

The intriguing experimental situation, the fascinating teoretical expectations and the high quality of the machine/experiment that can be designed nowdays anticipate a scientific success for the ALA/MDA project.

ACKNOLEDGEMENTS.

I am pleased to acknowledge the invaluable help and advice received by my Thesis Adviser, Prof. Giorgio Bellettini.

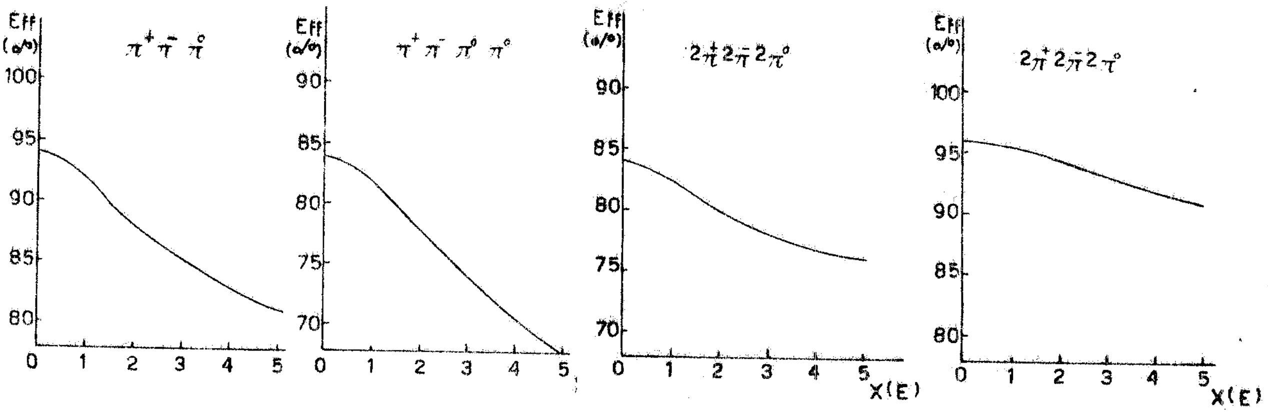

FIG. 123 - Photon energy resolution.

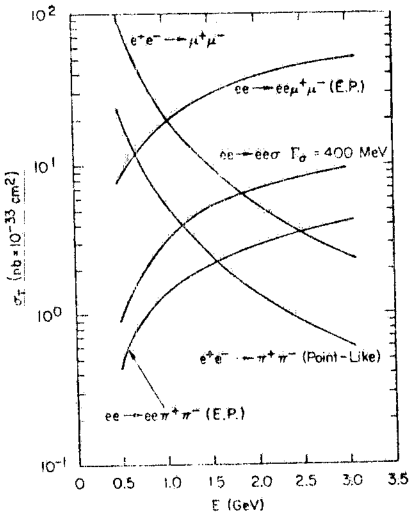

FIG. 124 - Expected values of a number of one and two photon cross section.

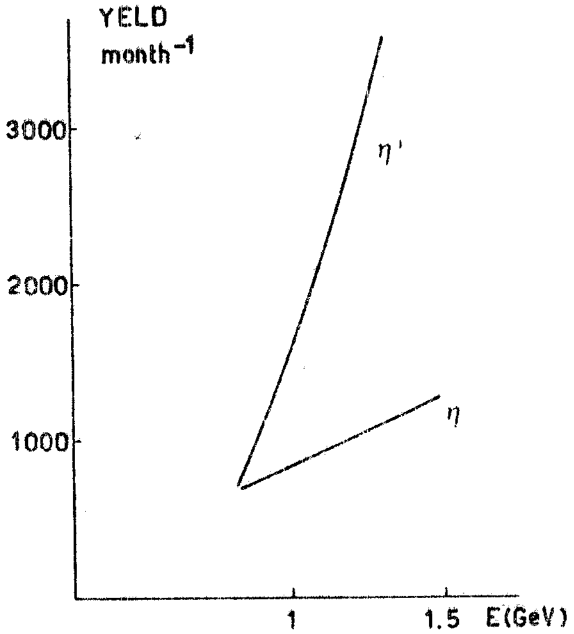

FIG. 125 - The yield of η and η' production corresponding to the total cross section for our standard integrated luminosity (2.6×10^4 nb^{-1}).

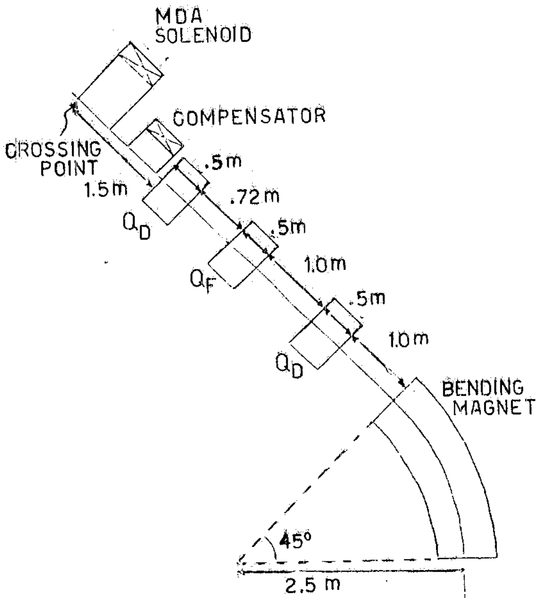

FIG. 126 - Horizontal view of a half straight section where MDA and compensator solenoids are represented; a partial view ol ALA-6 optical structure is also shown. Longitudinal dimensions are indicated.

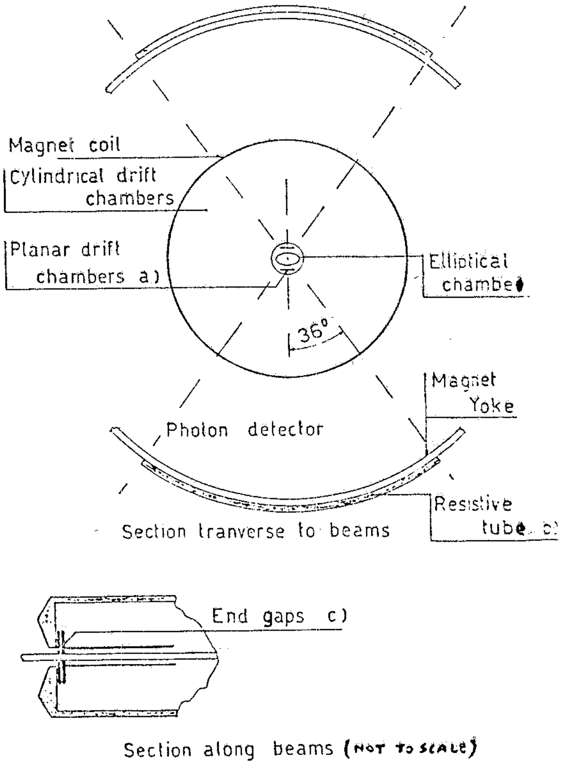

FIG. 128 - Implementations of MDA (a+b+c) for the quark-imp search.

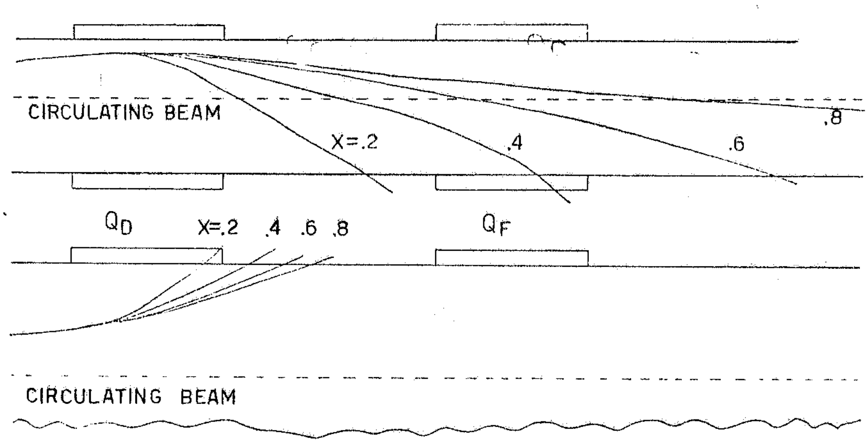

FIG. 127 - Electron trajectories in the radial (down) and vertical (up) view at different electron energies (x = 0.2, 0.4, 0.6, 0.8) and at same polar and azimuthal angle (θ = 20 mrad, ϕ = 0, $\phi = \pi/2$).

REFERENCES

(1) - The great amount of experimental and theoretical work on J/ψ physics has originated from the primary discoveries, reported in Phys. Rev. Letters 33, 1404, 1406, 1408 (1974).

(2) - The new physics for the heavier b-quark has originated from the discoveries, reported in Phys Rev. Letters 39, 252 (1977).

(3) - Adone Status Report, Frascati Report LNF-71/7 (1971).

(4) - These experiments ended around 1972. For a review of the data see for instance: C. Bernardini, Results in e^+e^- Reaction at Adone, Proceedings of th Electron-Photon Symposium, Cornell (1971), p. 38.

(5) - C. Bemporad, Proceedings of the 1977 Intern. Symp. on Lepton and Photon Interactions at High Energies, Hamburg (1977), p. 165.

(6) - C. Bacci et al., Phys. Letters 64B, 356 (1976).

(7) - W. W. Ash et al., Lett. Nuovo Cimento 11, 705 (1974).

(8) - M. Ambrosio et al., Phys. Rev. Letters 68B, 397 (1977)

(9) - For the search of narrow resonancies see for example: B. Bartoli et al., Frascati Report LNF-75/40 (1975), and C. Bacci et al., Frascati Report LNF-78/29 (1978), to be published in Phys. Letters.

(10) - G. P. Murtas, Frascati Report LNF-78/40 (1978), presented at the XIX Intern. Conf. on High Energy Physics, Tokyo (1978).

(11) - M. Bernardini et al., Nuovo Cimento 17A, 383 (1973); A. Zichichi, Riv. Nuovo Cimento 4, 498 (1974).

(12) - J. M. Feller et al., Phys. Rev. Letters 40, 1677 (1978).

(13) - C. Bacci et al., Frascati Report LNF-77/33 (1977); Phys. Letters 71B, 227 (1977).

(14) - M. Bernardini et al., Phys. Letters 45B, 510 (1973).

(15) - Status Report on DCI, Orsay Technical Report 2-77 (1977), presented at the X Intern. Conf. on High Energy Accelerators, Serpukhov (1977).

(16) - F. Laplanche, Recent Results from DCI, Proceedings of the 1977 Intern. Symp. on Lepton and Photon Interactions at High Energy, Hamburg (1977), p. 189.

(17) - G. J. Feldman, Speaker of e^+e^- Reactions at the XIX Intern. Conf. on High Energy Physics, Tokyo (1978).

(18) - S. Bartalucci et al., Frascati Report LNF-77/1 (1977); Nuovo Cimento 39A, 374 (1977).

(19) - Proceedings of the Topical Meeting on e^+e^- Annihilation at Medium Energies, Frascati (1978), p. 29.

(20) - E. Gabathuler, Rapporteur talk at the XIX Intern. Conf. on High Energy Physics, Tokyo (1978).

(21) - A. S. Carroll et al., Phys. Rev. Letters 32, 247 (1974).

(22) - V. Chaloupka et al., Phys. Letters 61B, 487 (1976).

(23) - R. L. Kelly and R. J. N. Phillips, Report RL 76-053 T159/LBL-4879 (1976).

(24) - L. Montanet, Report CERN/EP/Physics 77-22 (1977), Proceedings of the V Intern. Conf. on Experimental Mesons Spectroscopy, Boston (1977), p. 260.

(25) - A. A. Carter et al., Phys. Letters 67B, 117 (1977).

(26) - P. Benkheiri et al., Phys. Letters 68B, 483 (1977).

(27) - T. Armstrong, quoted in ref. (24).

(28) - Ch. Defoix et al., Collège de France, Report LPC 76-08 (1976).

(29) - P. Pavlopoulos et al., Phys. Letters 72B, 415 (1978).

(30) - U. Gastaldi, $\bar{p}p$ Experiments at very Low Energy using Cooled Antiprotons at CERN, Proc. of the IV European Antirpoton Symp., Barr (1978); P. Dalpiaz et al., e^+e^- Pairs Produced in $\bar{p}p$ Annihilation, same symposium.

(31) - G. Bassompierre et al., Phys. Letters 68B, 477 (1977).

(32) - M. Bohm et al., Nuclear Phys. B51, 397 (1973).

(33) - A. Bramon and M. Greco, Lett. Nuovo Cimento 3, 693 (1972).

(34) - J. A. Shapiro, Phys. Rev. 179, 1345 (1969).

(35) - M. Greco, Phys. Letters 70B, 441 (1977); Frascati Report LNF-76/55 (1976).

(36) - A. D. Bukin et al., Phys. Letters 73B, 226 (1978).

(37) - G. Nardelli and G. Preparata, Frascati Report LNF-77/56 (1977); see also J. P. Perez-Y-Jorba and F. M. Renard, Phys. Reports 31, 3 (1977).

(38) - I. S. Shapiro, Soviet Phys.-Uspekhi 16, 173 (1973); O. D. Dalkarov and I. S. Shapiro, Report ITEP-154 (1978).

(39) - F. Myhrer, Report CERN TH-2348 (1977).

(40) - C. Hong-Mo, Report CERN TH-2540 (1978); C. Hong-Mo and A. Høgaasen, Phys. Letters 72B, 400 (1978); Nuclear Phys. B136, 401 (1978); C. Hong-Mo, Report RL 78-094 T 230 (1978), Invited Paper to the XIX Intern. Conf. on High Energy Physics, Tokyo (1978).

(41) - G. C. Rossi and G. Veneziano, Report CERN TH-2287 (1977); Nuclear Phys. B123, 507 (1977).

(42) - J. C. Pati and A. Salam, Phys. Rev. D8, 1240 (1973); Phys. Rev. Letters 31, 661 (1973); Phys. Rev. D10, 275 (1974); Trieste ICTP Report IC/77/65 (1977).

(43) - B. McCoy and T. T. Wu, Report CERN TH-2405 and TH-2487 (1978).

(44) - M. Bassetti et al., Frascati Report LNF-78/7 (1978) and LNF-78/15 (1978).

(45) - CERN Yellow Report 77-13 (1977), p. 377.

(46) - E. H. Chao and C. Gareyte, Internal Report SPEAR, 197/PEP 224.

(47) - S. Tazzari, Adone Int. Memo T-93 (1978); S. Guiducci and G. Martinelli, Adone Int. Memo T-89 (1978).

(48) - F. Sauli, Principle of Operation of Multiwire Proprtional and Drift Chambers, CERN Yellow Report 77-09 (1977).

(49) - C. W. Fabjan et al., A Drift Chamber Vertex Detector for ISR, Contribution Paper for Wire Chamber Conference, Vienna (1978); Specification of the Linera Hybrid Circuits for R 807 Drift Chamber, CERN Int. Report EP/JL (1978).

(50) - V Radeka nad P. Rehak, Report BNL 23345 (1977); V. Radeka, IEEE Trans. NS-21, 51 (1974); J. L. Alberi and V. Radeka, IEEE Trans. NS-23, 251 (1976).

(51) - W Braunschweig et al., Nuclear Instr. and Meth. 134, 261 (1976).

(52) - T. E. Kalogeropulos, Phys. Rev. Letters 33, 1631 (1974); Proceedings of the VI Intern. Conf. on Nuclear Structure, Santa Fé (1975), p. 155.

(53) - G. Battistoni et al., Nuclear Instr. and Meth. 152, 423 (1978); V. Bidoli et al., Frascati Report LNF-76/58 (1976).

(54) - G. Battistoni et al., Frascati Report LNF-78/60 (1978), to be published in Nuclear Instr. and Meth.

(55) - C. Cerri and F. Sergiampietri, private communication.

(56) - H. Terazawa, Rev. Mod. Phys. 45, 615 (1973)

(57) - C. Bacci et al., Lett. Nuovo Cimento 3, 709 (1971). G. Salvini, Suppl. Journ. Phys. 35C, 1 (1974); G. Barbiellini et al. Phys. Rev. Letters 32, 385 (1974).

(58) - S. D. Drell, Proceedings of the Intern. Conf. on Elementary Particles, Amstedam (1972), p. 307.